Diffusion as an Oil Recovery Mechanism During CO_2 Injection in Fractured Reservoirs

Master Thesis in Reservoir Physics

Stig Holme Lie

Department of Physics and Technology

University of Bergen

November 2013

Abstract

This thesis is part of an ongoing study of enhanced oil recovery by CO_2 injection in the Reservoir Physics research group at the Department of Physics and Technology (IFT) at the University of Bergen. This work investigates the feasibility of oil recovery from diffusion during miscible CO_2 injection in fractured core plugs by conducting appropriate laboratory tests and numerical simulations.

A total of 10 miscible CO_2 injection tests were conducted in the laboratory using artificially fractured core plugs and were performed in four laboratories: ConocoPhillips Research center in Bartlesville, Oklahoma; Texas A&M in College Station, Texas; Haukeland University Hospital and at IFT. A feasibility study for oil recovery by CO_2 injection in unconventional oil shale reservoir was performed. The results show that recovery of oil took place by molecular diffusion from tight shale cores with permeability on the order of nanodarcies. More experiments are needed to draw definite conclusions on this matter.

A novel approach was tested using explicit imaging of CO_2 with ^{11}C as nuclear tracer in the CO_2 phase. Dynamic displacement was visualized using a PET/CT scanner. Early breakthrough of CO_2 was caused by a high injection rate and fingers developed through the high conductive fracture; preventing CO_2 from saturating the whole fracture whereas only a small area was saturated with CO_2. Still, diffusion of CO_2 into the matrix from this area of the fracture was successfully visualized during a small time period limited by the short lifespan of the tracer.

As a part of this thesis, a high pressure CO_2 experimental setup was designed and built at IFT. To achieve a diffusion dominated recovery the cores were cut along the cylinder axis and equipped with a high conductive spacer to maintain an open fracture to limit viscous forces in the displacement of oil and thereby isolating the recovery mechanism to molecular diffusion alone.

Oil recovery during injection of supercritical CO_2 injection (P = 107 bar, T = 42 °C) in a fractured, 100% oil saturated core plug was visualized in a CT-scanner. CO_2 concentration profiles were calculated from the development in spatial distributed CO_2 saturation during the experiment. The CT images confirmed that molecular diffusion from the fracture to the oil saturated matrix was the dominating recovery mechanism. This was also confirmed by the absence of a differential pressure across the core during CO_2 injection. Total recovery reached 96% OOIP after approximately 7 pore volumes of CO_2 injected. An effective diffusion coefficient was calculated to be $D_e = 1.66*10^{-9} \pm 7.2*10^{-10}$ m^2/s from concentration profiles based on a graphical method of solving Fick's second law of diffusion. Results from several mass balance injection tests confirmed the large potential with the use of miscible CO_2 injection for EOR, with recoveries ranging from 95-98% OOIP, if large enough quantities of CO_2 were injected. The final recovery

was not affected by the presence of irreducible water saturation but the flood was less efficient as a larger amount of injected CO_2 was required to obtain the same end-point saturation.

Numerical simulations have been performed with CMG GEM simulator and matched with the CO_2 visualization experiment with oil recovery by diffusion. The simulations satisfactorily reproduced the experimental data and an effective molecular diffusion coefficient of $D_e = 3.02*10^{-9}$ m^2/s was estimated. A sensitivity parameter study was conducted with known parameters that influence oil production by diffusion and was focused on changes in porosity, permeability and the diffusion coefficient. The model was not sensitive to variation in permeability ranging from 1 nD to 1D. The CO_2 diffusion process was, however, strongly influenced by changes in porosity and the diffusion coefficient. The model also confirmed that oil was only recovered at miscible conditions between the injected CO_2 and oil. The validated model should be further developed to study parameters that impact diffusion and can be used to predict oil production in more complex scenarios and possibly on field scale.

Acknowledgements

First and foremost, I would like to express my sincere gratitude to my advisors, Professor Arne Graue and Associate Professor Martin Fernø at the Department of Physics and Technology at University of Bergen for their guidance and support with this thesis and the opportunity given to conduct experiments abroad.

Thanks to Associate Professor David Schechter at the University of Texas A&M for being able to participate in experiments involving reservoir oil shale and providing us with necessary supplies. Also thanks to PhD Candidate Francisco Tovar for his help with experiments.

I would like to thank Sr. Reservoir Engineer Denis Pone for his guidance and professional expertise and Tech. chemist Jasin Palmer for his contribution with laboratory work and willingness to help with the CT experiments at ConocoPhillips Research Center in Bartlesville, Oklahoma.

I would like to thank the staff at Haukeland University Hospital for helping us run experiments and being able to conduct experiments in their PET/CT lab. A special thanks to MSc Stuart Baird for interesting discussions and cooperation with experiments and to PhD Candidate Øyvind Eide for his guidance with the use of imaging software and numerical simulations. Also thanks to PhD Candidate Jarand Gauteplass, PhD Candidate Lars Petter Hauge and MSc Thomas Mathiassen for cooperation with experiments conducted. Thanks to all my fellow students for making my study an invaluable experience to me.

Finally I want to express the deepest appreciation to my parents and my brother for their motivation and support throughout my years of study.

Bergen, November 2013

Stig Holme Lie

Table of contents

Introduction

The rate of new discoveries compared to produced reserves has been declining in the last decades (Alvarado, 2010). Many of the existing oil fields discovered to date are approaching the end of water flooding and are near the tail end production whereas large quantities of oil are left behind after conventional recovery methods. Enhanced oil recovery (EOR) processes are therefore needed to maximize oil recovery, extend the field life and increase profitability of the fields. EOR describes methods to extract the residual oil that is left behind after conventional recovery methods by increasing the macroscopic and microscopic sweep efficiency. Common recovery methods that refers to EOR include gas injection, in-situ combustion, WAG, polymers, surfactants and foam (Zolotukhin, 2000). The potential of incremental oil recovery by EOR processes world-wide is extensive.

Increased focus on the anthropogenic climate change and greenhouse gas emissions has led to an extensive research on carbon capture and sequestration (CCS), and carbon capture, utilization and sequestration (CCUS). The former deals exclusively with CO_2 gas storage and the latter differs by using the injected CO_2 for EOR before eventually being stored (Falcone and Harrison, 2013). Statoil has since 2006 injected over 13 Mt CO_2 into the Utsira saline aquifer in the North Sea as a part of the Sleipner CCS project for economic benefits (Falcone and Harrison, 2013). Increasing interest for EOR, coupled with CO_2 emission and governmental taxation, make CCUS combined with CO_2 EOR of general interest. An undergoing project that highlights the success of CCUS is being conducted in the Weyburn field in Canada (Malik et al., 2000). Another CCUS project was recently implemented in a field in Abu Dhabi after a screening study that showed to be economically viable (Morsi et al., 2004).

CO_2 injection into oil fields for the purpose of EOR has been commercially applied for over 40 years (Lambert et al., 1996). Most of the CO_2 EOR projects are found in the US because of favorable reservoir conditions, availability of low-cost CO_2 (from large natural sources and natural gas plants) and an extensive CO_2 pipeline infrastructure (NETL, 2010). CO_2 injection for EOR has not been conducted on the Norwegian Continental Shelf (NCS) resulting from technical challenges related to offshore projects combined with high costs of CO_2 (Lindeberg and Holt, 1994). Still, the interest of using CO_2 as injection fluid grows faster than any other methods, with an increase in total gas injection projects from 38% in 1984 to 65% in 2004 (Stosur, 1990).

Miscible CO_2 injection offers the greatest oil recovery potential, since it has the ability to recover all oil in the areas of the reservoir that is in contact with the gas (Lambert et al., 1996, Skjæveland, 1992). CO_2 increases oil recovery by primarily altering the physical properties of the oil phase, i.e. swelling of the oil, reduction of oil viscosity, increased oil density, vaporization and extraction of hydrocarbon components

up to C_{30}, reduction of the interfacial tension between the oil and CO_2 and the ability to achieve miscibility with crude oil at relatively low pressure (Ahmed, 1994, Holm, 1974, Lambert et al., 1996). Under miscible conditions, CO_2 has a density close to that of a liquid and is higher than that of other gases used for EOR, such as nitrogen (N_2) and methane (CH_4). That, together with the ability to increase water density and in the same time decrease oil density, makes CO_2 less prone to gravity segregation compared with N_2 and CH_4 (Brock and Bryan, 1989, Bui, 2013).

High oil recoveries (>95%) after miscible CO_2 floods has been reported on both experimental tests and in gas-swept areas in fields (Fernø et al., 2010, Holm, 1974). However, poor sweep efficiency has been a problem in CO_2 floods on field scale. Total oil recoveries reported in the literature from miscible CO_2 floods is typically 10-20% of OOIP (Enick, 2012). High mobility of CO_2 compared to oil and water leads, in many cases, to poor volumetric sweep efficiency limited by gravity tonguing and/or viscous fingering (Lescure and Claridge, 1986). The need for mobility control during CO_2 flooding has led to an extensive study of numerous methods to mitigate the problem.

Naturally fractured carbonate reservoirs are highly heterogeneous in terms of porosity and permeability (Chillenger, 1983, Fernø, 2012). High conductivity through the fracture system usually leads to rapidly declining production and low total recoveries (Alvarado, 2010, Allan, 2003). The largest fraction of hydrocarbons is stored in the matrix blocks (Jahediesfanjani, 2006). Water injection is inefficient in approximately 80 % of these fields because of mixed-wet and oil-wet preferences, but oil could be produced during miscible CO_2 injection by diffusion of CO_2 from the fracture network into the matrix blocks (Golabi, 2012, Roehl, 1985, Vuillaume et al., 2011).

Displacement efficiency in fractured reservoirs during both secondary and tertiary CO_2 floods is strongly influenced by achieving miscibility between the CO_2 and the oil. Molecular diffusion has shown to be a major recovery mechanism in fractured reservoirs on both laboratory core floods (short diffusion lengths) or during field scale floods (long diffusion lengths) (Grogan et al., 1988, Vuillaume et al., 2011). To determine the conditions where diffusion processes are important for oil recovery and to scale laboratory core floods to field scale, estimation of diffusion rate given by molecular diffusion coefficients are needed.

A wide range of parameters that affect the efficiency of CO_2 injection has been previously examined by the Reservoir Physics research group at the Dept. of Physics and Technology, UoB. The results from this thesis are built on that foundation and emphasize the potential of miscible CO_2 injection for EOR in naturally fractured reservoirs; showing that recovering oil from the matrix by diffusion of CO_2 from a fracture is an effective recovery mechanism. Visualization of the displacement has been conducted with the use of CT and CT/PET scanners along with several mass balance experiments to compare the results.

A numerical simulation model has been developed and validated against laboratory tests to study different parameters that control oil recovery by diffusion.

This thesis consists of 10 chapters. Chapter 1 introduces the most basic parameters in reservoir physics that are relevant for this thesis. Chapter 2 gives a general understanding of naturally fractured reservoirs including recovery mechanisms. Chapter 3 contains a literature study of CO_2 as the displacing fluid in petroleum reservoirs. Chapter 4 gives a short introduction to visualization methods by the use of CT and CT/PET. Chapter 5 explains the experimental procedures. The results from this thesis are presented and discussed in chapter 6. Conclusions that are drawn based on the results are listed in chapter 7 and future work in chapter 8. Chapter 9 presents the nomenclature and chapter 10 lists all the references used in this thesis. Appendix A and B presents the formulas used in uncertainty calculations and the simulation data file, respectively.

1 Fundamental Principles in Reservoir Physics

In this chapter the most basic parameters in reservoir physics that are relevant for this thesis are introduced. These different parameters control the saturation distribution, the fluid behavior and interactions and are important in the evaluation and the production of a reservoir (Zolotukhin, 2000).

1.1 Porosity

The porosity describes the amount of pore volume in the rock, i.e. the volume that is not filled by rock grains or mineral cement. This volume can contain fluids and thereby defines the storage capacity of fluids in the specific rock. Porosity is one of the most important parameters when considering a reservoir rock, and is defined as the ratio between the pore volume (V_p) and the total volume (V_t) (Selley, 1998):

$$\phi = \frac{V_p}{V_t} = 1 - \frac{V_m}{V_t} \tag{1.1}$$

where V_m the volume of the rock matrix. Porosity varies with grain size, shape of the grains and grain distribution (Lien, 2004). Accurate estimates of porosity are important in order to determine the volume of oil and gas present in the reservoir and can be measured from well samples in a laboratory or directly through well logging.

1.2 Permeability

The permeability of a rock defines the rocks capability to transmit fluids through a network of interconnected pores. Permeability is directly related to porosity, so the factors affecting porosity will also affect the permeability (Zolotukhin, 2000). A rock with no interconnected pores will be impermeable and will not be able to transmit fluids. Permeability, together with porosity, is the two most important factors when evaluating the potential of a petroleum reservoir.

1.2.1 Absolute permeability

The *absolute* permeability, *K*, is the permeability of the rock when there is only one single fluid present. It can be determined by Darcy's law for fluid flow in a porous media, given by

$$Q = -\frac{KA}{\mu}\frac{\Delta p}{L} \tag{1.2}$$

where Q [cm^3/s] is the fluid flow rate, μ [cP] is the fluid viscosity, A [cm^2] is the cross section area, L [cm] is the core sample length, Δp [bar] is the pressure drop across the core sample and K is the absolute permeability [D].

Darcy's law is an empiric law which is only valid under laminar and horizontal flow, 100% saturated with one incompressible fluid with no chemical or physical reaction between the fluid and the rock. The absolute permeability of a rock is constant for a particular rock and independent of the fluid present and can be determined in the laboratory by injecting a single fluid through a core sample.

By using equation (1.2), the absolute permeability can be determined by measuring the differential pressure across the core sample with known dimensions (length and width) at different flow rates as shown in **Figure 1.1** (Tiab, 2012).

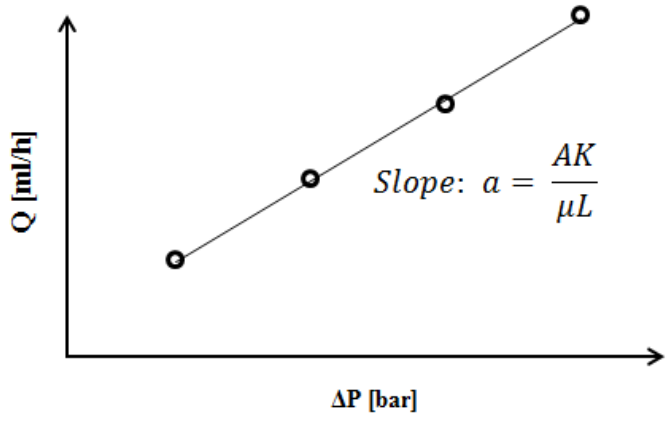

Figure 1.1: Empirical method of determining absolute permeability. Modified from (Zolotukhin, 2000).

1.3 Effective and relative permeability

When two or more immiscible fluids are present in a petroleum reservoir, the flow of each individual fluid will affect the flow of the other fluids present. Each specific fluid will then have an effective permeability, depending on the relative saturation of the fluids (Zolotukhin, 2000). The effective permeability is given by

$$K_{e,i} = \frac{q_i \cdot \mu_i}{A} \frac{L}{\Delta p} \quad , \quad i = o, w, g \tag{1.3}$$

The *relative* permeability is defined as the ratio between the effective permeability at a specific saturation to the *absolute* permeability of the rock (Lien, 2004):

$$k_{r,i} = \frac{K_{e,i}}{K} \tag{1.4}$$

where $k_{r,i}$ is the relative permeability of a fluid i, $K_{e,i}$ is the effective permeability of a fluid *i*. The relative permeability is often given as a function of water saturation, and depends on pore geometry, wettability, fluid saturation, saturation history (drainage or imbibition), reservoir temperature and pressure, overburden pressure and rock types with heterogeneities in terms of porosity and permeability (Xiao et al., 2012). The relative amount of each fluid present is controlled by the saturations, S_i, and the interactions between the different phases.

1.4 Fluid interaction

Fluids present in a petroleum reservoir are attracted to each other by cohesive forces, as well as being attracted to the rock surface by adhesive forces. These forces help explain important parameters regarding the interactions between the different liquids and surfaces in a reservoir.

1.4.1 Interfacial tension

There exists an interfacial tension (σ) between the molecules of two fluids in contact with each other. The extent of the interfacial tension represents the amount of energy that keeps the two fluids apart and if the temperature is constant this energy depends on the chemical composition of the fluids. Two fluids can have three different interfacial tensions depending on the amount of cohesive forces between their molecules (Zolotukhin, 2000):

- A positive interfacial tension ($\sigma > 0$) implicates that the fluids are immiscible, in which the molecules in both fluids are more attracted to its own kind.
- A neutral interfacial tension ($\sigma \approx 0$) implicates that the fluids are miscible, in which the molecules in the fluid are equally attracted to both fluids. The fluids will mix by diffusion until equilibrium is reached.
- A negative interfacial tension ($\sigma < 0$) implicates that the molecules in both fluids are strongly attracted to each other and will mix instantaneously, creating a new fluid. This process is called dissolution.

1.4.2 Mobility

Mobility is an important factor for the flow patterns of two or more fluids in a porous medium. It is well established that the mobility ratio between fluids present in the reservoir will have a large impact on flow patterns (J.S. Aronofsky, 1956). The mobility, λ, of a fluid i is given by

$$\lambda_i = \frac{k_{r,i}}{\mu_i},\ i = o, w, g \tag{1.5}$$

where μ is the viscosity of the fluid. In a displacement process where water displaces oil, the mobility ratio is then given by

$$M = \frac{\lambda_w}{\lambda_o} = \frac{\frac{k_{r,w}}{\mu_w}}{\frac{k_{r,o}}{\mu_o}} \tag{1.6}$$

Floods with low mobility ratio ($M < 1$) are considered efficient, resulting in a stable displacement front. A high mobility ratio ($M \geq 1$) will result in a unstable displacement front dominated by viscous fingering (Zolotukhin, 2000).

The impact of heterogeneities in the reservoir increases as the mobility ratio become more unfavorable (Mridul Kumar, 2008). To ensure a stable displacement and a higher total recovery, a low mobility of the displacing fluid is preferable.

1.5 Miscibility

Miscibility can be defined as the ability of two or more substances to form a single homogenous phase when mixed in all proportions without the existence of an interface (L.W. Holm, 1986, Rao, 2000). Miscible displacement implies that the interfacial tension between the displacing and the displaced fluid is zero (Glaso, 1990, Rao, 2000, Thomas, 1994).

In an oil recovery process, miscibility between the displaced and displacing phase (like oil and gas) increase the displacement efficiency and the total oil recovery (Olaoluwa O. Adepoju, 2013). Regions previously flooded with immiscible fluids (like water) may contain large amounts of entrapped residual oil. Miscible flooding is considered as a promising enhanced oil recovery method because of its ability to increase the microscopic displacement efficiency, theoretically displacing all the residual oil (Skjæveland, 1992).

Miscible processes have been successfully developed for enhanced oil recovery (EOR) in the past 50 years (L.W. Holm, 1986). The miscible solvents used in these processes may include natural gas, inert gas and CO_2 (Ahmed, 1994). There are three miscible displacement categories, depending on the composition of the fluids; (1) First contact miscibility (2) vaporizing gas drive and (3) condensing gas drive.

Ternary diagrams are used to describe the phase behavior of three-component system at constant system temperature and pressure and are useful in describing the three different categories. The apexes of the diagram represent 100% of light components (C_1), intermediate components (C_2-C_6) and heavy components (C_{7+}).

First contact miscibility

Figure 1.2 illustrates the concept of a first contact miscibility displacement process. Point C represents the composition of the crude oil. Point A represents the composition of the injected gas. Point P represents the critical or plait point. The area inside the envelope is the two-phase region and outside the envelope is the single phase region. In this case the crude oil and the injected gas are first contact miscible under the specific conditions, since the dilution path does not enter the two phase area (Lake, 1989).

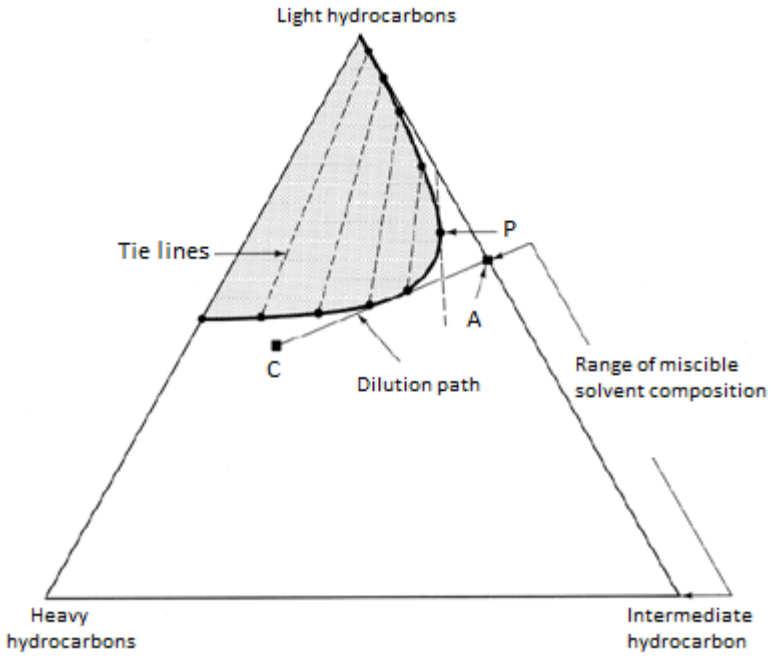

Figure 1.2: Ternary diagram showing an example of a first miscibility displacement process. Modified from (Lake, 1989).

Vaporizing gas drive

Figure 1.3 illustrates the concept of a vaporizing gas drive process. In this case a relatively lean containing mostly methane or other low molecular weight hydrocarbons or sometimes inert gas such as nitrogen is injected into the reservoir. It displaces reservoir oil consisting of intermediate components (C_2-C_6). The composition of the injected gas is modified as it moves through the reservoir. Vaporization of intermediate components takes place at the leading edge of the gas front where gas is in contact with the oil. Imagine several mixing cells set up diagonally in a one dimensional displacement. In the first cell the light gas gets saturated by the heavier oil components and the resulting composition of the mixture is M_1. The mixture consists of two phases, a gas with composition G_1 and a liquid with composition L_1.

The gas in this cell is more mobile than the oil. This light gas, partly enriched with intermediate components, will be transported to the next cell. In the second cell the gas is getting even more saturated with intermediate components which represent the composition M_2. The mixture is still two phases represented by G_2 and L_2. The process continues with vapor-phase composition change along the saturated vapor curve, G_3 and L_3, G_4 and L_4 etc. The gas is gradually saturated with intermediate components until the dilution path reaches the edge of the two-phase area (plait point) and the critical tie line. Beyond this point, the leading gas front will become fully miscible with the oil. Behind the leading cell, which develops miscibility, there will be a mixture zone gradually saturated with intermediate components. The size of the mixing zone depends on several factors, including dispersion and velocity gradient. Miscibility will develop if the composition of the solvent and the reservoir oil are on opposite sides of the critical tie line (Lake, 1989).

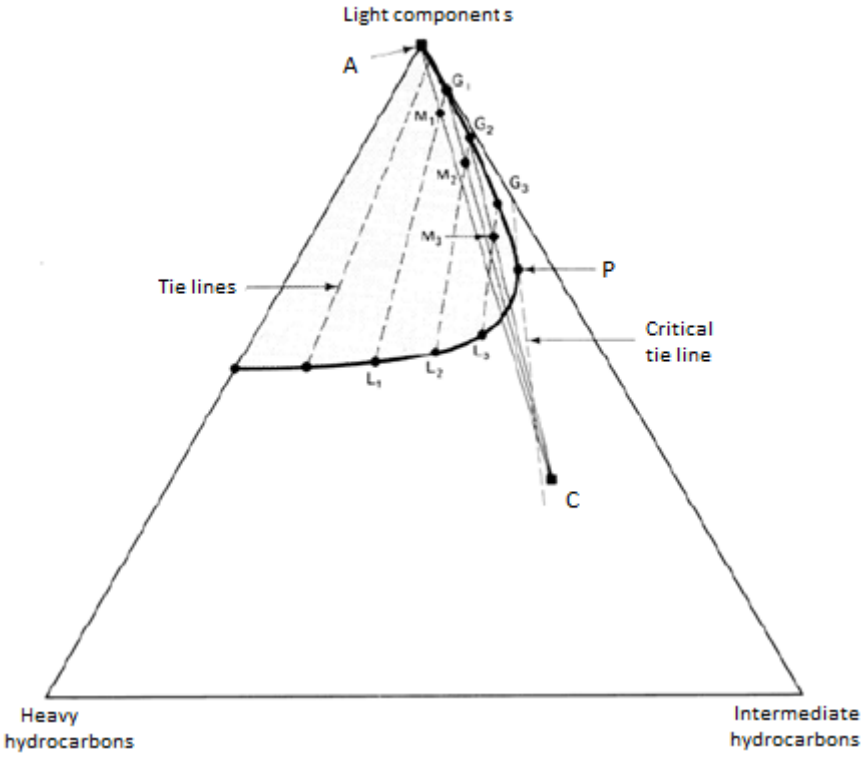

Figure 1.3: Ternary diagram showing an example of a vaporizing gas drive displacement. Modified from (Lake, 1989).

Condensing gas drive

Figure 1.4 illustrates the concept of a condensing gas drive process. In this case the injected gas (given by A) which generally contains larger amounts of intermediate hydrocarbons is displacing the reservoir oil (given by C) containing heavier components. Imagine a one dimensional displacement same as in the vaporizing gas drive case. Condensation of light components from the rich-gas into the oil in the first cell will result in a two-phase mixture M_1, with gas composition G_1 and liquid composition L_1. The more mobile gas, which is now diminished by light components, will move to the next cell. In the first cell more light components will condense to the oil as fresh gas enters the cell, leading to a mixture M_2. This means that the process will develop miscibility at the rear of the mixing zone. The leading gas in the front of the displacement will be immiscible with the reservoir oil. Because both the solvent and the reservoir oil are on the same side of the critical tie line, it will lead to an immiscible displacement process (Lake, 1989). For multiple contact miscibility by condensation to occur the injected fluid must be on the opposite side of the critical tie line. If it is not, condensation of CO_2 into the reservoir oil will still occur, however, miscibility will not be developed.

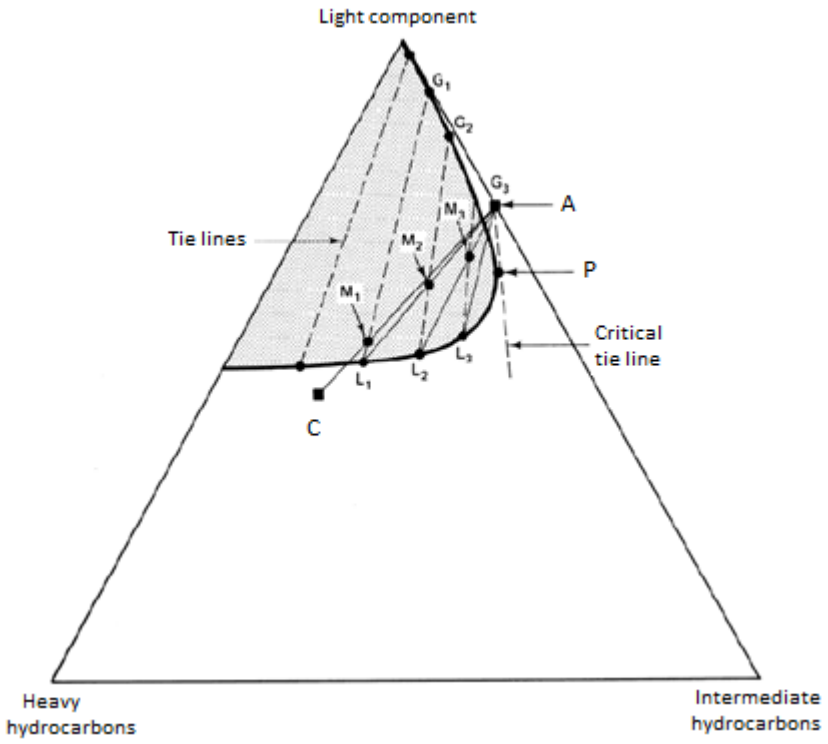

Figure 1.4: Ternary diagram showing an example of a condensing gas drive process. Modified from (Lake, 1989).

1.5.1 Minimum miscibility pressure

Two fluids that are immiscible at a certain pressure may become miscible at higher pressures. The minimum miscibility pressure is the minimum pressure required to achieve multi-contact miscibility between the injected gas and the reservoir oil at a given temperature and composition (Skarestad, 2011, Amao et al., 2012, Zolotukhin, 2000). Accurate predictions of MMP are especially important in reservoir evaluation to determine the necessary conditions for miscible displacement processes. Miscible enhanced oil recovery processes have estimated additional 10-15% recovery of OOIP (Original oil in place), compared to immiscible displacement processes that with 5-10% additional recovery (Lake, 1989). CO_2 has major advantages compared to other miscible agents because it achieves miscibility with reservoir oil at lower pressures compared with natural or inert gases (Ahmed, 2013). Several techniques have been performed to determine the MMP (Christiansen, 1987, Elsharkawy, 1992, Ayirala, 2006):

- Slim-tube experiment
- Rising bubble measurement
- Vanishing interfacial tension

The slim-tube displacement is the most widely used method for determining the MMP. This method involves displacement of oil with a miscible agent at a given reservoir temperature through a small diameter tube packed with sand or glass beads. The pressure is regulated and MMP is determined based on the oil recovery and visual observations (Christiansen, 1987).

Slim-tube experiments are fast, reproducible and easy to conduct. A disadvantage by using this method is that reservoir rock properties are not being taken into account. These effects may be heterogeneities, relative permeability, wettability and pore geometry (Ahmed, 1994). Contamination of CO_2 influences the MMP in slim-tube experiments, and observations that free O_2 increases the CO_2 MMP significantly have been reported (Haifeng Jiang, 2012).

The rising bubble measurement (RBM) involves observation of rising gas bubbles in oil through a sight gauge at a constant pressure. By gradually increasing pressure the gas will eventually be miscible with the oil and the MMP is found (Christiansen, 1987).

The vanishing interfacial tension method involves measuring the interfacial tension of two fluids with constant temperature at increasing pressure. By plotting IFT as a function of pressure, the MMP can then be found by extrapolation of the IFT to zero (Ayirala, 2006).

Figure 1.5 shows the determination of MMP of CO_2 and oil, for a displacement process of oil with 1.2 hydrocarbon pore volume of CO_2 by the use of a slim-tube experiment. The MMP is characterized by the recovery factor graph reaching a plateau. Increasing pressure above the MMP will not tend to increase the recovery since first contact miscibility is developed (Holm, 1974, Skarestad, 2011).

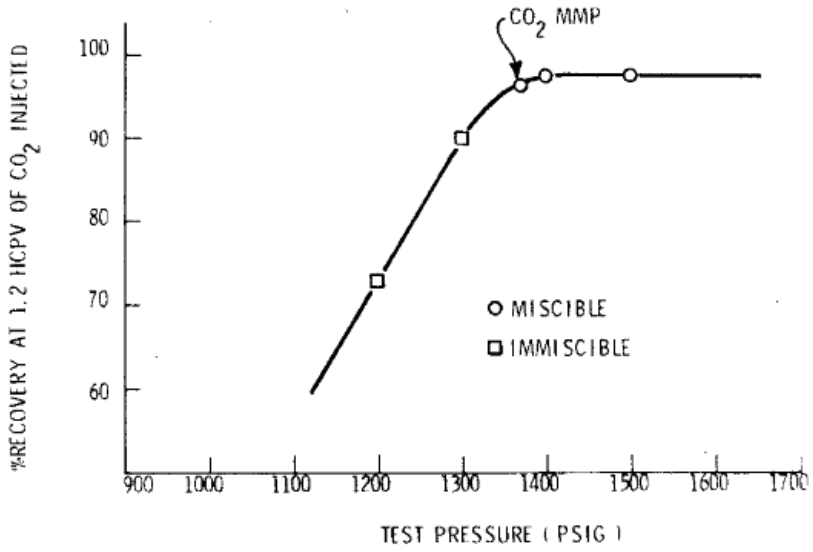

Figure 1.5: Test results showing MMP in a displacement of reservoir oil with 1.2 hydrocarbon pore volume of CO_2 injected (Yellig, 1980).

1.6 Enhanced oil recovery

Tertiary recovery, referred to as enhanced oil recovery, is recovery of additional oil by other methods after the conventional primary and secondary methods (Henry, 1977, Katz, 1980). EOR includes injection of fluids that are not initially present in the reservoir in order to recover oil that is left behind after secondary recovery (Howes, 1988, Lake, 1989).

Oil recovery from primary and secondary recovery are often lower than 50% of OOIP (Farouq and Thomas, 1989). Naturally fractured carbonate reservoirs have recoveries lower than 30% of OOIP because of wettability preferences, which makes good candidates for EOR processes (Austad, 2008).
EOR methods are generally categorized into three major types; gas injection, thermal recovery and chemical injection (Stosur and Luhning, 1994). The purpose of EOR is to increase the macroscopic and microscopic sweep efficiency (Zolotukhin, 2000).

Microscopic sweep can be increased by lowering the interfacial tension between the displacing fluid and the oil. The major methods of reducing the interfacial tension are miscible gas injection, adding a stimulating microbial growth (MEOR) or by adding surfactants to the displacing fluid (Zolotukhin, 2000).
Macroscopic sweep can be increased by altering the mobility ratio between the displacing and the displaced fluid (Farouq and Thomas, 1989, Zolotukhin, 2000). The most common methods of mobility control is by foam injection, WAG (Water Alternating Gas), SWAG (Surfactant Water Alternating Gas), FAWAG (Foam assisted Water Alternating Gas) and polymer injection (Zolotukhin, 2000). EOR methods applied on the NCS are miscible hydrocarbon gas injection, WAG, SWAG, FAWAG and MEOR. All projects were to some extent successful, especially WAG injection, except WAG in the Ekofisk field and FAWAG in Snorre (Awan et al., 2006).

Gas injection for EOR can be implemented as secondary and tertiary recovery and involves injection natural gas (CH_4), nitrogen (N_2) or carbon dioxide (CO_2) into the reservoir. The gases either expands and push oil through the reservoir towards production wells, or dissolve in the oil, decreasing its viscosity and facilitating oil flow to the production wells . It may recover oil that has already been in contact with water (tertiary recovery), including oil that has not been in contact with water (secondary recovery) since the gas may choose other flow paths than water (Skarestad, 2011).

2 Recovery mechanisms in fractured reservoirs

This thesis is focused on the study of miscible gas injection for EOR in fractured carbonate reservoirs. This chapter gives a general overview of possible scenarios in fractured petroleum reservoirs, with focus on oil displacement by molecular diffusion.

2.1 Naturally fractured carbonate reservoirs

Carbonate reservoirs are estimated to hold more than 60% of the world's oil (Akbar, 2000), and almost half of the world's gas injection projects worldwide are in carbonate reservoirs (Alvarado, 2010). Most carbonate reservoirs are naturally fractured and are highly heterogeneous in terms of porosity and permeability (Chillenger, 1983, Fernø et al., 2010). Examples of naturally fractured reservoirs are the Asmari limestone reservoir in Iran, the vugular carbonate reservoirs in Mexico and a group of chalk reservoirs on the NCS (Firoozabadi, 2000).

A fractured reservoir is defined as a reservoir where the fractures have a significant impact on performance and oil recovery (Fernø, 2012). **Figure 2.1** displays an example of natural fractures in a carbonate rock from a field excursion in the Middle East by Statoil (Ras Al Khaimah).

Figure 2.1: Field example of a naturally fractured carbonate rock in the Middle East. From (Statoil, 2013).

The natural fracturing, leading to a higher permeability throughout the reservoir is essential when determining if a fractured reservoir is profitable or not. The fractures may lead to an early breakthrough of injected fluids through the fracture network and bypass rock matrix. The fractures provide oil flow paths and the matrix provides the storage (Firoozabadi, 2000). This usually leads to rapid production declines and low total recoveries from fractured reservoirs (Alvarado, 2010, Allan, 2003). Fluid flow in this type of reservoir is governed by the distribution, orientation and the interconnectivity of the fracture system (Fernø et al., 2010). Another important factor that may influence fluid flow is the degree of mineral cement within the fractures, which is a function of fracture size and the diagenetic history of the rock (Stowell, 2001).

A common characterization is matrix blocks with low porosity and permeability surrounded by a network of fractures with high permeability and low porosity. The largest fraction of hydrocarbons is isolated in the matrix blocks acting as hydrocarbon storage (Jahediesfanjani, 2006). The high permeability fractures surrounding matrix blocks represent primary pathways for hydrocarbon migration to the production wells, strongly affecting the production drive mechanism including the total sweep efficiency.

One classification of fractured reservoirs is introduced (Allan, 2003):

- Type I: Fractures provide essential hydrocarbon storage capacity and permeability in a reservoir. The matrix has little porosity and permeability.
- Type II: Fractures provide fluid-flow pathways and the rock matrix provides the essential hydrocarbon storage capacity in the reservoir. The rock matrix has low permeability and porosity.
- Type III: Fractures provide high permeable fluid flow pathways in an already economical producing reservoir. The matrix has low permeability but provides essential hydrocarbon storage capacity with high porosity.
- Type IV: Fractures do not provide significant additional storage or permeability in an already producible reservoir; fractures hinder fluid flow creating anisotropy (flow barriers).

The different types of fractured reservoirs mentioned above highlight the relationship between heterogeneities and the geological features related to hydrocarbon storage (Fernø, 2012). Classification of a potential fractured reservoir may reveal potential production and reservoir evaluation problems that can be anticipated. At reservoir scale these heterogeneities will have a large impact on the overall productivity and drainage of the field.

Natural fractures are usually induced geomechanically over time by diagenesis or deformation, whereas mechanical or induced fractures are caused by human activities such as drilling or hydraulic fracturing. The success of developing a fractured oil reservoir relies on the understanding of the fractures (mechanical or diagenetic, or both), the structure of their network (e.g. connectivity, fracture length, distribution) and accurate models of these networks (Sahimi, 2011). Knowledge of fracture networks is important for reservoir characterization and the assessment of fluid flow behavior. There are several methods to characterize the fracture distribution including wire line logs, conventional cores, sub-seismic investigation and seismic data (Shen, 2004).

The intensity of natural fractures is controlled by rock structure, lithology, bed thickness, underlying salt structures and other geological factors. In addition, fracturing is influenced by rock properties such as shale content, matrix porosity, carbonate contents and earlier tectonic events that has caused stress to the reservoir rock (Shen, 2004). Examples of fracture types found in carbonate reservoirs (such as Ekofisk) are stylolite, tectonic, irregular and healed fractures. Stylolite and tectonic fractures often provide enhanced permeability and are therefore of primary interest (Thomas et al., 1987).

2.1.1 Recovery methods in fractured carbonate reservoirs

There are fundamental differences between recovery from fractured and recovery from unfractured reservoirs, mainly caused by different roles of capillarity. The difference in capillary pressure of the matrix and fracture has a significant effect on recovery performance in fractured reservoirs (Firoozabadi, 2000). There are four basic recovery mechanisms in naturally fractured reservoirs, depending on the displacing fluid and reservoir characterization and conditions. These mechanisms include gravity drainage, spontaneous imbibition, viscous effects and molecular diffusion (Haugen, 2006).

High connectivity through the fractures in the reservoir leads to a lack of differential pressure buildup across the reservoir during production. In cases of water-wet carbonate reservoir rock, with water as the displacing fluid, the main recovery mechanism will be spontaneous water imbibition (Fernø, 2012). About 80 % of all carbonate reservoirs are neutral-wet to preferentially oil-wet, which are unfavorable conditions for spontaneous water imbibition (Golabi, 2012). In such cases gas is often used as the displacing fluid. If the gas is immiscible with the reservoir oil, the displacement of oil will be governed by gravity drainage. The recovery will be most efficient if the reservoir pressure and temperature is high enough to promote miscible conditions between the injected gas and the reservoir oil.

Miscible gas displacement in naturally fractured reservoirs

There are various cross flow of oil and gas between the less permeable matrix blocks and the high permeable fractures because of capillarity, gravity and viscous forces or due to diffusion (Firoozabadi, 2000). Both experimental data and theoretical analysis have proven that during a miscible gas process, the injected gas does not flow directly through the high permeable fractures (Firoozabadi, 1994). There are also strong matrix-fracture cross flow caused by gravity and dispersion of fluids during the flood (Tan and Firoozabadi, 1995, Dindoruk and Firoozabadi, 1997).

Gravity drainage will dominate the recovery in a miscible gas flood if the reservoir consists of large size, high permeable matrix blocks surrounded by gas in the fracture. The oil will be drained from the matrix to the fracture network because of density differences between the oil and the gas. In a scenario where the reservoir consists of small size matrix blocks with high capillary pressure and low permeability, which is the case in several North Sea fractured carbonate reservoirs, dispersion by molecular diffusion will be the dominate the recovery as gravity drainage will be inefficient (Darvish, 2006, Karimaie et al., 2007).

Gas in the fracture system is not in equilibrium with the oil in the matrix and, because of concentrations differences under miscible conditions, molecular diffusion will tend to equilibrate the matrix and fracture fluid compositions (da Silva, 1989). This leads to mass transfer of oil from the matrix to the fracture network (Karimaie et al., 2007).

2.2 Dispersion in porous media

Dispersion describes the mixing of fluids in porous media during a miscible displacement as a result of molecular diffusion and convective mixing within pores (Bear 1972; Lake 1989). Convective mixing describes the mechanic mechanisms of fluid mixing in a porous media resulting from heterogeneities that causes fluctuations of the local fluid velocity in the pores (da Silva, 1989, Rage, 1996, Ramirez, 1980). Molecular diffusion occurs at the contact zone between the fluids. Two miscible fluids in contact with each other will slowly diffuse into one another (Perkins, 1963, Sahimi, 2011).

Convective dispersion can be described by two mechanisms; Longitudinal dispersion describes spreading of a solute concentration front in the mean-flow direction as is passes through a porous media and transverse dispersion describes cross-spreading at a given transverse plane in a porous media (Sahimi, 2011). The two mechanisms drive convective dispersion in a homogenous, macroscopic porous media with a microscopic disordered pore space. It is important to mention that these two mechanisms of dispersion do not depend on molecular diffusion. The effect of molecular diffusion is usually more important at pore level (Sahimi, 2011).

Griffiths (1911) was the first to report some experimental data that demonstrated the dispersion process in a tube with the effect of molecular diffusion being present. Since then dispersion in porous media has been studied extensively, particularly in bead packs, unconsolidated sand packs and sandstones (Sahimi, 2011).

A classification of dispersion regimes has been made to explain the relationship between convective and diffusive drive mechanisms. The Péclet number is used to describe the different regimes, defined as the ratio between convective and diffusive transport (Sahimi, 2011):

$$P_e = \frac{d_g v}{D_m} \tag{2.1}$$

where d_g is the average diameter of a grain or bed [m], v is the average fluid velocity [m/s] and D_m is the molecular diffusion coefficient [m^2/s]. **Figure 2.2** shows the ratio between longitudinal dispersion coefficient, D_L , and the molecular diffusion coefficient, D_m, as a function of Péclet number. Five dispersion regimes are indicated. The longitudinal dispersion coefficient is proportional to the average fluid velocity (Perkins, 1963).

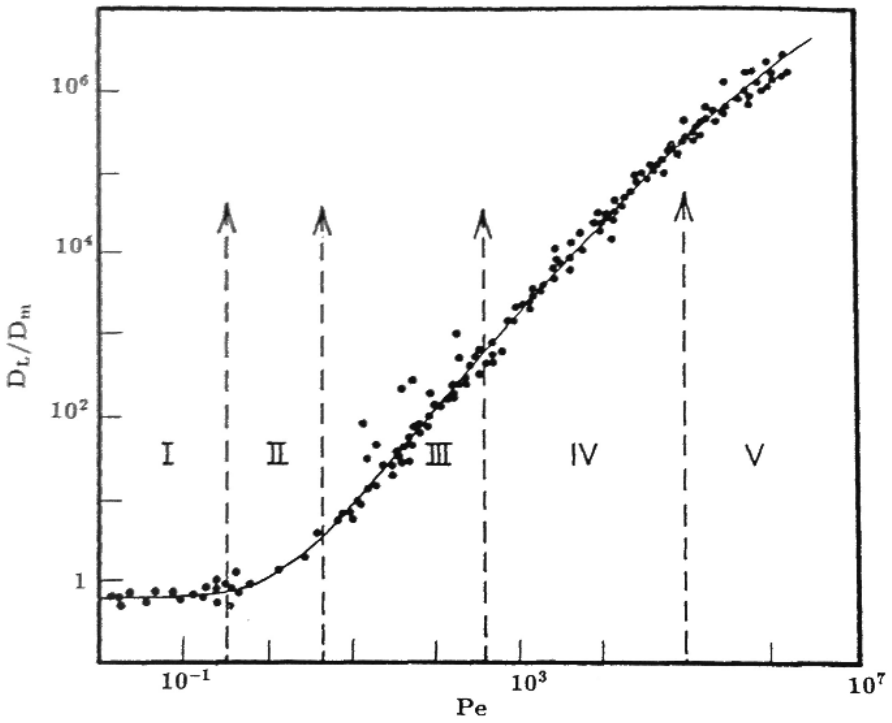

Figure 2.2: The five dispersion regimes and the dependence of the longitudinal coefficient, D_L, on the Péclet number. From (Fried, 1971).

The five dispersion regimes, indicated in **Figure 2.2**, can be described as follows (Sahimi, 2011):

I. $P_e < 0.3$ defines the *diffusive* regime. The bulk flow velocity is too slow for convection and the mixing is almost completely controlled by diffusion.

II. $0.3 < P_e < 5$ defines the *transition* regime. Convection contributes to dispersion, but diffusion is still strong.

III. $5 < P_e < 300$ defines the *power-law* regime. Convection dominates the dispersion, but the effect of diffusion cannot be neglected.

IV. $300 < P_e < 10^5$ defines the *purely convective* regime. The high fluid velocity leads to dispersion by convection alone, which is called mechanical dispersion.

V. $P_e > 10^5$ defines the *turbulent* regime. This regime is not of interest for fluid flow in porous media because the Péclet number is no longer the only correlating parameter. In this case Reynolds number should also be considered.

A sixth dispersion regime called the *holdup* regime have been introduced by Koch and Brady (Koch, 1985). This regime emphasizes a case where the solute is trapped in dead-end pores or dendritic structures, only affected by molecular diffusion (Sahimi, 2011).

During a miscible gas flood in a fractured reservoir the drive mechanisms will be convection in the fracture network and diffusion in the matrix where fluid velocities are small. Mass transfer of oil from the matrix to the fracture network will be controlled by molecular diffusion over time (Darvish, 2007, Islas-Juarez, 2004b). Factors that contribute to a larger area of contact between the fluids enhance the effects of molecular diffusion (Garmeh et al., 2009).

2.2.1 Diffusion

Molecular diffusion describes the mixing of miscible fluids by molecular transfer because of concentration gradients (Ghorayeb, 2001, Haugen, 2006). It is caused by movement of molecules from high-concentration areas to low-concentration areas by random motion until equilibrium is reached. The diffusional flux is described by Fick's first law:

$$J = -D\frac{\partial C}{\partial x} \tag{2.2}$$

where J is the diffusional flux, D is the molecular diffusion coefficient, C is the concentration and x is the position. Fick's second law introduce change in time, t, for an unsteady state diffusion:

$$\frac{\partial C}{\partial t} = D\frac{\partial^2 C}{\partial x^2} \tag{2.3}$$

The diffusion coefficient describes the molecular diffusivity of the solute in the solvent. According to Fick's second law, with a constant concentration at the boundary, the rate of diffusion is proportional to the square root of time. The rate of diffusion decreases significantly as a solvent diffuses further into a solute, which makes concentration related to square root of time (Cussler, 1997).

Phase behavior effects by molecular diffusion in a miscible CO_2 displacement in porous media depends on contact time, length of diffusion and rate of diffusion. The rate of diffusion is presented by the diffusion coefficient. The diffusion length provides a measure of how far the concentration has propagated in x-direction by diffusion in time *t* (Bird, 1976) and are affected by pore-space geometry, microscopic and macroscopic heterogeneities, fluid properties and rock wettability (Grogan et al., 1988).

Experimental studies have shown that the diffusion coefficient depends on pressure and temperature of the system, phase composition and fluid saturations. In a porous media the diffusion coefficient also depends on (Darvish, 2007):

- Pore connectivity, characterized by the tortuosity factor (τ)
- Porosity
- Matrix geometry in terms of fractured reservoirs

The diffusion coefficient is lower in porous media compared to bulk volume because of variable area of contact between two fluids but the mechanism diffusion remains the same (Darvish, 2007, Luo, 2008). The diffusive molecules have to travel a longer path through a tortuous pore network; hence the diffusion rate will be slower. For this reason a distinction between the absolute diffusion coefficient (absence of porous media) and effective diffusion coefficient (presence of porous media) has been made.

For a porous media the ratio between the absolute diffusion coefficient , D_a, and the effective diffusion coefficient , D_e, is given by (Perkins, 1963)

$$\frac{D_a}{D_e} = \frac{1}{F\phi} \qquad (2.4)$$

where *F* is the formation electrical resistivity factor and is the porosity. The ratio D_a/D_e is approximately 0.6 to 0.7 for unconsolidated sand packs (Perkins, 1963).

Diffusion coefficients can be estimated from measured data either directly by measuring the composition with time, or indirectly by measuring one of the system parameters that are changed as a result of diffusion (Sheikha et al., 2006). According to the literature the direct estimation of composition with time seems to be the most efficient method. The importance of estimating the diffusion coefficient from a slope of measured data with time rather than from individual data points were first presented in 1933 (Pomeroy, 1933).

Over the last decades experimental work has highlighted the importance of reservoir conditions when studying diffusion. Diffusion coefficients have been reported to be 5 to 10 times higher at reservoir conditions than those measured at ambient conditions and thereby cannot be comparable (Denoyelle, 1983).

Diffusion coefficients between CO_2 and different hydrocarbon systems at elevated pressure and temperature has been determined experimentally by Denoyelle and Bardon (Denoyelle, 1983), de Boer *et al.* (de Boer, 1984), Renner (1988), Grogan *et al.* (1988) and Aguilera *et al.* (2001). Convective effects may explain the large difference of experimental values of diffusion coefficients found in the literature (Grogan et al., 1988).

CO_2/n-decane diffusion coefficient

Renner (Renner, 1988) estimated effective diffusion coefficients between CO_2 and n-decane in Berea sandstone from volume/time profiles with different pressures at approximately 37.9 C°, using a solution of equation (2.3). Both horizontal and vertical core alignment were conducted, assuming a pure CO_2 source and semi-infinite porous medium as long as the CO_2 diffusion length did not reach the edge of the rock. The effective diffusion coefficients were higher for vertical core alignment than for horizontal alignment. In addition, an increase in pressure seemed to increase the diffusion coefficient (Renner, 1988).

Grogan *et al.* (Grogan et al., 1988) estimated CO_2/n-decane diffusion coefficient based on direct observation of the motion of an interface caused by diffusion of CO_2 through the oil without the presence of a porous media. Grogan used a horizontally aligned glass capillary tube (0.61 mm in diameters) to observe the diffusion process in a range of pressures, all at 25 °C. Estimated diffusion coefficients from Grogan's horizontal capillary tube was in the same range as Renner's horizontal alignment despite being conducted at different experimental conditions (e.g. without the presence of a porous media, different pressure and temperature). The results from Grogan also indicated that the diffusion coefficients increase with increasing pressure. Results from Renner and Grogan are shown in **Figure 6.17** in chapter 6.3.4, along with results from this work.

3 CO_2 as displacing fluid for EOR

Carbon dioxide (CO_2) is a transparent gas at ambient conditions composed of carbon (C) and oxygen (O). CO_2 has a central role in the photosynthesis process, and are stored naturally in our atmosphere, forest and oceans. This natural storage of CO_2 also includes coal, gas and oil, which is used as a source to the increasing energy demand worldwide (Lenntech, 2009).

CO_2 is in recent years highly debated because it is a greenhouse gas [GHG]. The large amount of CO_2 emission by human activity into the atmosphere enhances the greenhouse effect affecting the climate drastically. Most importantly, increased CO_2 emission leads to air pollution and global warming (Ran et al., 2012).

For this reason large quantities of CO_2 are injected into deep reservoirs known as CCS (Carbon Capture and Storage) projects (Iglauer, 2011b). Subsurface oil and gas reservoirs has the required properties to trap CO_2 and are excellent candidates for geological sequestration (Ran et al., 2012). These reservoirs have stored oil and gas since it first migrated millions of years ago and are thereby considered available for CCS projects.

The largest CO_2 injection in a pure CCS project was applied on NCS in the Sleipner field. Since 1996, 16 Mt CO_2 have been injected into the Utsira formation at 800 meter depth (Iglauer, 2011a), which corresponds to over 2 years of CO_2 emission from all cars in Norway (Statoil, 2008). The CCS project on Sleipner is considered to be one of the global pioneers of CO_2 capture and storage (GCCSI, 2013).

CO_2 injection can be economical beneficial in both conventional and unconventional oil reservoirs as CO_2 can be used for storage and possibly recover incremental oil in the same process, called CO_2 EOR and storage (Holtz, 2009, Gozalpour, 2005). Because of the increasing interest on EOR and CO_2 emission and taxation, CO_2 EOR and storage is expected to get more focus by the oil industry in the near future.

3.1 CO_2 flooding

Carbon dioxide (CO_2) injection in oil reservoirs have been applied for 40 years since the first commercial CO_2 injection for enhanced oil recovery at SACROC Unit in Texas, 1972 (Lambert et al., 1996). The SACROC Unit is still producing one million barrels of oil per year by CO_2 flooding (Melzer, 2012). CO_2 injection into carbonate reservoirs are regarded as one the most important EOR processes in the US since the early 1980's (Manrique and Muci, 2007). In 2010, it was reported a total of 153 active CO_2 EOR projects worldwide. 139 of these projects are stationed in USA (Ahmed, 2012).

Several estimates of incremental recoveries in CO_2 floods are mentioned in the literature, from 8-16% (Lambert et al., 1996) to 7-22% (Brock and Bryan, 1989) of original oil in place. It is estimated that the "next-generation" CO_2 EOR has a potential of producing additional 67 billion barrels of oil using new techniques including injecting larger volumes of CO_2 and increasing mobility control by the use of thickeners and foams (OFE, 2013, Enick, 2012).

CO_2 EOR techniques include miscible displacement, water-alternative-gas (WAG), gravity stable displacement, "huff-and-puff" and CO_2 foam injection (mobility control). Under the right circumstances, these techniques increase the oil recovery by the use of CO_2. Despite the success of enhanced oil recovery by CO_2, the CO_2 EOR process could be improved by affordably reducing the high mobility of CO_2 compared to oil and water (Enick, 2012). The water-alternative-gas process (WAG) is often used as it reduces the amount of CO_2 used and enhances mobility control during the flood (Zolotukhin, 2000).

Experience over the years suggest that CO_2 should be used in moderately light to light reservoirs with API gravity > 25, deep enough (typically above 915 meters) to have a fracture pressure above the MMP (Enick, 2012, Farouq and Thomas, 1989). **Figure 3.1** shows an illustration of a CO_2 miscible displacement process, neglecting fluid density differences (which cause gravity override), viscosity differences (which may cause fingering of fluids) and reservoir heterogeneities like permeability differences.

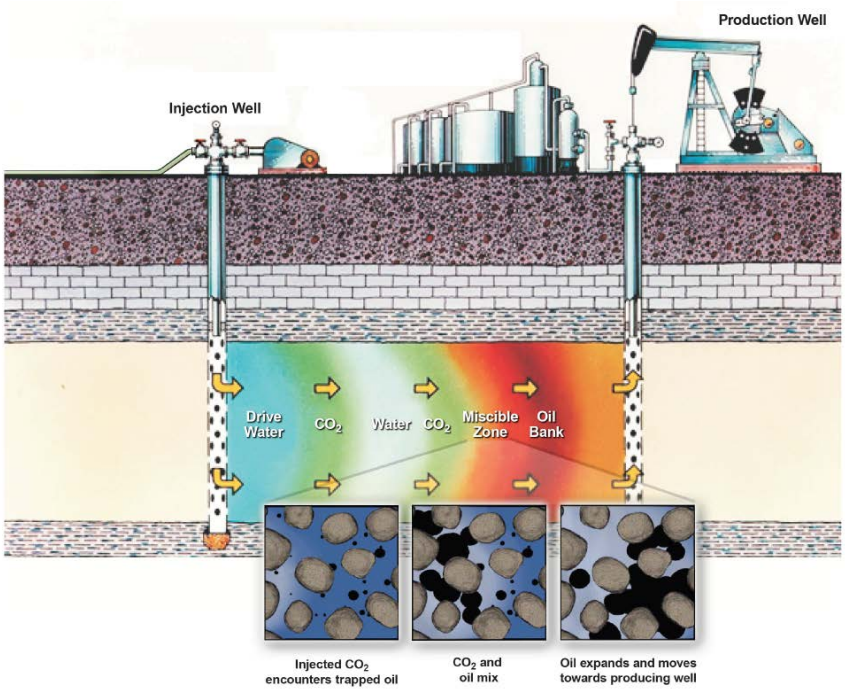

Figure 3.1: Cross-section illustrating a CO_2 miscible WAG process, displacing any residual oil from subsurface reservoir rock between the injection well and production well. From (NETL, 2010).

CO_2 EOR Field examples

The Ford Geraldine Unit field is located in west Texas and was discovered in 1956. Primary recovery yielded 18% of OOIP and was increased to 23% by secondary water injection. A good primary recovery combined with high initial water saturation in the reservoir led to poor secondary recovery. A stagnation in oil production from water injection led to miscible CO_2 injection for EOR. Favorable reservoir characteristic, availability of a CO_2 source and a good response with CO_2 injection in a geological similar field provided incentives for CO_2-flooding. Slim-tube experiments indicated miscible conditions between CO_2 and the oil and a short-term injection test showed that the reservoir would take the desired CO_2 injection rate. Miscible CO_2 injection was implemented to the field in 1981 and as a result the oil production tripled (Pittaway, 1990). Tertiary incremental oil recovery by CO_2 injection was 7% in 1992, and was estimated to increase up to 15 % of OOIP in the following decades (Lopez, 2012).

Another successful CO_2 flooding was conducted in Sundown Unit field in the San Andres formation north of Midland, Texas. CO_2 flood in this field was benefited from a good infrastructure including CO_2 supply pipelines and a large processing plant nearby to handle produced gas contaminated with CO_2. A miscible CO_2 flood pilot test was initiated in 1976 to 1984. The pilot achieved incremental oil recovery of 19% of OOIP and a full-scale CO_2 flood was implemented later the same year (Folger, 1996).

3.2 Using CO_2 as an EOR fluid

Benefits compared to other gases

CO_2 is proven to be the most efficient non-hydrocarbon solvent for both miscible and immiscible processes (Abrishami et al., 1996), but recovery enhancements depend on reservoir conditions and fluid composition. These enhancements include swelling of the oil, reduces oil viscosity, increases oil density, highly soluble in water, vaporization and extraction of hydrocarbon components up to C_{30} and reduce the interfacial tension between the oil and CO_2 (Holm, 1974, Lambert et al., 1996).

Miscible CO_2 displacements include all the enhancements mentioned above. Immiscible CO_2 displacements relies more on the reduction of viscosity of the oil phase, reduction of IFT and swelling of oil in contact with CO_2 (Brock and Bryan, 1989). The ability to extract intermediate hydrocarbon components (C_5- C_{30}) makes CO_2 an efficient solvent for heavier oil extraction in enhanced oil recovery processes (Green, 1998, Blunt, 1993).

The CO_2 dissolves into the oil phase and some light components are extracted to the CO_2 phase. Dissolved CO_2 reduces the viscosity of oil as the concentration of CO_2 increases, affecting the mobility ratio favorably, resulting in a better sweep efficiency (Holm, 1974, Miller, 1981, Barrufet, 1996). In addition, the dissolution of CO_2 causes the oil to swell up to 50-60%, which contributes to the total enhanced oil production (Firoozabadi, 2010, Iglauer, 2011b). Swelling of oil also increases the contact area between the oil and CO_2 , hence increasing the diffusion rate (Sohrabi et al., 2007).

CO_2 is unique as it achieves miscibility at a lower pressure than other gas solvents used for miscible EOR processes. This makes CO_2 a candidate for miscible displacements in reservoirs with lower API gravity, shallower depths and lower fracture pressure gradients (Ahmed, 2012). Unlike other gas solvents used for miscible processes, further oil recovery through CO_2 injection does not depend upon the presence of light components (C_2-C_4) in the reservoir oil. CO_2 is most applicable to reservoirs that has already been depleted of its gas and liquefied gas components (LPG) (Holm, 1974).

Under miscible conditions, CO_2 has the density close to that of a liquid and is higher than that of other gases used for EOR, such as nitrogen (N_2) and methane (CH_4). In addition, dissolution of CO_2 into the reservoir brine and oil preferably enhances the density differences between the two fluids. CO_2 saturated water have lower density than water while CO_2 saturated oil have higher density than oil. This contribute to more efficient vertical sweep efficiency by being less prone to gravity segregation than N_2 and CH_4 (Brock and Bryan, 1989, Bui, 2013).

Challenges compared to other gases

There are many challenges regarding injection of CO_2 for enhanced oil recovery. Apart from the economical aspect, the main challenges are related to the density and viscosity of CO_2 (Enick, 2012). First, CO_2 has much lower viscosity than the oil at reservoir conditions. The unfavorable mobility ratio between CO_2 and the reservoir oil will cause viscous fingering through the oil. In addition, CO_2 will preferably invade high permeable areas, leaving behind unswept low permeable areas that may contain large amounts of recoverable oil (Enick, 2012).

Second, CO_2 has much lower density than the oil at reservoir conditions. This may cause gravity override and poor sweep of the lower parts of the reservoir (LaForce, 2008, Enick, 2012). The extent of gravity override depends on the vertical permeability and the permeability of horizontal layers within the reservoir. In a scenario where the lower horizontal layers in the reservoir have high permeability gravity override will not dominate. Segregation of CO_2 to the top of the reservoir may be delayed in reservoirs with low vertical permeability (Skjæveland, 1992). Both cases mentioned above contribute to a poor sweep efficiency associated with early CO_2 breakthrough, high CO_2 utilization ratio, low oil production rates and low OOIP recovery (LaForce, 2008, Patel, 1987, Enick, 2012).

There are also challenges related to CO_2 sources. CO_2 flooding for EOR requires a large amount of pure CO_2. In the beginning of the CO_2 EOR era, natural CO_2 reservoirs were used as a source. Depending on the distance pipelines were made to supply the oil fields with pure natural CO_2. Today, depletion of the source fields and/or limitation on pipelines is constricting CO_2 EOR growth. The large cost of industrial CO_2 versus the cheaper natural CO_2 from fields is the largest barrier (Melzer, 2012). CO_2 is soluble in water. In most cases, CO_2 is injected with water simultaneous or as alternative slugs. This leads to some CO_2 loss in the water, but most importantly, carbonic acid is made when mixing CO_2 with water. The carbonic acid will cause severe corrosive effects on the existing pipeline systems (Lambert et al., 1996, Farouq and Thomas, 1989). Carbonic acid may also affect the strength of carbonate rocks. CO_2 enriched water at reservoir conditions causes dissolution or precipitation of the chalk material (Alam et al., 2011). This may affect the reservoir rock in terms of porosity, permeability, compaction and pore geometry.

3.2.1 Water shielding

Miscible gas injection processes has the ability to recover all the oil present in the gas flow channels (Skjæveland, 1992). The residual oil is isolated from the gas by the presence of water in dendritic structures and parts of the pore space. Water can act as a barrier preventing CO_2 from contacting the oil during a flood. CO_2 diffusion through the water barrier causes swelling of the entrapped oil. After sufficient time the swelling of the oil can eventually break the water barrier that blocked the oil, thus extract the oil (Grogan, 1987). **Figure 3.2** illustrates the process explained above.

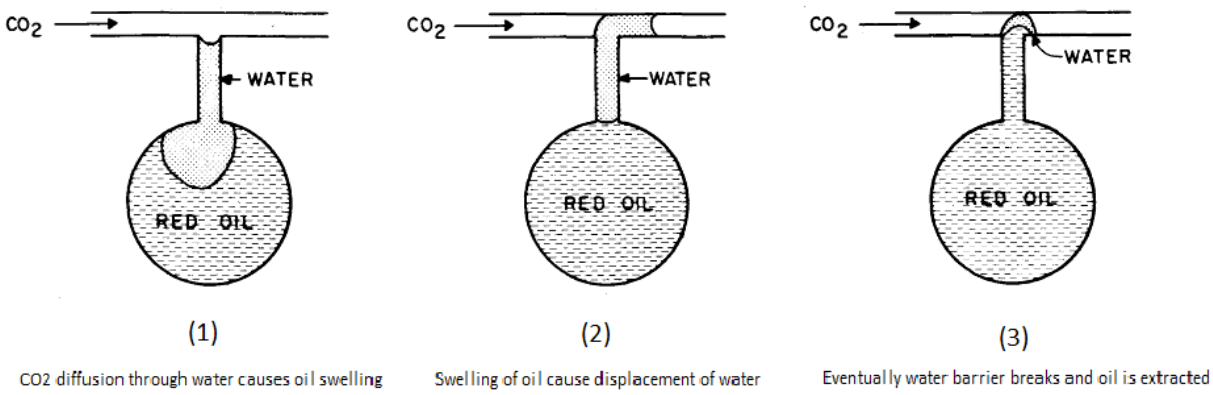

Figure 3.2: Oil recovery by CO_2 through water barrier in a dendric pore structure caused by diffusion and swelling. Modified from (Campbell, 1985).

Past studies have shown that trapping of oil by water occurs both in first-contact miscible and multi-contact miscible processes in water-wet rocks (Walsh, 1989). Water shielding is observed during miscible core floods, and is significant, especially for water-wet reservoirs, during simultaneous water/CO_2 injection (Muller, 1991). This effect can lead to a higher amount of residual oil behind a miscible displacement front.

The amount of trapped oil in mixed-wet and oil-wet are significantly less compared to water-wet cores after CO_2 miscible floods (Lin, 1990). In an oil-wet rock the water is present in the middle of the larger pores, leading to less shielding of oil that can be miscible displaced by CO_2 (Wylie et al., 1999).

3.3 Applying CO_2 in the North Sea

Many fields on NCS have already produced up to 50% OOIP resulting from an advanced increased oil recovery (IOR) technology during secondary recovery. Nevertheless, injection of CO_2 in North Sea fractured chalk reservoirs as both secondary and tertiary processes is of interest since EOR potential is large (Alavian and Whitson, 2012). In these reservoirs oil entrapment in water flooded areas is the main target for tertiary EOR processes. The residual oil may be displaced by miscible CO_2 flooding.

A recent study by NPD (2005) shows a potential of 130-150 MSm^3 of incremental oil from 20 fields that are considered as potential candidates for CO_2 injection. Amongst the candidates are Ekofisk, the largest fractured carbonate field on NCS, estimated to achieve a break-even oil price of 23-33 $/bbl, which is considered commercial with the present oil price (Skarestad, 2011). Another simulation study proved that considerably more oil could be recovered by miscible CO_2 injection on NCS, approximately 63% OOIP, compared to approximately 43% OOIP for water injection (Lindeberg and Holt, 1994).

Most reservoirs on NCS have pressures and temperatures in the region 200-300 bar and 70-130 °C. At these conditions, CO_2 act as a supercritical fluid and will be first contact miscible with the reservoir oil (Skarestad, 2011). The potential of EOR by CO_2 on NCS is present, but technically there are many challenges that can be addressed for offshore field applications (Gozalpour, 2005):

- Insufficient reservoir characterization (geology and fluids are different than in the US)
- Large space between wells
- Lifespan of offshore structures
- Extra cost to upgrade platform equipment and pipeline system to handle CO_2 (corrosive effects)
- CO_2 cost
- Transportation cost

3.4 CO_2 foam for mobility control

In general, CO_2 flooding has low sweep efficiency because of a significant difference in mobility between the CO_2 and the oil. The high mobility of CO_2 compared to oil and water results in poor vertical and horizontal sweep efficiency dominated by gravity override, gas channeling in high-permeable layers and gas coning into production wells (Zolotukhin, 2000).

Mobility control is an important factor in successful CO_2 floodings. Surfactants may be added, either simultaneous with the gas or in portions to generate foam in the pore network. The foam will reduce gas mobility by several orders of magnitude leading to a more preferable mobility ratio between the gas and the oil (Kovscek, 1993, Rossen, 1996, Farajzadeh, 2009).

The foam reduces the gas mobility, especially in high permeable layers, leading to a more stable displacement front. It may improve sweep efficiency by the diversion of CO_2 from the high permeability to the low permeability regions (Rossen, 1996, Solbakken et al., 2013).

The dependence of foam mobility control has shown to be beneficial in fracture systems (Yan and Hirasaki, 2006), since the reduction of fracture conductivity leads to significantly improved sweep efficiency (Graue and Nesse, 2002). Increasing the resistance to flow through the fractures may divert fluid flow to the matrix and displace unswept residual oil (Haugen et al., 2012). Several field tests of steam foam and CO_2 foam has been applied (Feng Li, 2010).

3.5 Physical properties of CO_2

It is important to understand the physical properties of CO_2 during floods. **Figure 3.3** shows the phase diagram of CO_2 with different temperatures and pressures. CO_2 has a sublimation point at -78.5 °C and 1 atm (1 bar), triple point at -56.6 °C and 5.11 atm (5.17 bar), and critical point at 31.1 and 72.9 atm (73.9 bar). Beyond the critical point, the CO_2 act as a supercritical fluid, with no distinctive liquid or gas preferences.

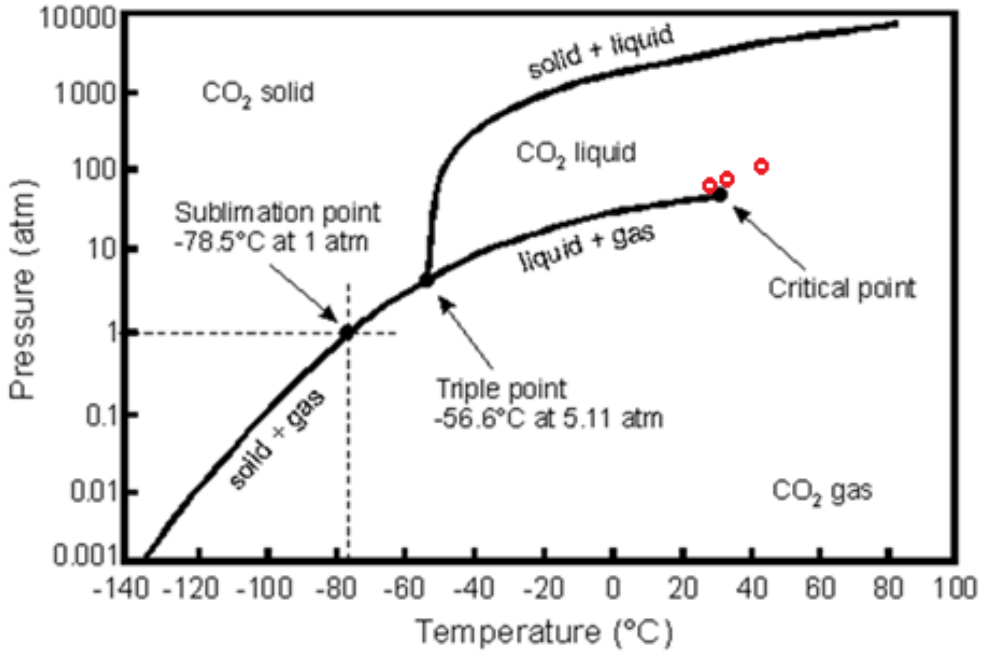

Figure 3.3: Phase diagram of CO_2. The red circles represent the experimental conditions in this thesis. Modified from (Picha, 2007).

Figure 3.4 and F**igure 3.5** show density and viscosity of CO_2 as a function of temperature and pressure, respectively. A rapid increase in density and viscosity can be noticed as CO_2 changes from gas to liquid and supercritical phase.

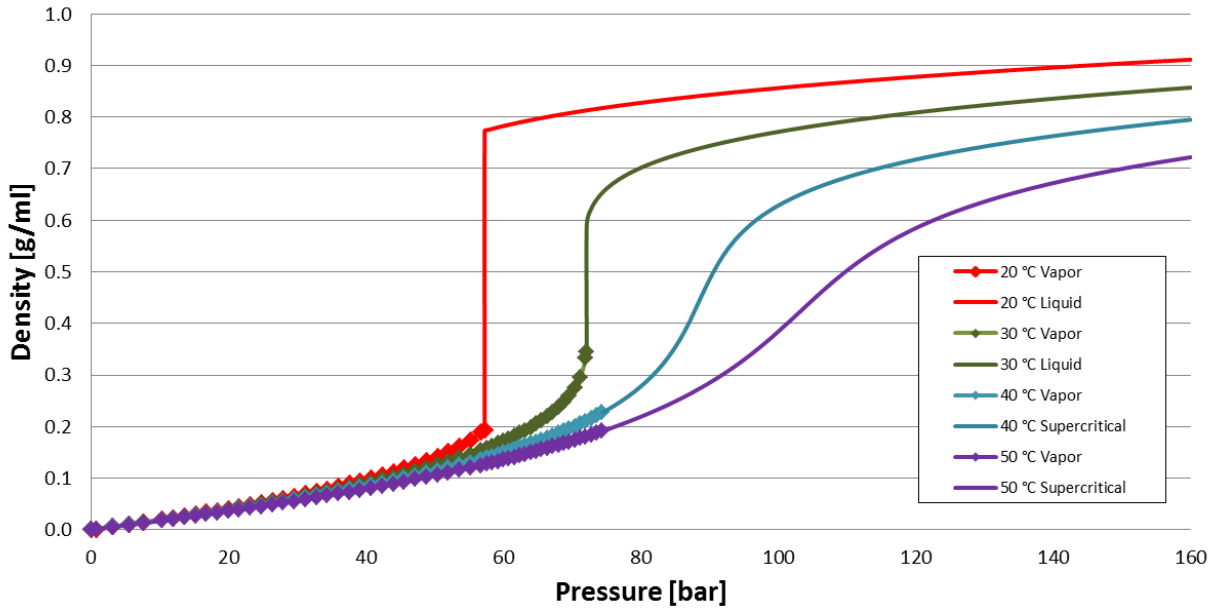

Figure 3.4: Density [g/ml] as a function of pressure [bar] for CO_2. Data obtained from (NIST, 2013).

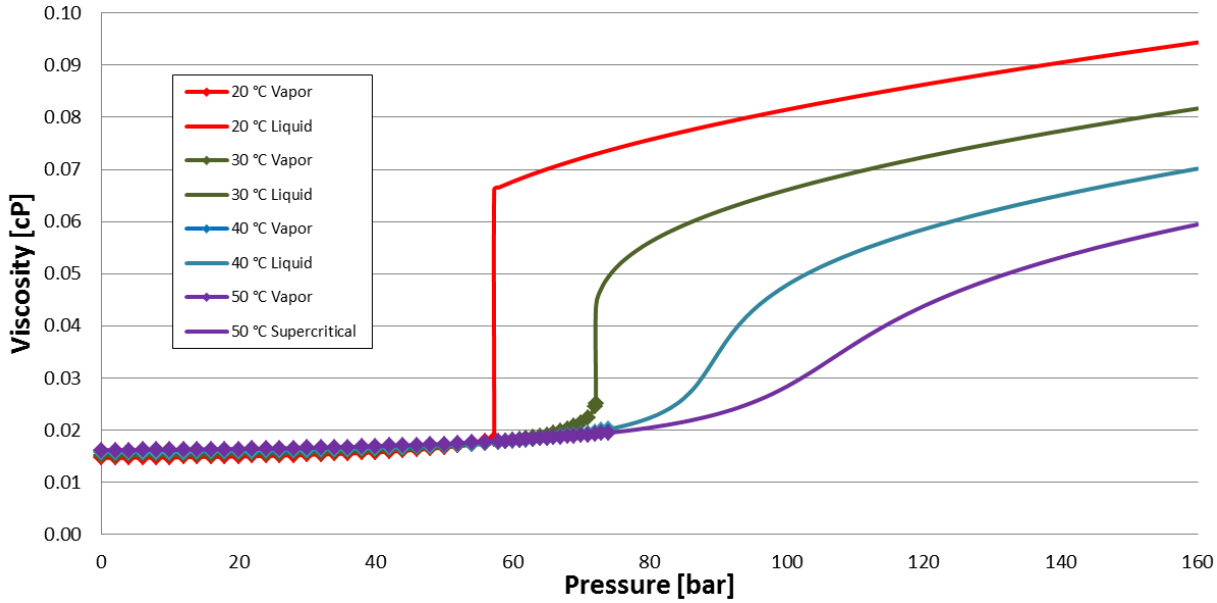

Figure 3.5: Viscosity [cP] as a function of pressure [bar] for CO_2. Data obtained from (NIST, 2013).

3.6 Miscibility between CO_2 and n-decane

In this thesis n-decane was used as the oil phase. N-decane is not influenced by pressure and temperature variations since it is composed of a single hydrocarbon component. In addition, n-decane does not affect the wettability on core samples (Graue and Nesse, 2002, Haugen et al., 2012).

All the experiments conducted in this thesis were above the minimum miscibility pressure between CO_2 and n-decane. CMG simulations have been performed by Ahmed (Ahmed, 2013), using WinProp PVT simulator to determine the MMP between CO_2 and n-decane with increasing pressure and temperature displayed in **Figure 3.6**.

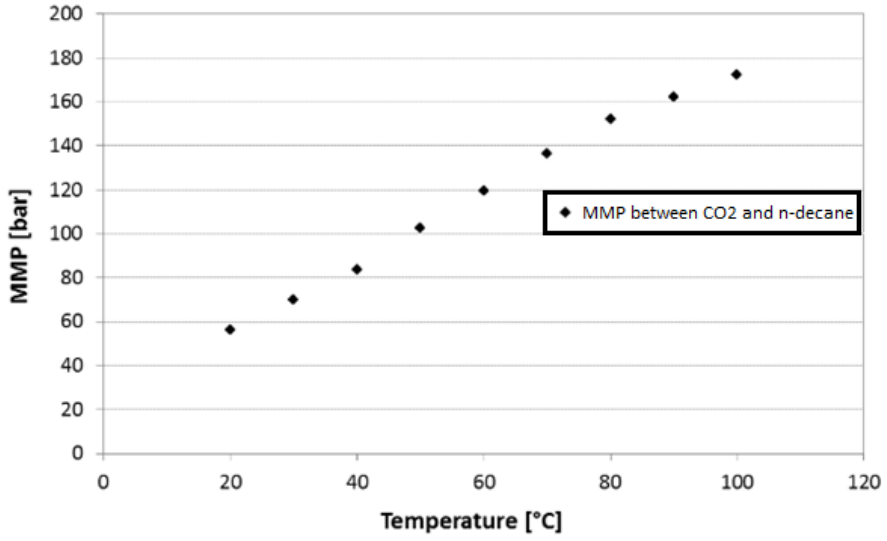

Figure 3.6: Simulation of the minimum miscibility pressure, MMP, between CO_2 and n-decane as a function of pressure and temperature using CMG simulation. Modified from (Ahmed, 2013).

Estimations of the MMP between CO_2 and n-decane by slim-tube and RBM methods have been reported in the literature. At 38 degrees the MMP was measured to be approximately 86 bar with the use of the slim-tube method and 88 bar with the rising bubble method (Elsharkawy, 1992). Others have performed the same experiments with fairly consistent results.

4 Imaging techniques

Computed tomography and positron emission tomography provide high-spatial-resolution 3D (<1mm^3) visualization of in-situ fluid flow. Data obtained are also used to determine different parameters in the rock sample such as saturation profiles and porosity measurements (Ketcham, 2001). The imaging techniques used in this thesis is briefly discussed below.

4.1 Computed Tomography (CT)

A Computed Tomography scanner, also known as a CAT (Computed Axial Tomography) scanner consists of an X-ray source and a detector. The X-ray source emits electromagnetic radiation while rotating around the sample. Detectors are positioned on the opposite side of the circle from the X-ray source. These detectors measure the X-ray attenuation as they pass through materials with different density. When electromagnetic radiation passes through matter the intensity decreases (Thorsteinsen, 1995).

The attenuation of the X-ray is affected by absorption and scattering which affects the intensity of the X-ray beam. The CT-scanner measures the linear attenuation coefficient, μ_a, for the material a. It is given in Beer-Lamberts law (Beer, 1852) given by the following equation:

$$I = I_0 e^{-\mu_a x} \tag{4.1}$$

where I_0 is the intensity of the incident beam, I, is the intensity after passing through the material and x is the thickness of the material. A large linear attenuation coefficient means that the X-rays are attenuated as it passes through material and a small attenuation coefficient means that the material is relatively transparent to the beam. The attenuation of the beam is closely related to density of the material the X-rays are passing through (Ketcham, 2001). The attenuation, thus the CT value, increases with density (Watanabe, 2011). On a CT image, high CT values represent high attenuation and thereby the bright high-density areas. Low CT values represent the darker low density areas on the image.

Figure 4.1 shows the concept of CT-scan geometry. The X-ray source rotates around the sample as it emits radiation. Detectors on the opposite side of the sample measure the extent to which the X-rays have been attenuated by the sample.

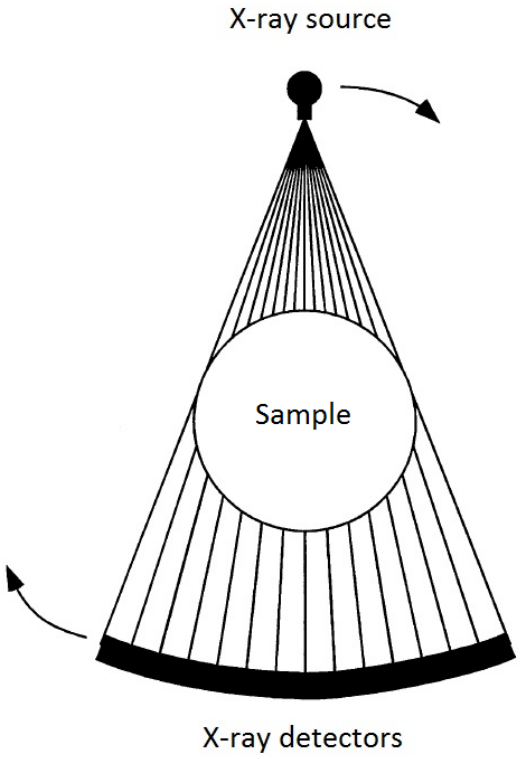

Figure 4.1: Illustration of a third generation rotate-only CT scan geometry. Modified from (Ketcham, 2001).

After rotating around the object one time, a two-dimensional image called a slice can be computed based on the density difference which is presented by CT values. The sample can be moved slightly in a lateral direction between each 2D image. Many 2D slices can then be compiled together to create a 3D representation of the sample.

4.1.1 Calculations based on CT-values

In this thesis CT-data is used for porosity and saturation measurements and to visualize a displacement process. This process requires several scans before the displacement process.

First, a dry scan of the core is needed to compute a porosity image. The core is vacuumed before the dry scan is taken. This image can be used to discover local heterogeneities within the core sample that can affect fluid flow within the rock during a flood including core damage and mud invasion (Coles, 1995). It will also function as a background image of a 3D visualization displacement process toned down to show the edges of the core sample. By applying formulas approximate values for porosity and saturation can be found. The porosity, ϕ, can be calculated by applying formula (Coles, 1995, Akin, 1999):

$$\phi = \frac{CT_{wet} - CT_{dry}}{CT_{water} - CT_{air}} \tag{4.2}$$

where CT_{dry} and CT_{wet} refer to CT values obtained from the core material saturated with air and water, respectively. CT_{water} and CT_{air} are the CT values for pure water and air. The CT numbers are given in Hounsfield units.

In order to calculate saturations during a displacement the core sample must also be scanned 100% saturated with each fluid at experimental conditions. These scans act as reference when calculating saturations. The saturation of a fluid at a given time can be calculated by applying formula (Coles, 1995, Akin, 1999):

$$S_{CO_2} = \frac{CT_{scan} - CT_{Oil}}{CT_{CO_2} - CT_{Oil}} \quad , \quad CT_{Oil} = 1 - CT_{CO_2} \tag{4.3}$$

where CT_{scan} is the CT values obtained for a fluid at an unknown saturation at a specific time step. CT_{CO2} and CT_{Oil} refer to CT values obtained from the same core material saturated with CO_2 and oil, respectively. To obtain reliable quantitative values from CT images it is important to acquire accurate CT numbers (Coles, 1995).

4.2 Positron Emission Tomography

Positron Emission Tomography (PET) uses the emitted radiation from radioactive isotopes, individually labeling fluids of interest to visualize in-situ fluid flow. The radioactive isotope, called a tracer, is produced in a cyclotron and added to the injecting fluid.

In this thesis ^{11}C was used to label CO_2. ^{11}C has a half-life of approximately 20 minutes and should be produced close to the scanner for optimal use. ^{11}C, with, is only active within a few hours. As the isotope decays, detectors placed in a circular ring around the scanned object detects the radioactive radiation. The chemical reaction, causing radiation by ^{11}C is

$$^{11}C \rightarrow {}^{11}B + e^{+} + \nu_e + 0.96MeV \tag{4.4}$$

$$^{11}C + e^{-} \rightarrow {}^{11}B + \nu_e + 3.17MeV \tag{4.5}$$

Most of the β^{+}-decay by ^{11}C is positron emission (99.8%). The positron loses its kinetic energy caused by interaction with nearby materials. Eventually the kinetic energy of the positron becomes the same as the rest energy of an electron, 0.511 MeV. This ultimately leads to a collision between the positron and an electron. The positron-electron annihilation emits two gamma-rays (photons), each with energy of 0.511 MeV, close to the opposite direction of each other. These gamma-rays are detected by the PET scanner, calculating the exact position where the collision took place (Bailey, 2006).

The fact that the emitted photons are not exactly in the opposite direction of each other, combined with the delay in time between the release of a positron before it collide with an electron, add some uncertainty to PET scanning (Bailey, 2006). This generally leads to a lower resolution than other imaging techniques.

5 Experimental procedures

In this chapter the experimental part of the thesis will be described. It includes rock material, fluids, routine core analysis methods and experimental setups.

Table 5.1 lists the experiments presented in this thesis. Two supercritical CO_2 injections into Rørdal chalk cores were performed in the CT lab at ConocoPhillips Research center in Bartlesville, Oklahoma. 6 supercritical CO_2 injections were run in the lab at University of Bergen. One supercritical CO_2 injection into reservoir shale cores were run at Texas A&M in College Station, Texas. A visualization study using ^{11}C to label liquid CO_2 in Bentheimer sandstone was performed at Haukeland University Hospital, Bergen.

Table 5.1: Experimental overview.

Core Material	Experiment type	Location
Rørdal Chalk	Supercritical CO_2 injection	University of Bergen
Rørdal Chalk	Supercritical CO_2 injection in CT	ConocoPhillips, Bartlesville, Oklahoma, US
Bentheimer Sandstone	Liquid CO_2 injection in PET/CT	Haukeland University Hospital
Shale	Supercritical CO_2 injection in CT	Texas A&M, College Station, Texas, US

5.1 Rock material

In this section the rock material used in this thesis is presented. Conducting experimental work on rock cores similar to the reservoir rocks is important for the understanding and evaluation of petroleum reservoirs in general. Physical preferences on core samples taken from a reservoir may change as it is taken from reservoir conditions to the surface. Because it is both expensive and difficult to get reservoir core samples, outcrop cores that are similar to the reservoir rock are used frequently for experimental studies (Fernø et al., 2010). Three types of rock have been used in this thesis; Portland Rørdal chalk, Bentheimer sandstone and reservoir shale rock.

5.1.1 Portland Rørdal chalk

Rørdal chalk cores from Portland cement factory in Ålborg, Danmark have been used in this thesis. This chalk originates from the Maastrichan age and is mainly composed of carbonate minerals, formed under deep marine conditions from a gradual accumulation of micro-organisms called coccolithophores (Ekdale, 1993). It presents permeability and porosity in the range of 1-4mD and 45-48% (Graue et al., 1999), respectively, and consist of 50% calcite (Ca-compounds) and 50% of silicia and clay (Si-compounds) (Hjuler, 2007). **Figure 5.1** displays a high resolution microscopic picture of Rørdal chalk compared to a picture of offshore Ekofisk chalk, accomplished by high magnification scanning electron microscopy (SEM). A resemblance can be observed.

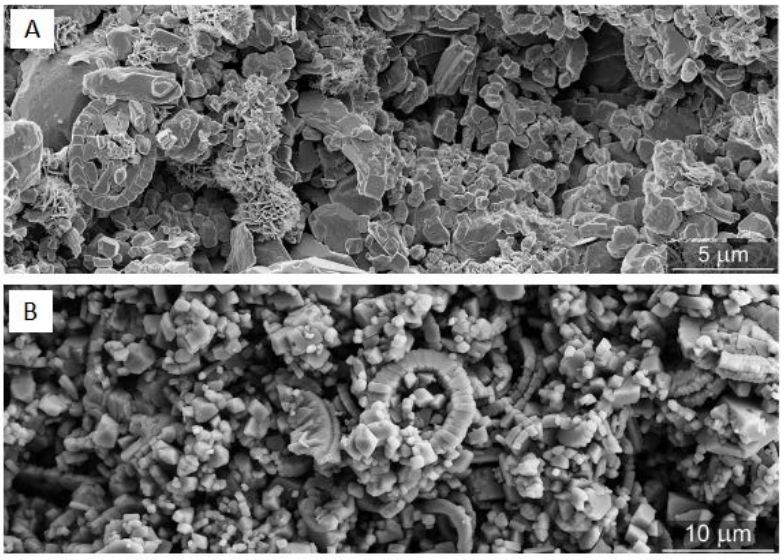

Figure 5.1: High resolution microscopic imaging (SEM) of (A) Rørdal chalk outcrop and (B) offshore Ekofisk chalk. Modified from (Hjuler, 2007).

Geomechanically, chalk from the Ekofisk field and Valhall field resembles the Rørdal chalk. These outcrops are suitable for comparability provided that porosity and permeability of the outcrop and reservoir chalk are similar (Graue et al., 1999, Haugen et al., 2012, Hjuler, 2007). Wettability of the Rørdal chalk has been studied extensively. In most cases, either cores or outcrops which has been cleaned, is or becomes water-wet (Hedegaard, 2011, Johannesen, 2008). For this reason wettability measurements have not been applied in this thesis.

5.1.2 Bentheimer sandstone

Bentheimer sandstone was used to visualize flow of CO_2 in a PET/CT scanner. It is heterogeneously composed of 95% quartz, 3% clays and less than 2 % feldspars and presents a porosity and permeability in the range of 23-25% and 1-3 D, respectively (Dautriat, 2007). The high permeability and connectivity in this type of rock leads to a faster diffusion process as the labeling radioactive tracer ^{11}C has such a short lifespan.

5.1.3 Shale

Shale is formed from fine-grained sediments under the influence of high pressure and temperature over geological time (Oyekunle, 2013). It is mainly composed of clay minerals (mud-size particles less than 64 micrometer) with a permeability in the order of nanodarcies (Tinni, 2012, Metwally, 2010). Producing hydrocarbons from shale reservoirs requires hydraulic fracturing of the tight layered shale along with horizontal wells (Tinni, 2012). **Figure 5.2** displays the two shale cores used in this thesis.

Figure 5.2: Reservoir shale cores containing light crude oil.

5.2 Fluids

Table 5.2 lists all the fluids used in this thesis including the densities and viscosity at experimental conditions when available. To represent the reservoir brine and oil phase, synthetic brine from the Ekofisk field and n-decane have been used in the experimental work. The synthetic Ekofisk brine was made in the laboratory mixing the salts with distilled water. 5 wt. % CaCl2 was added to hinder dissolution of the chalk and 0.01 wt. % NaN3 (sodium acid) was added to hinder bacterial growth (Graue et al., 1999).

Using n-decane offers a high degree of reproducibility in experiments because of its stable and repeatable wettability preference and thus suited for this type of study (Haugen et al., 2012). Both n-decane and the reservoir brine have a representative viscosity ratio at room temperature compared to reservoir fluids at reservoir temperature and pressure (Graue and Nesse, 2002).

During the CT scanner experiment, Iododecane was mixed with the oil with a ratio of 1/10 to increase the contrast of the CT-numbers between the oil phase and CO_2 phase during the CT-scan. It was assumed that the Iododecane had no significant effect on the properties of n-decane. The surfactant AOS ($C_{14/16}$) was used for foam generation.

Table 5.2: Fluid overview

Fluid	Contents	Density [g/ml]	Viscosity [cP]	Condition
Carbon dioxide	> 99.999 % CO_2	0.784	0.068	25 °C, 83 bar
		0.662	0.051	35 °C, 90 bar
		0.638	0.049	42 °C, 107 bar
n-decane	$C_{10}H_{22}$	0.733	0.933	25 °C, 83 bar
		0.726	0.818	35 °C, 90 bar
		0.722	0.761	42 °C, 107 bar
Ekofisk brine	Distilled water 5 wt. % NaCl 5 wt. % NaCl 0.01 wt. % NaN_3	1.050	1.090	20 °C, 1 bar
Iododecane	$C_{10}H_{21}I$	1.201	n/a	20 °C, 1 bar
AOS C14/16	Distilled water 1 wt. % NaCl 1 wt. % P-C1	n/a	n/a	n/a

5.3 Routine core analysis

5.3.1 Porosity measurement

The saturation method was used to measure porosity. This method involves measuring the mass of the core sample before and after the sample is saturated with a fluid. The mass difference is measured corresponding to the total the volume of fluid that has saturated the sample.

This volume corresponds to the total pore volume of the core assuming that it is 100% saturated with the fluid. The density of the fluid used is known and the bulk volume, pore volume and porosity can be calculated using material balance (Graue, 2006).

The chalk core is cut from an outcrop before the core surface is cleaned by hand with Ekofisk brine and then dried at 80 °C for 24 hours in a heating cabinet. The length and width of the core sample are measured with a caliper before it is saturated with a liquid in a vacuum apparatus.

Saturating the core

Two methods of saturating the core samples have been applied in this thesis. Both methods use the principle of the saturation method, as explained above, but with a slightly different procedure.

Figure 5.3 shows the first method of saturating the core with the use of a vacuum apparatus. The Ekofisk brine was vacuumed to a pressure below 10 mbar and the core was vacuumed to below 1 mbar before saturation. It is important to get below these pressures to avoid underestimating the porosity and avoid getting air inside the core, leading to a three phase system.

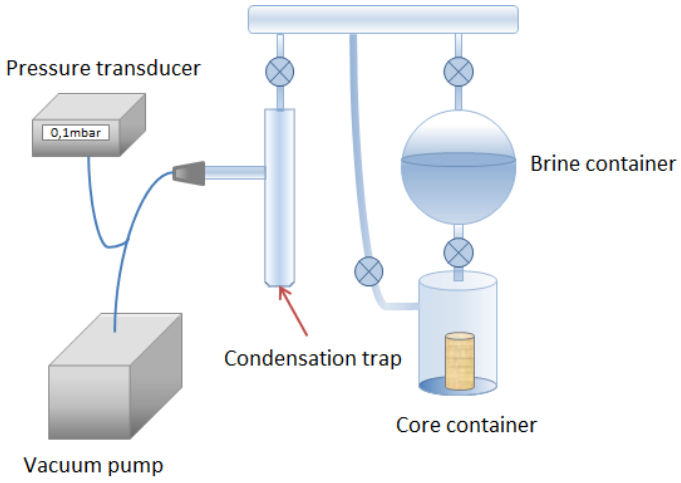

Figure 5.3: Experimental procedure of measuring porosity in a vacuum apparatus. Modified from (Christophersen, 2012).

The second method is to saturate the core in the core holder itself. This is the best suited method when using a CT/PET scanner to avoid movement of the core holder between scans. It is also less time consuming when using fractured core samples.

Figure 5.4 shows the experimental setup when saturating an air filled core sample directly in the core holder. Both end pieces have a valve to close the desirable connections whereas one was connected to a vacuum pump and the other was connected with a pipe to a cylinder filled with oil. The core sample is vacuumed below 1 mbar before it is spontaneously saturated with oil. By measuring how much oil the core is saturated with minus the dead volume, pore volume and porosity can be calculated by material balance.

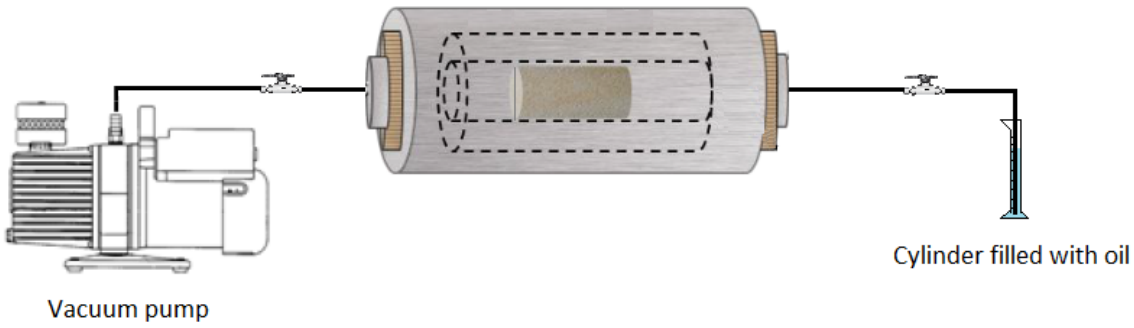

Figure 5.4: Illustration of saturating the core directly in the core holder.

5.3.2 Permeability measurement

Permeability measurements were conducted using the method described in section 1.2.1, by the use of Darcy's law. Assuming that the cores were 100% saturated with the Ekofisk brine, the cores were flooded with several constant injection rates until the differential pressure stabilized. **Figure 5.5** shows the experimental for permeability measurements.

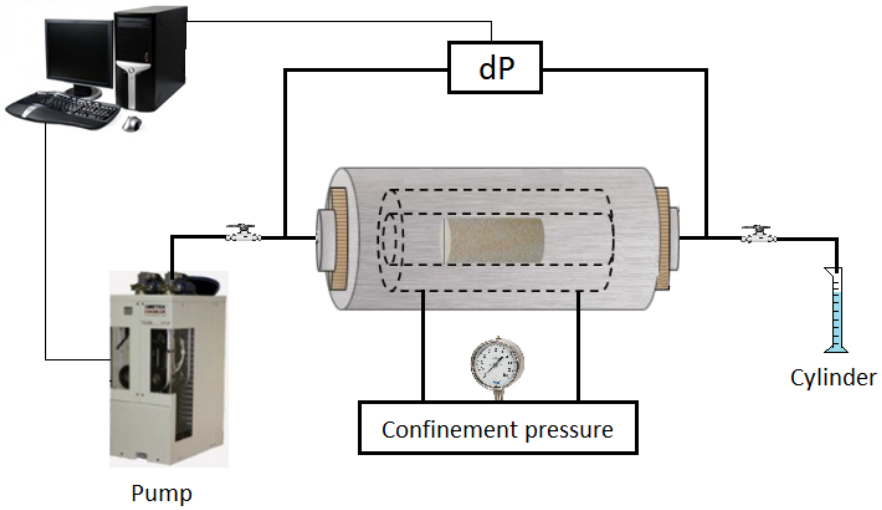

Figure 5.5: Experimental setup for measuring absolute permeability. The same setup is used when draining the cores.

5.3.3 Drainage

The brine saturated core samples were drained with n-decane until the irreducible water saturation was obtained. The cores were drained with up to 4 PV of Ekofisk brine in both directions of the core with a differential pressure equivalent to 2 bar/cm of their length until the brine production stagnated. The experimental setup was identical for permeability measurements, displayed in **Figure 5.5**. The injection rate during permeability measurements was slowly increased to the desired rate to control the buildup of the differential pressure versus the confinement pressure. This procedure was followed to avoid rapid changes in pressure and possibly damage the core plugs.

5.3.4 Fracturing the core samples

In order to study recovery mechanisms by CO_2 in fractured reservoirs, most of the cores were cut along the center of the cylinder axis with a band saw to represent a fracture. The cores diameter become 1 mm less from the width of the saw blade and fracture surface becomes smooth with no roughness.

Two methods of calculating the new pore volume after fracturing was applied. The first method was to subtract the volume removed by the saw blade and the second method was to measure the weight difference before and after cutting the core. Both methods included the assumptions that the porosity distribution and fluid saturations did not change upon cutting the core.

Assuming that the volume removed has the shape of a rectangular box the new pore volume can be calculated by subtracting the fracture volume, *V*, from the initial pore volume, PV:

$$PV_{frac} = PV - (\phi \cdot V_{fracture}) \quad , \quad V_{fracture} = L \cdot D \cdot D_{cut} \tag{5.1}$$

where PV_{frac} is the pore volume after fracturing, is the measured porosity, *L* is the length of the core, *D* is the initial diameter and D_{cut} is the diameter of the part that are cut away perpendicular to the fracture plane. The new porosity can also be estimated using weight measurements:

$$PV_{frac} = PV \cdot \frac{m_{frac}}{m_{initial}} \tag{5.2}$$

where m_{frac} is the weight of the core after cutting and $m_{initial}$ is the initial weight of the core. Some of the cores where cut dry and saturated directly in the core holder as explained in section 5.3. In these cases the pore volume was measured based on the volume of oil that imbibed into the core and the dead volume of the core holder.

To allow reproducibility in experiments with the same fracture permeability and fracture-to-matrix transmissibility, a special designed spacer was placed in the fracture (see **Figure 5.6**). The spacer was 1 mm thick and made of polyoxymethylene (Pomeroy, 1933). It contained three separate partments connected with high conductivity flow channels. Each of these partments represents an open fracture with 1 mm width.

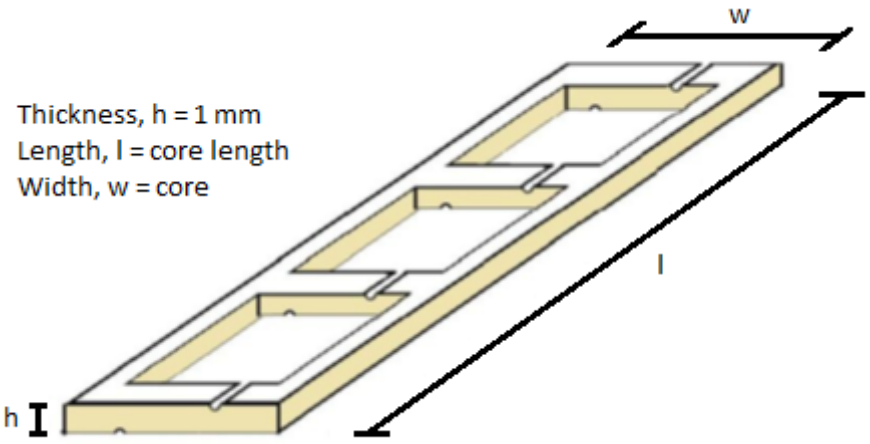

Figure 5.6: POM spacer with three separate apartments to simulate open fractures.

5.4 Supercritical CO_2 injection by material balance

A total of 6 material balance experiments were conducted in the lab at University of Bergen. All experiments were performed with a horizontally aligned core plug with a vertical fracture. The objective was to study oil recovery mechanism in fractured Rørdal chalk cores through CO_2 diffusion and to reproduce one of the experiments conducted at ConocoPhillips research center in Bartlesville.

The experimental equipment was built in a newly acquired heating cabinet large enough to contain the accumulator (buffer) with CO_2 in addition to the core holder. This gave the opportunity to warm up and stabilize the CO_2 at experimental conditions before injection to the core. An overview over the experiments is given in **Table 5.3**.

Table 5.3: Overview of all material balance CO_2 injection experiments.

Core ID	Fractured	Siw [%]	Average P [bar]	Average T [^oC]	Injection rate [ml/h]
CHR_CO2D_2	Yes	0	89.7	35.0	3
CHR_CO2D_5	Yes	0	89.9	35.0	3
CHR_CO2D_14	No	0	90.0	35.0	3
CHR_CO2D_08	Yes	21.9	90.3	35.0	3
CHR_CO2D_11	Yes	11.3	90.0	35.0	3
CHR_CO2D_12	Yes	21.7	90.0	35.0	3

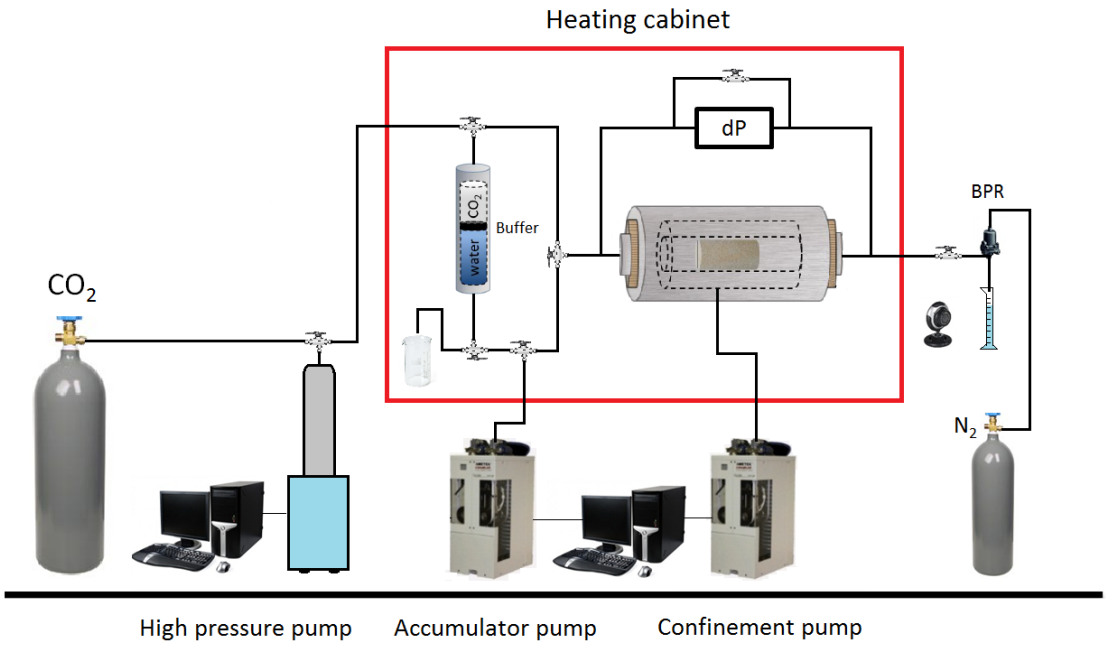

Figure 5.7: Illustration of experimental setup at University of Bergen.

Equipment used:

- Heating cabinet
- Computer for logging and operating pumps
- Hassler steel core holder
- *Quizix SP-5200* pump for confinement oil
- *Quizix QX-6000* pump for pressurizing the system with n-decane and driving the accumulator
- *Sanchez ST* pump for pressurizing the accumulator with CO_2
- *Validyne P61* differential pressure transducer
- *ESI 200* pressure transducer for measuring line pressure
- Back pressure regulator controlled by nitrogen to adjust line pressure
- *Swagelock* tubings,fittings and valves
- Web camera for monitoring production
- POM spacer to create a fracture through the core sample
- Steel accumulator (buffer) to store heated and pressurized CO_2 before injection

5.4.1 Procedure

The experimental setup is shown in **Figure 5.7**. Rørdal chalk cores were cut from an outcrop and fractured as explained in section 5.6. Porosity and permeability measurements were performed as explained in section 5.3 and 5.4. Some of the cores were drained to the irreducible water saturation (see section 5.5). **Figure 5.8** shows the preparation of the cores. The core was wrapped with aluminum folio to protect the sleeve from CO_2, equipped with POM spacers to simulate fractures (see section 5.6) and assembled in the core holder.

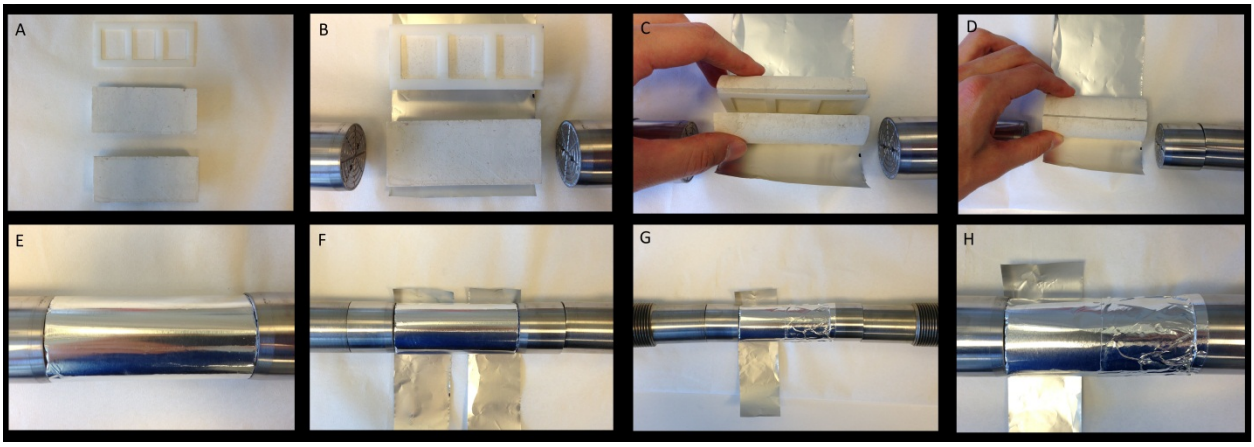

Figure 5.8: Preparation of the cores before experiments. Aluminum folio is wrapped around the core sample to protect the sleeve from CO_2.

The core holder was placed inside the heating cabinet in a horizontal alignment with a vertical fracture plane. CO_2 was transferred to the accumulator through a high pressure pump and stabilized at experimental conditions (P = 90 bar, T = 35 °C). At these conditions CO_2 is in a supercritical state and is first contact miscible with n-decane as shown in **Figure 3.6**. Fluid properties are given in **Table 5.2**.

The system was flushed and pressurized with n-decane to experimental conditions. A back pressure regulator, adjusted with Nitrogen, was used to control the pore pressure during the experiment. The confinement pressure was kept 10 bar above the line pressure to avoid leaks into or from the confinement chamber and also prevent damaging the core.

CO_2 was injected through the core at a constant injection rate of 3 ml/h for 5 days. Computers logged the line pressure and confinement pressure during the experiments. A web camera was used to capture oil production in a graduated cylinder downstream of the BPR.

The differential pressure across the core remained low during experiments because of the high conductivity through the fracture. For this reason, the differential pressure measurement was removed in subsequent tests to reduce the dead volume and to reduce some loss of CO_2 caused by diffusion into these lines.

5.5 Supercritical CO_2 and CO_2-foam injection visualized in CT

Two experiments were conducted in the CT-scanner at ConocoPhillips Research center. Both experiments were performed in a horizontal alignment with a vertical fracture. The objective was to study recovery mechanisms by CO_2 diffusion and CO_2-foam for mobility control including diffusion taking place. The first experiment was pure CO_2 injection at a low injection rate to study the effects of diffusion as a recovery mechanism. In the second experiment a surfactant was added to observe the impact of CO_2-foam in a similar experiment.

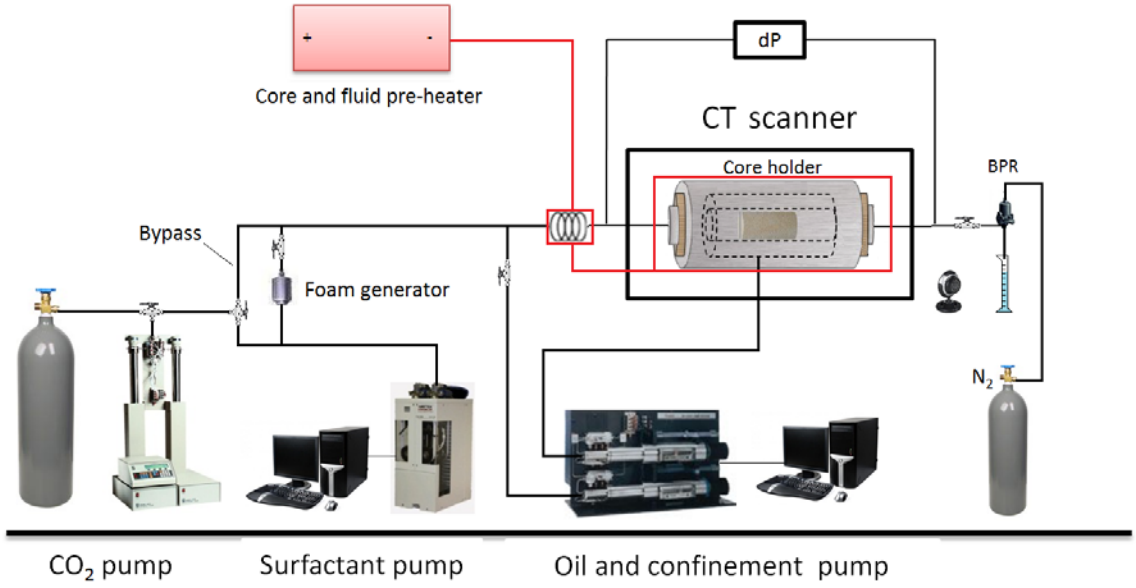

Figure 5.9: Illustration of the experimental setup at ConocoPhillips Research center.

Equipment used:

- *Toshiba Aquilion* medical CT scanner (129kV & 200 mA)
- 2x computers for line pressure logging and operating pumps
- Temco carbon fibre core holder
- 2x *Quizix SP-5200* pump for pressurizing the system with oil pre-flood and confinement pressure
- *Quizix QX-4000* pump for surfactant injection during the foam experiment
- *Teledyne Isco High Pressure* pump for CO_2 injection
- 2x *Validyne DP15* pressure transducers for measuring differential pressure
- Electrical heater system connected to the fluid-preheater including the core holder
- Back pressure regulator controlled by nitrogen to adjust line pressure
- Enclosed sand pack for pre-generating foam
- Shrink sleeve to protect the core sample
- *Swagelock* and *autoclave* tubings,fittings and valves
- Vacuum pump
- Web camera for monitoring production overnight
- 2x Rørdal chalk cores (38 mm diameter and 86 mm long)
- POM spacer

5.5.1 Procedure

The experimental setup is illustrated in **Figure 5.9**. Two 1.5 inch Rørdal chalk cores were cut and fractured as described in section 5.6. The spacers were made and fitted to the fractures. The core was fitted with a Teflon shrink sleeve. A plastic tube with holes was placed over the sleeve to keep the core stabilized and prevent it from getting damaged by confinement pressure. **Figure 5.10** shows how the core holder was assembled before placed horizontally in the CT scanner.

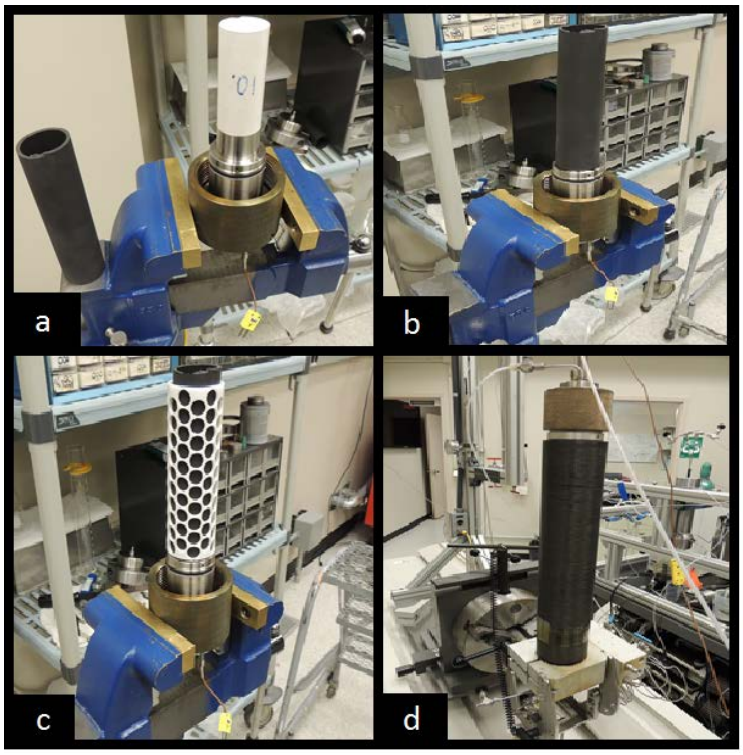

Figure 5.10: The different steps when assembling the core sample in the Temco carbon fibre core holder.

To calculate fluid saturations during the CO_2-flood the core was scanned 100% saturated with each fluid, as described in section 4.1.1. First, the core was scanned to localize its position and to make sure that the fracture plane was vertical. A pump was used to vacuum the core for two hours before the dry scan was taken.

The system was slowly pressurized with CO_2 and left overnight to stabilize before the 100% CO_2 saturated scan was taken. The Isco pump had to be refilled with CO_2 during the procedure of pressurizing. At approximately 76 bars the CO_2 changes phase from gas to liquid causing the pressure to increase rapidly after this point.

The system was depressurized to prepare the 100% saturated n-decane scan. The system was vacuumed before saturated with oil as described in section 5.3.1. The system was pressurized and the 100% oil saturated scan was taken. All the 100% scans were taken at experimental conditions.

The confinement pressure was kept 10 bars above the line pressure to avoid leaks into or from the confinement chamber and also prevent damaging the core. A pre-heater connected to the core holder warmed up the system. The expansion of CO_2 as it gets warmed up by the pre-heater system had to be taken into consideration. Both experiments were conducted at supercritical CO_2 conditions at 107 bars and 42 °C, to ensure first contact miscibility between n-decane and CO_2, as can be seen from **Figure 3.6**.

Supercritical CO_2 injection

CO_2 was injected into the core 100% oil saturated core with a constant injection rate of 0.03 ml/min at ambient conditions (P = 107 bar, T ~ 20 °C) for 6 days. Oil production was measured consequently by a web camera. Most of the production was expected to occur in the early stages of the experiment. To capture this CT scans were taken every 20 minutes at first. As the production rate declined less CT scans were taken. It takes approximately two minutes to conduct a CT scan and a total of 30 scans were taken during the experiment.

Supercritical CO_2-foam injection

A surfactant solution was co-injected with CO_2 (90% gas fraction) at ambient conditions (P = 107 bar, T ~ 20 °C) for 3 days. The surfactant (AOS C14/16) was mixed with CO_2 through a sand pack mounted on the inlet side of the core to inject pre-generated CO_2 foam. The injection rate of CO_2 was kept the same as in the supercritical CO_2 injection.

5.6 CMG GEM simulation

Numerical simulations have been performed with CMG GEM simulator to reproduce experimental results from the supercritical CO_2 injection described in chapter 5.5.

Figure 5.11 shows an illustration of the area in the core that was numerically modeled to investigate oil recovery by diffusion (red color on the left image) and the associated grid to replicate this area of the core (right image). The grid dimensions were 34 * 21 * 1 in x, y and z direction, respectively. The grid did not contain any wells. Instead, two areas were made to study mass transfer by diffusion between matrix and fracture without viscous forces present. The blue area represents the fracture and only contains CO_2. The red area represents the matrix and only contains n-decane. The fracture area was made significantly larger than the matrix area with infinitely high permeability to maintain a 100% CO_2 saturation in the fracture at all times. Because of concentration differences the simulator will try to equilibrate fluid composition between matrix and fracture. Diffusion of CO_2 from the fracture area into the matrix area occurs at the bottom of the matrix in addition to both sides to represent diffusion from the end pieces. The matrix area was refined to a fine grid at the boundaries to reduce simulation time and numerical dispersion. Similar procedure was reported by Alavian and Whitson when modeling a miscible CO_2 injection into a chalk core based on data reported by Darvish (Alavian and Whitson, 2012, Darvish, 2007).

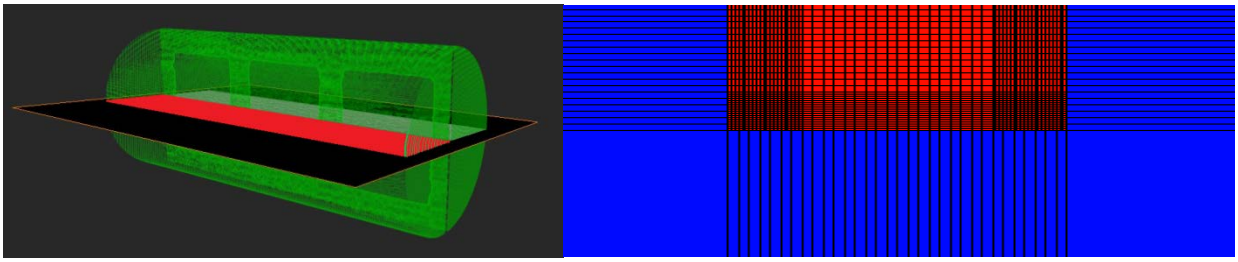

Figure 5.11: On the left: an illustration of the area in the core that was numerically modeled to investigate oil recovery by diffusion (red color) from the fracture into the matrix. On the right: Image of the grid modeled in CMG GEM. The red area on the grid represents the matrix and the blue area represents the fracture area with a 100% CO_2 saturation at all times.

Core properties such as porosity, permeability, relative permeability and capillary pressure were defined. The irreducible water saturation in the matrix was set to zero. A linear gas-oil relative permeability and a water-oil relative permeability curve for chalk taken from the literature were used in the simulation.

CMG GEM includes several methods of estimating the diffusion processes, each distinctive method are applied to the simulation with the use of a keyword. The keyword *DIFFC-OIL was used to be able to change the diffusion coefficient to match the experimental production profiles. *DIFFC-OIL specifies the Lake correlation for molecular diffusion (Lake, 1989). Oil swelling was not included to reduce simulation time. Oil production graphs from the matrix were calculated and the diffusion coefficient was varied until a good match between the experimental and the simulated values were obtained. The effective diffusion coefficient was calculated by the following equation (Alavian and Whitson, 2012):

$$D_e = D_i \phi^{(m-1)} \tag{5.3}$$

where D_e is the effective diffusion coefficient in the porous media, D_i is the estimated diffusion coefficient in absence of porous media found in the simulation, ϕ is the porosity and m is the cementation factor. The cementation factor was assumed to be equal to 2.5 based on values found in the literature from fractured chalk reservoirs, in this case the Valhall field (Olsen, 2007). This value was used since Valhall chalk resembles the Rørdal chalk used in the supercritical CO_2 injection experiment (Hjuler, 2007).

5.7 Liquid CO_2 injection labeled with ^{11}C visualized in PET/CT

The PET/CT scanner used in this thesis, located at Haukeland University Hospital in Bergen, is conducting both CT- and PET examinations at the same time. PET-data alone does not reproduce the shape and density of the core sample. By merging PET with CT, a 3D visualization of the core sample and the injected fluid can be computed. The PET/CT scanner is mainly used for patients undergoing cancer treatment in weekdays and experiments conducted by the Reservoir Physics group at UoB are performed during weekends.

Experiments were performed using radioactive ^{11}C as a tracer labeling the CO_2 phase during displacements. A total of 4 experiments involving ^{11}C were conducted in the medical PET/CT scanner at Haukeland. 3 of them involved CO_2 sequestration presented elsewhere (Mathiassen, 2013).

The experiment presented in this thesis involves displacement by CO_2 in a 100% oil saturated fractured core. The objective was to investigate recovery mechanisms by CO_2 diffusion and if ^{11}C is suitable for labeling the CO_2 phase during core floods as an imaging technique.

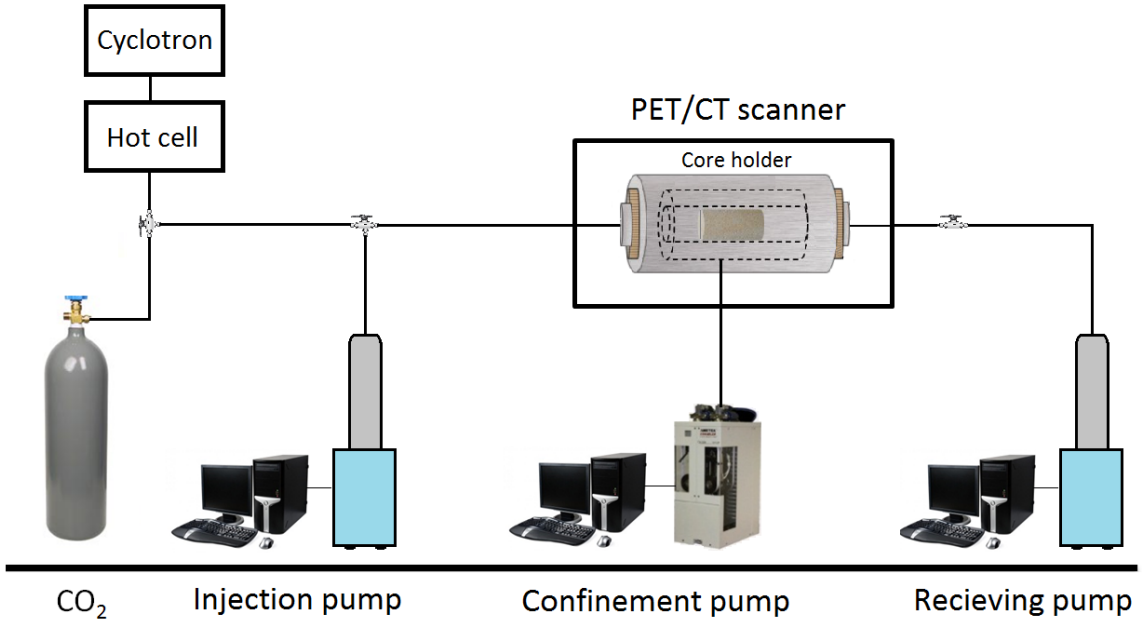

Figure 5.12: Illustration of the experimental setup at Haukeland University Hospital.

Equipment used:

- *Siemens Biograph™ TruePoint™* medical PET/CT scanner
- 2x computers for logging and operating pumps
- Hassler steel core holder
- *Quizix SP-5200* Pump System for confinement pressure
- 2x *Sanchez ST* Pump systems for pressurizing the system with CO2 pre-flood, injection of CO2 with 11C during the experiment and one as a receiving pump
- *Swagelock* and *Autoclave* tubings,fittings and valves
- Vacuum pump
- *Bentheimer* sandstone (38 mm diameter and 86 mm long)
- POM spacer

5.7.1 Procedure

The experimental setup is shown in **Figure 5.12**. A 2 inch Bentheimer sandstone was fractured, prepared and wrapped in aluminum folio as explained in section 5.6. Before the experiment, 100% saturated scans of all fluids at experimental conditions (P = 83 bar, T = 25 °C) were obtained. At these conditions CO_2 is in liquid state and is first-contact miscible with n-decane, as seen from **Figure 3.6**.

The core holder was placed horizontally in the PET/CT scanner and all the equipment was set up in the CT/PET lab. A dry scan was taken to find the position of the core and to ensure that the fracture plane was vertical. CO_2 was introduced to the core and slowly pressurized experimental conditions before the 100% CO_2 saturated scan was taken. The confinement pressure was kept 15 bar above the line pressure at all times to avoid leaks into or from the confinement chamber and also prevent damaging the core.

The system was depressurized with a vacuum pump below 1mbar and saturated with n-decane as explained in section 5.3.1. A pump was used to pressurize the system to experimental conditions, before the 100% oil saturated scan was taken. All the necessary scans were now taken and the experiment was ready to start.

Radioactive ^{11}C was delivered through a Hot Cell located in a separate lab than the CT/PET scanner. For this reason the equipment was mounted on a mobile chart to be able to transport the equipment from the Hot Cell to the CT/PET lab after delivery of ^{11}C.

Generation of ^{11}C takes place in a cyclotron controlled by a radiologist. More information about this process is mentioned in section 4.2. The ^{11}C was delivered in the Hot Cell through a pipe network from the cyclotron and transferred to the injection pump. The injection pump containing ^{11}C was then filled

with CO_2 and pressurized to experimental pressure. After a few minutes to let the fluids stabilize the injection pump, including associated equipment, was assembled and transported to the CT/PET lab.
The core holder was already mounted horizontally in the CT/PET scanner from the 100% saturation scans. The injection pump was connected to the core holder and injection into the core was commenced. A constant rate of 60 ml/h was injected to rapidly displace the oil in the fracture, before the rate was adjusted to 9 ml/h to let the main recovery mechanism be CO_2 diffusion from the fracture into the matrix. CO_2 was injected into the core for a total of 12 hours and the PET sequence lasted for three hours.

^{11}C was mixed with the injected CO_2 two times during the experiment. Further in this thesis injection of such a mixture is referred to as a PET cycle. A PET cycle involves mixing ^{11}C with CO_2 such that the injected CO_2 becomes radioactive for a short time period to be visualized using the PET scanner. The first PET cycle was conducted at experimental start, and the second PET cycle was conducted 12 hours into the experiment. The whole experiment lasted for 2 days and during this time a constant rate of 9 ml/h was kept.

5.8 Supercritical CO_2 flooding in reservoir shale cores in CT scanner

One experiment was conducted in the CT scanner located at Texas A&M University in order to investigate if oil could be recovered from two reservoir shale cores by CO_2 diffusion. Several reservoir shale cores were acquired from a company through collaboration with Texas A&M. Two of these cores were used in the experiment.

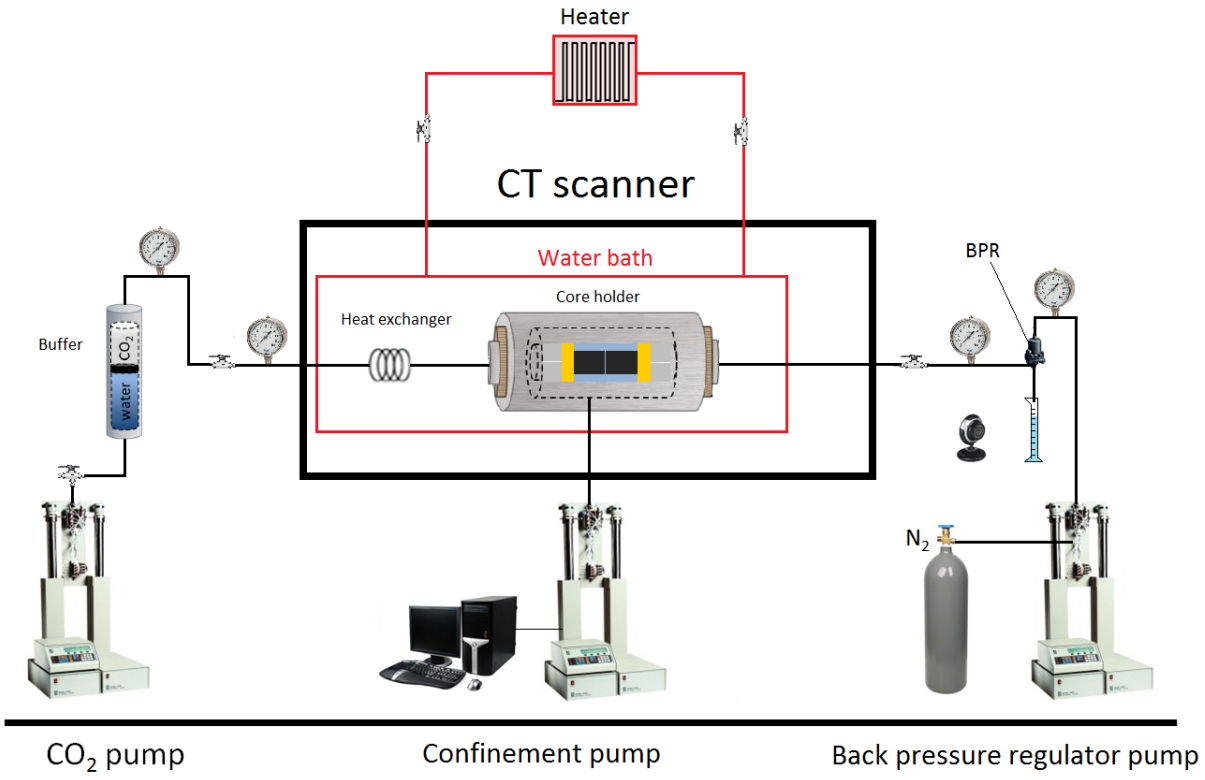

Figure 5.13: Experimental setup at Texas A&M University

Equipment used:

- Medical PET/CT scanner
- 2x computers for logging and operating pumps
- Aluminum core holder emerged in a water bath
- Shrink sleeve & glass beads
- *Swagelock* tubings,fittings and valves
- *Teledyne Isco High Pressure* pump for confinement pressure
- *Teledyne Isco High Pressure* pump for injection of CO_2 via a buffer
- *Teledyne Isco High Pressure* pump controlling back pressure with nitrogen
- Water heater including pump
- 2x unidentified reservoir shale cores

5.8.1 Procedure

The shale cores had a diameter of 1 inch (2.54 cm) whilst the core holder available was designed for 2 inch cores (5.08 cm). **Figure 5.14** shows an illustration of the how the cores were assembled to solve this problem. The two shale cores were placed on top of each other surrounded by a 2 inch shrink sleeve filled with glass beads and encapsulated between two short sandstones. This solution provides a high permeability medium with a large contact area between the CO_2 and shale core surface to allow oil recovery by molecular diffusion.

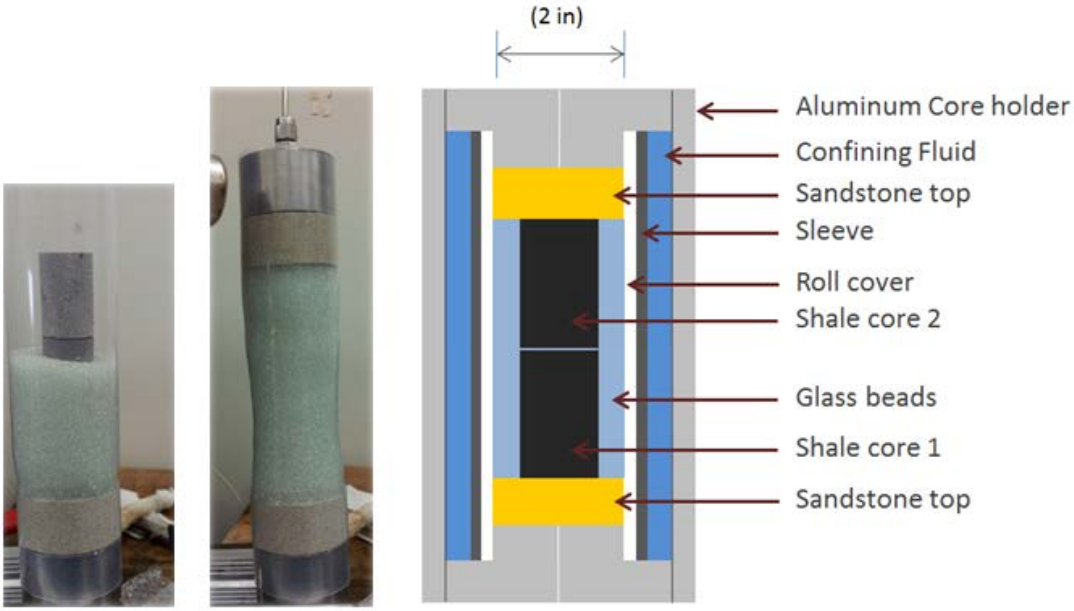

Figure 5.14: Reservoir shale cores equipped with shrink sleeve. Modified from (Tovar, 2013).

Figure 5.13 illustrates the experimental setup. The core holder was placed horizontally in the CT scanner inside a water bath holding a temperature of 65 °C. A water heater was connected to the bath circulating the water to ensure a constant temperature throughout the experiment. The back pressure regulator, controlled with nitrogen, was set to hold 200 bar. At these conditions CO_2 is in supercritical state and miscibility with the crude oil was assumed. The confinement pressure was kept 15 bar above the line pressure at all times to avoid leaks into the confinement chamber.

The rate of CO_2 diffusion into the shale was assumed to be very slow because of the low permeability. In order to save the amount of CO_2 used, the line pressure was kept at a constant pressure just below the back pressure regulator during the day and an injection rate of 3.7 ml/h during nights. The experiment was run for 5 days and during this time a total of 10 scans were taken.

6 Results and discussion

In this chapter the experimental results are presented. Basic core data from the routine analysis are presented first followed by presentation of the individual experimental results in subsections.

6.1 Routine core analysis

Basic core properties were measured experimentally as described in section 5.3. An overview over all core data is given in **Table 6.1**.

Table 6.1: Core data

Core ID	Material	Length [cm]	Diameter [cm]	Porosity [%]	PV [ml]	Siw [%]	Permeability [mD]
CHR_CO2D_2	Chalk	8.69	3.78	41.78	37.30	0	3-4*
CHR_CO2D_5	Chalk	8.62	3.82	44.03	39.93	0	3-4*
CHR_CO2D_8	Chalk	8.69	3.83	44.99	43.04	21.9	3.75
CHR_CO2D_9	Chalk	8.55	3.80	45*	45.40	0.0	3-4*
CHR_CO2F_10	Chalk	8.73	3.84	45*	45.60	0.0	3-4*
CHR_CO2D_11	Chalk	8.68	3.79	42.93	40.20	11.3	2.66
CHR_CO2D_12	Chalk	8.63	3.83	44.85	42.71	21.7	3.13
CHR_CO2D_13	Chalk	8.26	3.80	45.72	40.91	21.9	3.27
CHR_CO2D_14	Chalk	8.40	3.80	46.07	43.93	0	2.86
SHALE_1	Shale	3.97	2.53	-	-	-	-
SHALE_2	Shale	3.48	2.53	-	-	-	-
BH_#2	Sandstone	13.25	5.20	0.23	63.39	100	1296
BH_#4	Sandstone	15.19	5.16	-	-	0	1100*
CHR_#1	Chalk	8.01	5.07	44.95	72.69	0	2.82
CHR_#2	Chalk	8.59	5.09	46.73	81.64	0	3.03
CHR_#3	Chalk	8.00	5.07	46.24	74.60	34.1	2.91
CHR_#4	Chalk	7.79	4.95	47.34	70.85	0	3.51
CHR_#5	Chalk	7.63	4.95	46.16	67.72	13.6	2.89
CHR_#6	Chalk	8.07	5.08	46.67	76.39	0	3.01
CHR_#7	Chalk	8.07	5.08	47.15	77.05	30.0	3.10
CHR_#8	Chalk	7.67	4.98	46.24	68.97	21.7	3.09
CHR_#9	Chalk	8.09	5.09	46.75	76.88	0	3.17
CHR_#10	Chalk	7.28	4.95	46.26	64.78	13.6	2.89
CHR_#11	Chalk	7.50	4.94	47.09	67.75	22.1	3.23
CHR_#12	Chalk	8.09	5.08	47.70	78.26	28.3	3.11
CHR_#13	Chalk	8.08	5.08	47.31	77.53	33.6	3.15
CHR_#14	Chalk	8.23	5.08	46.96	78.28	0	3.23
CHR_#15	Chalk	7.62	5.08	46.43	71.81	0	3.01
CHR_#16	Chalk	8.11	5.08	46.82	76.86	0	3.11
CHR_#17	Chalk	8.84	3.80	45.96	46.01	17.0	4.23
CHR_#18	Chalk	8.58	3.80	46.44	45.21	15.9	4.52

*The permeability of these cores was not measured experimentally. Instead it assumed to be the in the same range as other core plugs taken from the same outcrop.

Fracture permeability

Most of the cores were fractured. High flow conductivity through the spacer leads to a low differential pressure buildup across the core. Fracture permeability was only measured on one of the cores and was calculated to be 5D ± 3D under the assumption of a consistent fluid flow through the spacer. The large uncertainty is caused by the small range in differential pressure, limited by the accuracy of the pressure transducers that were used. High permeability in the fracture, together with a low injection rate, isolates the oil recovery to CO_2 diffusion alone.

6.2 Supercritical CO_2 injection by material balance

The experiments were designed to investigate oil recovery by supercritical CO_2 injection and made analogue to the injection test conducted in the CT scanner in Bartlesville to be able to compare the results. Some of the cores were initially 100% oil saturated and some were drained to initial water saturation before injection of CO_2. The experimental procedure is explained in section 5.4. All experiments were conducted above the MMP between CO_2 and n-decane as shown in **Figure 3.6**. Uncertainties related to the experiments are discussed in section 6.8.

6.2.1 Supercritical CO_2 injection into 100% oil saturated cores

Table 6.2 shows the experimental conditions for the 100% oil saturated cores. One of the cores was flooded whole, without the presence of a fracture, to compare recovery efficiency with the fractured cores.

Table 6.2: Experimental conditions for the 100% oil saturated cores

Core ID	Fractured	S_{iw} [%]	Average P [bar]	Average T [^oC]	CO_2 injection rate [ml/h]
CHR_CO2D_2	Yes	0	89.7	35.0	3
CHR_CO2D_5	Yes	0	89.9	35.0	3
CHR_CO2D_14	No	0	90.0	35.0	3

Figure 6.1 shows the reduction in oil saturation of the 100% oil saturated cores versus pore volume of CO_2 injected. The reduction in oil saturation for the two fractured cores (CHR_CO2D_2 and CHR_CO2D_5) overlap after approximately 1.2 PV of CO_2 injected and show good reproducibility between identical cores. Before this point, a discrepancy in oil production rate can be recognized from the two graphs, predicted to be caused by small fluctuations in nitrogen pressure controlling the oil production through the BPR. The end point saturation was reached after 9 PV of supercritical CO_2 injected. Large amounts of CO_2 were injected since diffusion was the only recovery mechanism. Reduction in oil saturation for the whole core (CHR_CO2D_14) was more efficient than the fractured cores. It achieved end point saturation after 4 PV of CO_2 injected. The recovery from this core was mainly governed by viscous displacement, partly stabilized by diffusion at the contact area between the gas and oil until breakthrough of CO_2. After breakthrough the gas will follow the same flows paths and the displacement enters a diffusive regime. Early breakthrough is most likely caused by the unfavorable mobility ratio that promotes development of fingers of the CO_2. In this case a lower injection rate would increase mixing by diffusion at the contact area between the fluids, resulting in a more stable displacement front before breakthrough and thereby reducing the amount of CO_2 injected.

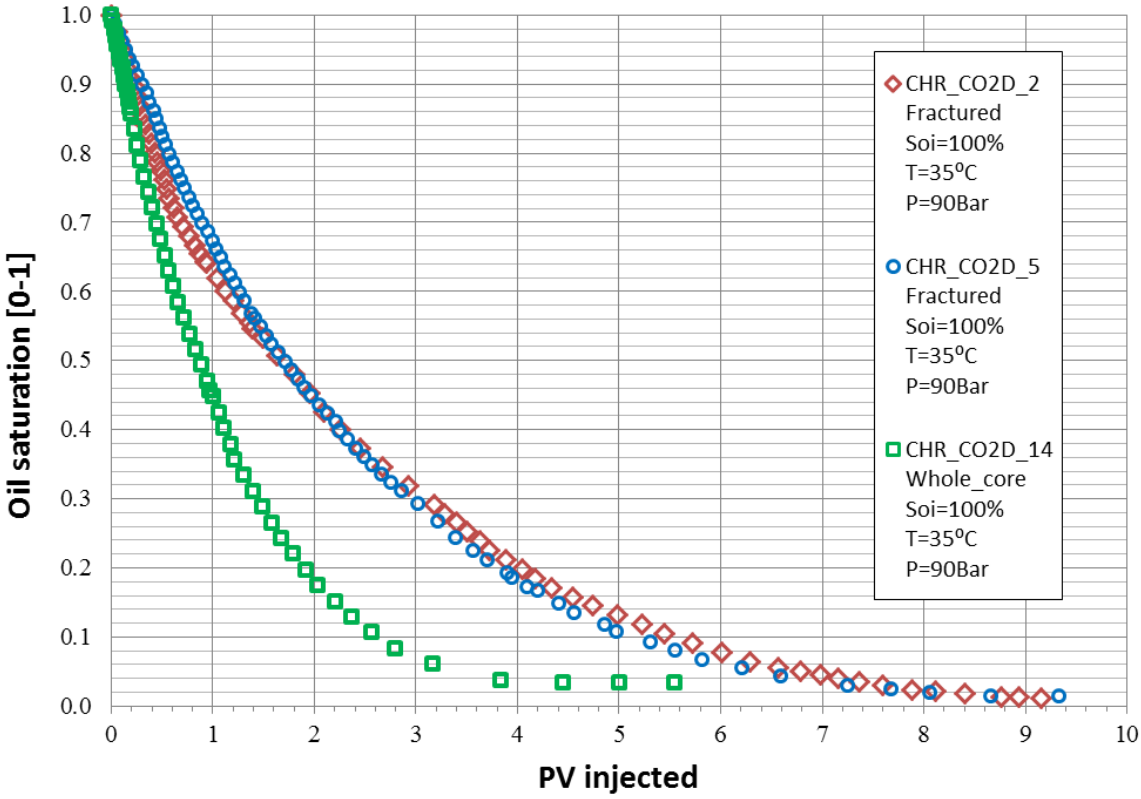

Figure 6.1: Reduction in oil saturation as a function of pore volumes of CO_2 injected for the 100% oil saturated core experiments. Two cores were fractured and one was whole core to compare results. Oil displacement in the whole core will be dominated by viscous forces until breakthrough of CO_2 at the outlet. After breakthrough the recovery mechanism will be dominated by diffusion since the gas will follow the high permeability channels to production. As for the fractured cores, after the oil initially present in the fracture is displaced, the only oil recovery mechanism is by diffusion.

The high connectivity through the fractured cores, created by the spacer, made it possible to investigate oil recovery by diffusion alone. After the oil in the fracture is displaced, it is the only mechanism that constitutes mass transfer of oil from the matrix to the fracture. If this is correct the production should be linear to square root of time, as explained in section 2.2.1.

Figure 6.2 shows oil production as a function of square root of time for the two 100% oil saturated fractured chalk cores. Before R_f = 10% the initial oil present in the fracture is displaced dominated by viscous forces. After the oil in the fracture was displaced, CO_2 will be the only fluid flowing through the fracture at a low rate. The only way to recover oil from the matrix will then be by diffusion from the fracture. After approximately R_f = 10% the production graphs become close to linear with square root of time. The linear production indicates a diffusion regime from approximately R_f = 10% to R_f = 80% PV injected where diffusion is the only recovery mechanism. In this time period the bulk flow velocity within the pores is too slow for convection and the mixing between CO_2 and n-decane is completely controlled by diffusion (Perkins, 1963). Above R_f = 80% most of the oil is already displaced and the production declines. Diffusion is driven by concentration gradients and the low concentration of remaining oil near the boundary of the core contributes to a lower recovery rate after 7 PV of CO_2 injected. The recovery rate is slower because the small fraction of oil left is near the outer edge of the core and must be transported a longer distance through a tortuous pore network before it reaches the fracture and is produced.

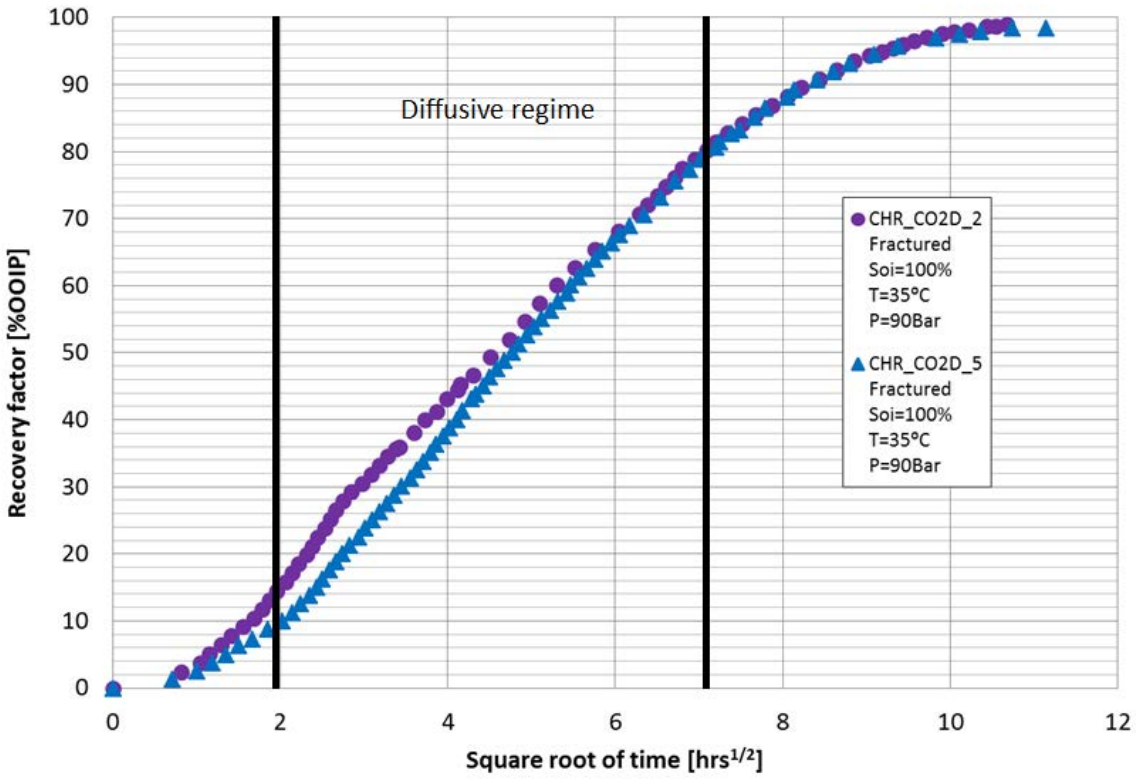

Figure 6.2: Oil recovery as a function of square root of time for both 100% oil saturated core experiments. A linear production is observed from approximately Rf = 10% to Rf = 80% and highlights a diffusive regime (indicated in the figure).

6.2.2 Supercritical CO_2 injection into oil saturated cores with initial water saturation

Table 6.3 lists the experimental conditions for the oil saturated cores with initial water saturation present. To examine the effect of different water saturations present one of the cores (CHR_CO2D_11) was drained for more than 10 hours, producing a lower initial water saturation.

Table 6.3: Experimental conditions for the cores with initial water saturation

Core ID	Fractured	S_{iw} [%]	Average P [bar]	Average T [°C]	CO_2 injection rate [ml/h]
CHR_CO2D_08	Yes	21.9	90.3	35.0	3
CHR_CO2D_11	Yes	11.3	90.0	35.0	3
CHR_CO2D_12	Yes	21.7	90.0	35.0	3

Figure 6.3 shows the reduction in oil saturation as a function of CO_2 injected into oil saturated cores with initial water saturation present. Two of the experiments were aborted because of spotted leaks from the system. The leaks explain the slower recovery from these graphs compared to the completed experiment (CHR_CO2D_8). A total of 10 PV of CO_2 injected was required to achieve end point saturation at 96% of OOIP for CHR_CO2D_8.

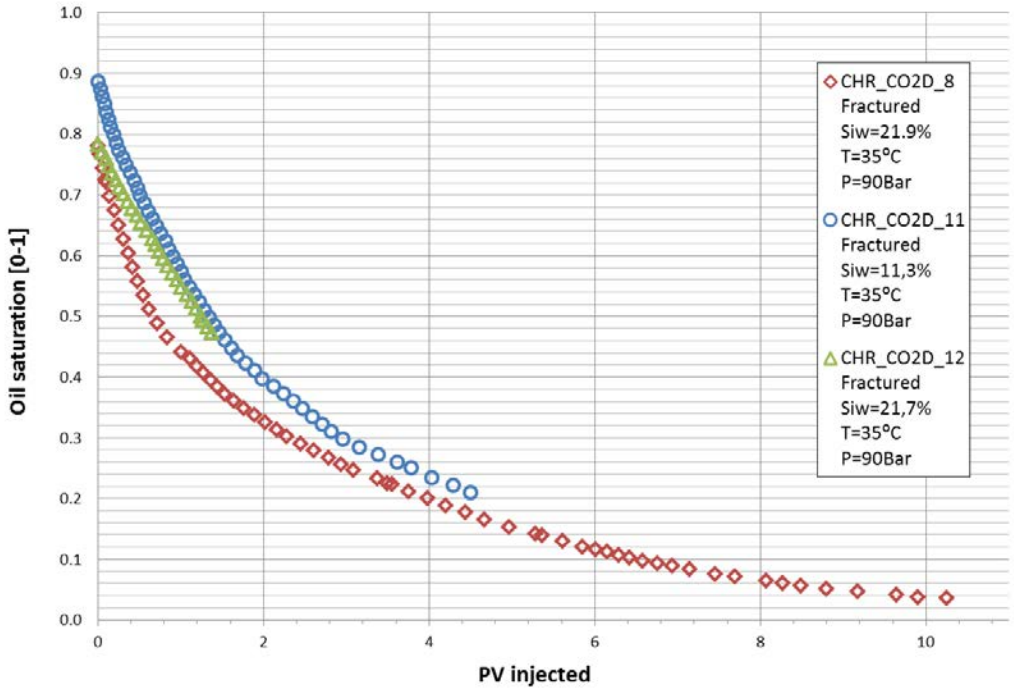

Figure 6.3: Reduction in oil saturation for the cores with an initial water saturation present. Two experiments were aborted caused by leaks from the system. The graphs match and show good reproducibility. A total of 10 PV of CO_2 injected was required to achieve end point saturation at 96% of OOIP for CHR_CO2D_8.

Figure 6.4 shows the oil recovery as a function of PV CO_2 injected for all experiments conducted at UoB. The 100% oil saturated whole core is the most efficient resulting from a viscous- and diffusive dominated displacement. Displacement in fractured cores depends on diffusional processes alone and results in a slower recovery. Cores with initial water had slower recovery and more CO_2 was needed to achieve the same total recovery. Still, a total recovery of over 95% of OOIP was obtained for all cores and emphasizes the potential with the use of CO_2 and the effects of molecular diffusion as an important recovery mechanism.

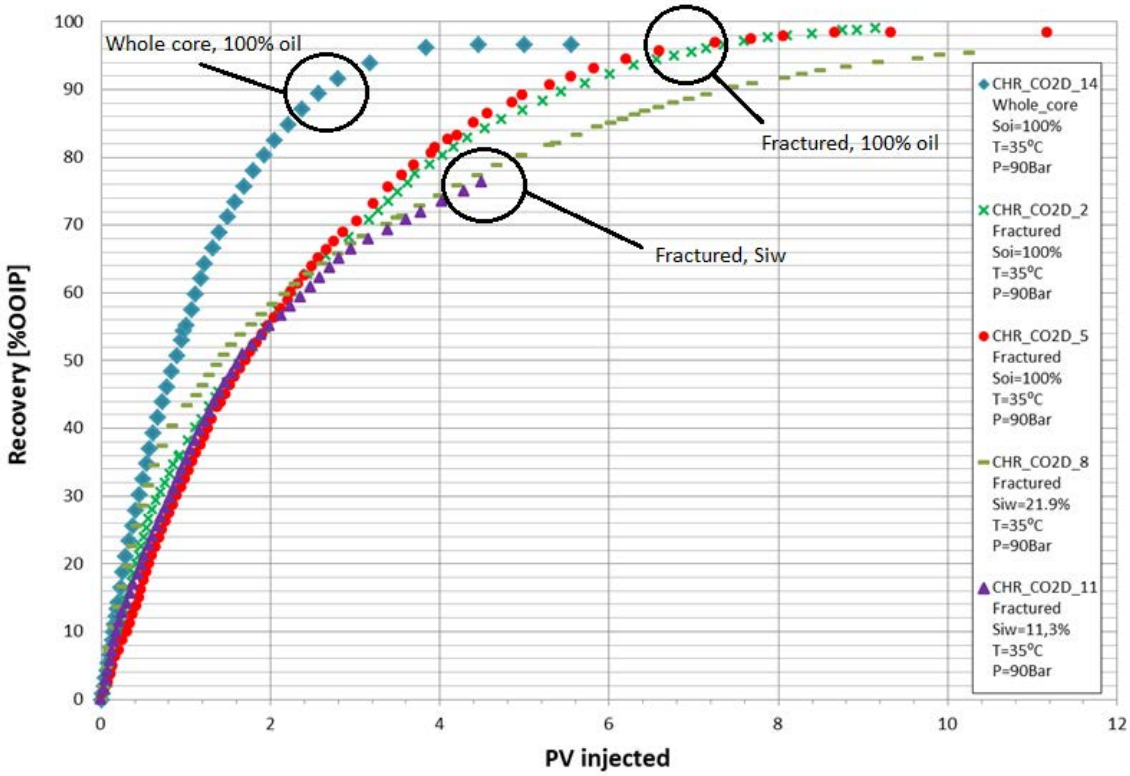

Figure 6.4: Recovery profile of all experiments conducted at University of Bergen. The graphs highlight the impact on oil recovery efficiency with the use of CO_2 in different scenarios such as the presence of fractures and initial water saturation. All the experiments achieved endpoint saturations above 95% OOIP.

The presence of water decreases the contact area between oil and gas and thereby reduces diffusional fluxes and consequently the amount of oil recovered by diffusion (Grogan, 1987). Water reduces the amount of CO_2 available for mixing with the oil because of CO_2 solubility in water (Pollack et al., 1988). Up to 10% of the injected CO_2 can dissolve in water and are thereby made unavailable for mixing with the oil (Chang et al., 1998). The mentioned effects will delay oil recovery for cores with initial water present and can be recognized from **Figure 6.4**.

All experiments included injecting at least over 4 PV of CO_2 into the core. Injecting this much CO_2 into an oil reservoir would not be economical but it points out the large potential with the use of miscible CO_2 injection for EOR. More experiments are needed to draw definite conclusions on this matter.

6.3 Supercritical CO_2 injection visualized in CT

Two supercritical CO_2 injections were performed at ConocoPhillips Research Center in Bartlesville, Oklahoma. The process behind CT scanning is briefly explained in section 4.1. Experimental procedure is explained in section 5.5 and the experimental conditions for the two experiments are given in **Table 6.4**. Uncertainties related to CT scanning are discussed in section 6.8.

Most of the work and analysis was conducted on the CO_2-injection (CHR_CO2D_9), the CO_2-foam injection (CHR_CO2F_10) is presented in an individual section (section 6.4). In this section the only focus will be on the CO_2 injection although experimental conditions for both experiments are presented in **Table 6.4**.

Table 6.4: Experimental conditions

Core ID	Fractured	S_{iw} [%]	Average P [bar]	Average T [^oC]	CO_2 injection rate [ml/h]
CHR_CO2D_9	Yes	0	107	42	2*
CHR_CO2F_10	Yes	0	109	42	2*

Large fluctuations in room temperature during the experiment made it difficult to estimate the injection rate at experimental conditions. A constant CO_2 injection rate of 1.8 ml/h was kept during the whole experiment at ambient temperature (from 10 °C to 25 °C) and experimental pressure (107 and 109 bar). Assuming a constant ambient temperature of 20 °C, the CO_2 injection rate was calculated to be 2.7 ml/h at experimental conditions. The impact of the temperature fluctuations for the supercritical CO_2-injection will be discussed in section 6.3.7.

6.3.1 Dry scan

Figure 6.5 shows the dry scan of the core (CHR_CO2D_9) used in the supercritical CO_2-injection experiment. The image shows density differences within the core. Warm colors indicate high density areas and low density areas were made transparent. Only a specified interval of higher density areas was highlighted to the show the possibility of discovering geological activity and heterogeneities within the core samples with the use of CT. Less dense rock material was made transparent.

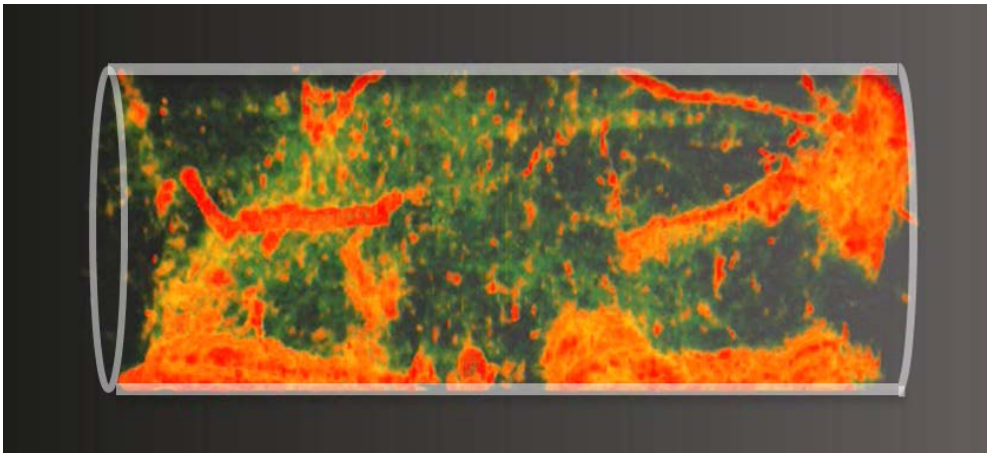

Figure 6.5: Dry CT scan of core CHR_CO2D_9. The 3D images are showing density differences within the cores. Warm colors indicate high density areas and low density areas are transparent. Note that only a specific interval of high density areas shows with colors. The transparent areas are filled with less dense rock material.

The high density areas from **Figure 6.5** were interpreted to be geological records of biological activity (mainly burrows). These areas are less permeable and may influence fluid flow within the core. No signs of deformation bands were observed.

6.3.2 CO_2 injection

Supercritical CO_2 was injected into a fractured 1.5" chalk core (CHR_CO2D_9) at a calculated rate of 2.7 ml/h for 5 days. A total of 30 scans were conducted during the experiment, each consisting of 184 image slices. The voxel dimension was 0.156 mm * 0.156 mm * 0.5 mm.

Figure 6.6 illustrates the horizontal core alignment with a vertical fracture plane. The alignment of the fracture made it possible to study both the recovery mechanism by diffusion, in addition to the influence of gravity effects inside the fracture. Colors are adjusted to see the vertically aligned spacer in the fracture. The plane indicated in the **Figure 6.6** illustrates where the core was digitally sliced to visualize fluid flow between matrix and fracture.

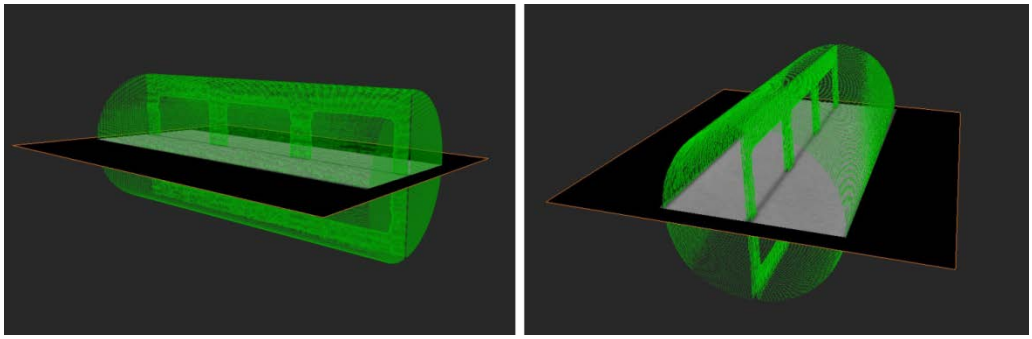

Figure 6.6: Illustration of core alignment with embedded plane to indicate where the core was digitally sliced horizontally to visualize the spatial fluid saturations during the injection test. The vertical fracture is generated by the spacer and can be seen in the figure.

Figure 6.7 shows the calculated porosity distribution of core CHR_CO2D_9. The porosity was calculated by equation 4.2 and an average porosity varying between 45-46 % can be recognized from the graph. This value corresponds with the measured porosity from similar 1.5" Rørdal chalk cores presented in **Table 6.1**.

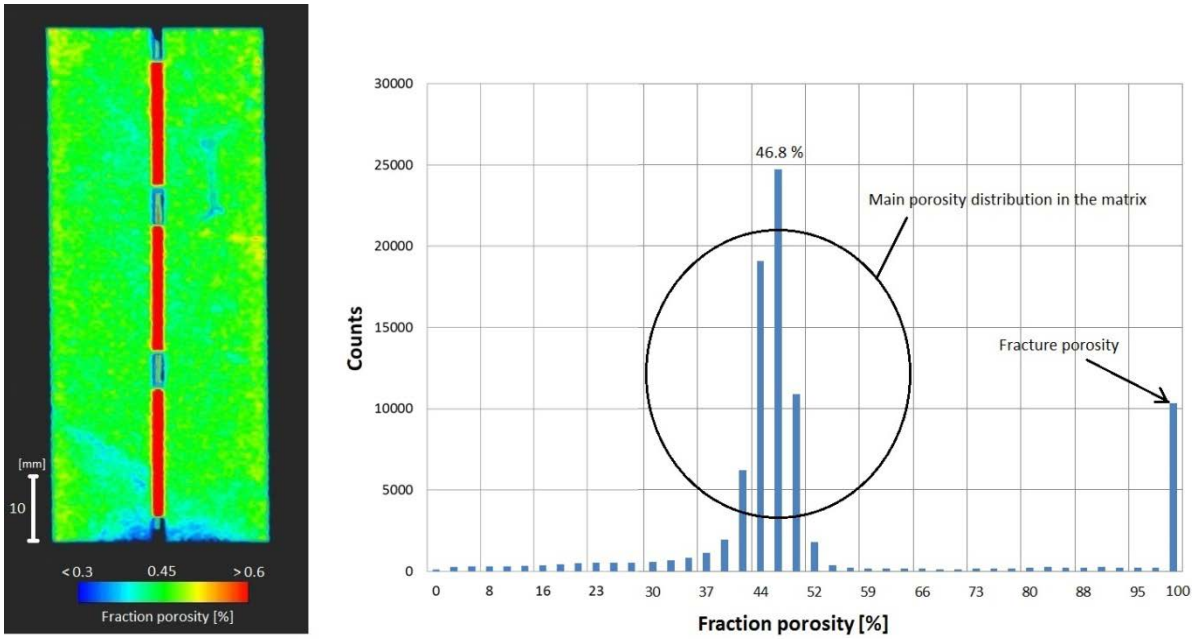

Figure 6.7: Calculated fractional voxel porosity from obtained CT-values of core CHR_CO2D_9. On the left is a porosity image, horizontally perpendicular to fracture plane. The green color indicate a porosity of ~45%, and the red color indicate a porosity >60%. Calculated voxel porosity is presented in a histogram on the right.

Figure 6.8 shows the oil development from calculated saturations obtained from CT-values from all 30 scans. Fluid saturations were calculated as explained in section 4.1.1. The core was digitally sliced perpendicular to the fracture plane as indicated in **Figure 6.6**. Each image represents the same location of the core at different time steps from a birds-eye view, where CO_2 is injected at the bottom of the image and produced at the top. The time is indicated at the bottom of each image. Warm colors indicate high oil saturations and cold colors indicate low oil saturation.

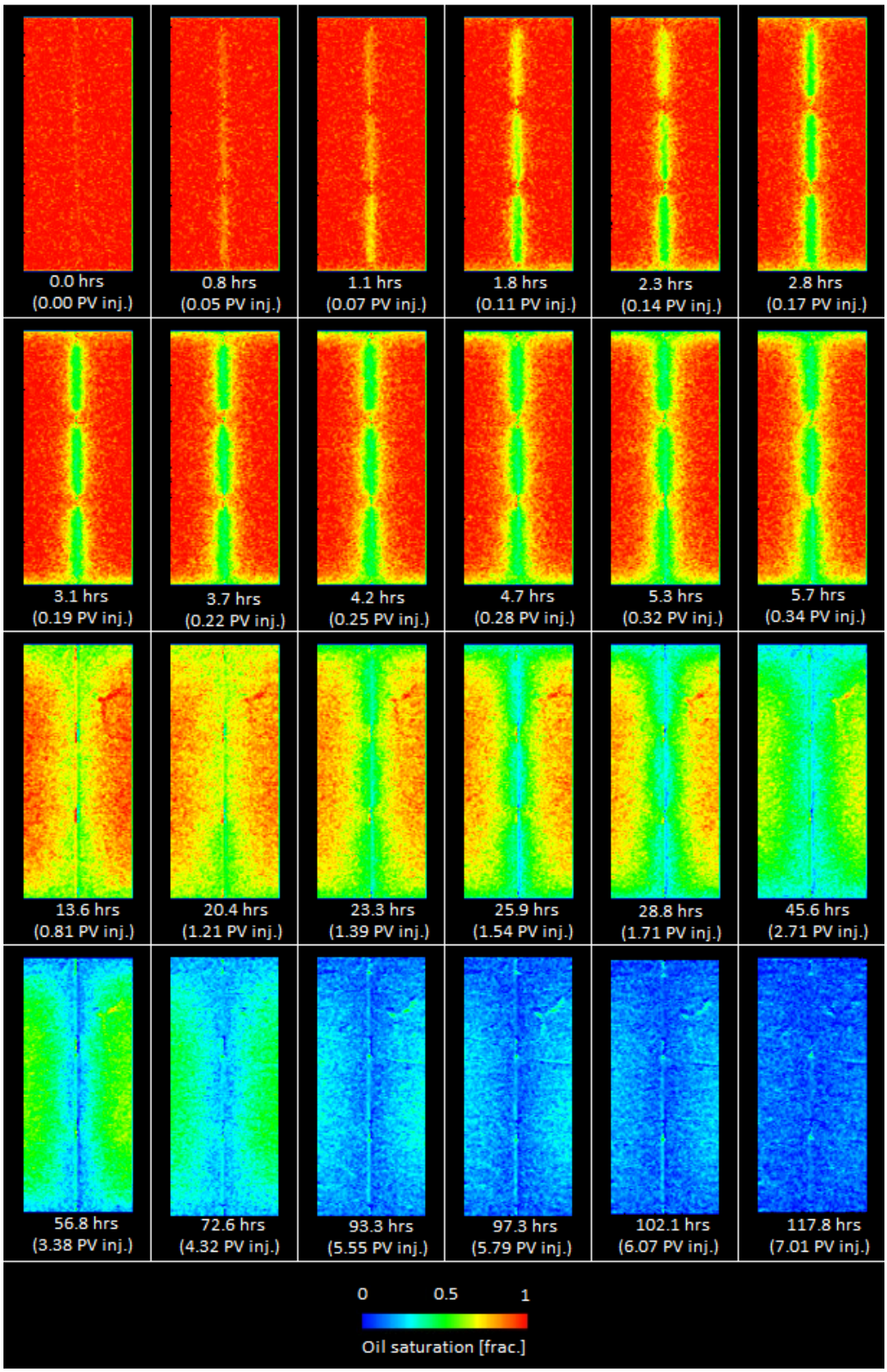

Figure 6.8: Calculated oil development based on CT-values obtained from the scans for the supercritical CO_2 experiment (CHR_CO2D_9). Warm colors indicate high oil saturations and cold colors indicate low oil saturation. The core is horizontally digitally sliced perpendicular to the fracture to observe recovery mechanisms from a birds-eye view.

It can be observed from **Figure 6.8** that the CO_2 flowed through and displaced oil from the fracture first. There were no signs of a front from the inlet side where the CO_2 was injected. High fracture conductivity directs the flow of CO_2 through the fracture. A symmetric reduction in oil saturation from the end pieces at the inlet side (bottom) and the outlet side and also in the matrix adjacent to the fracture is observed. This validated diffusion as the main recovery mechanism. Similar effects (diffusion from end-pieces) was also observed in a CO_2 injection experiment into fractured chalk core with the use of MRI imaging (Haugen, 2012).

Figure 6.9 shows how the core was digitally sliced vertically perpendicular to the fracture plane where the inlet- and outlet effects are minimal, to investigate the effects of gravity on the saturation distribution during displacement.

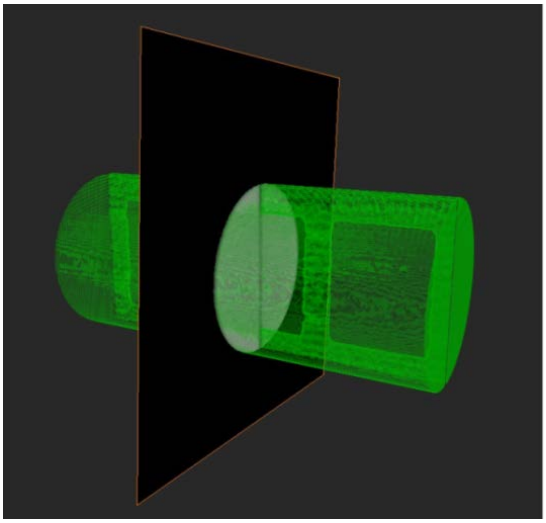

Figure 6.9: Illustration of core alignment with embedded plane to indicate where the core was digitally sliced vertically to visualize the displacement, saturation distributions and gravity effects.

Figure 6.10 shows the oil development in the middle of the core (X_L = 0.5). Warm colors indicate high oil saturations and cold colors indicate low oil saturation. The CO_2 enter the lower parts of the fracture upon entering the core. The CO_2 saturation, given by cold colors, gradually increased in the top of the core throughout the injection test.

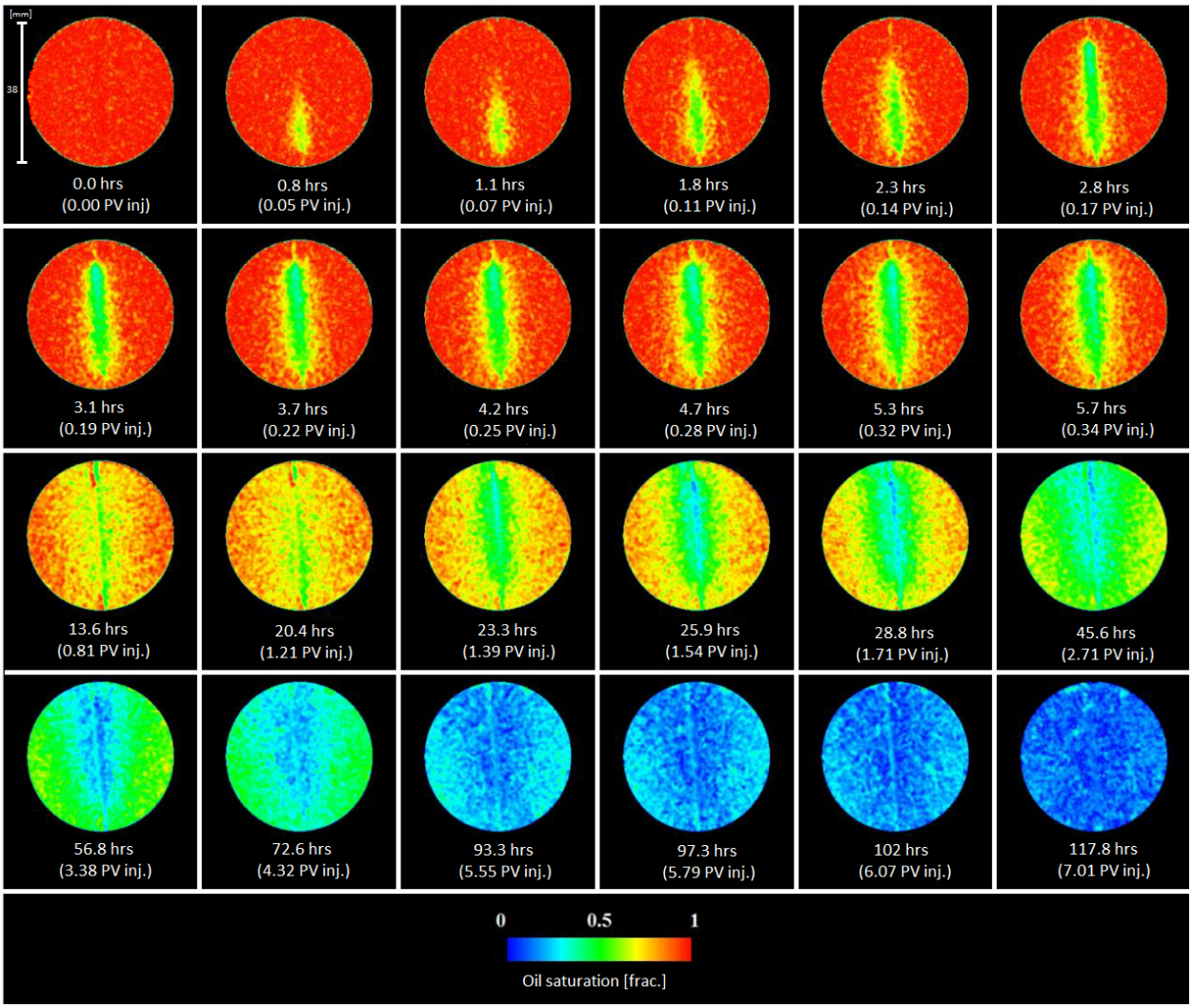

Figure 6.10: Calculated oil development in a vertical slice in the center of the core at different time steps. Warm colors indicate high oil saturations and cold colors indicate low oil saturation. The CO_2 saturation, given by cold colors, was high in bottom of the fracture at the beginning of the test before it gradually increased in the top throughout the injection test. A length scale is indicated on the left on the first image (38 mm).

6.3.3 Calculation of CO_2 concentrations

The CT images were used to identify the different phases and to quantify spatial fluid saturations during CO_2 floods. An oil solvable dopant was used to increase the density of the oil phase to improve accuracy in phase saturation determination.

Figure 6.11 illustrates where the CT values was obtained for saturation calculations, from a line probe penetrating the center of the core (X_L = 0.5), in each of the total 30 scans. The line probe was placed through the center of the open fracture created by the spacer, perpendicular to the fracture plane. This location was chosen to give the most representative CT values for determination of the diffusion process.

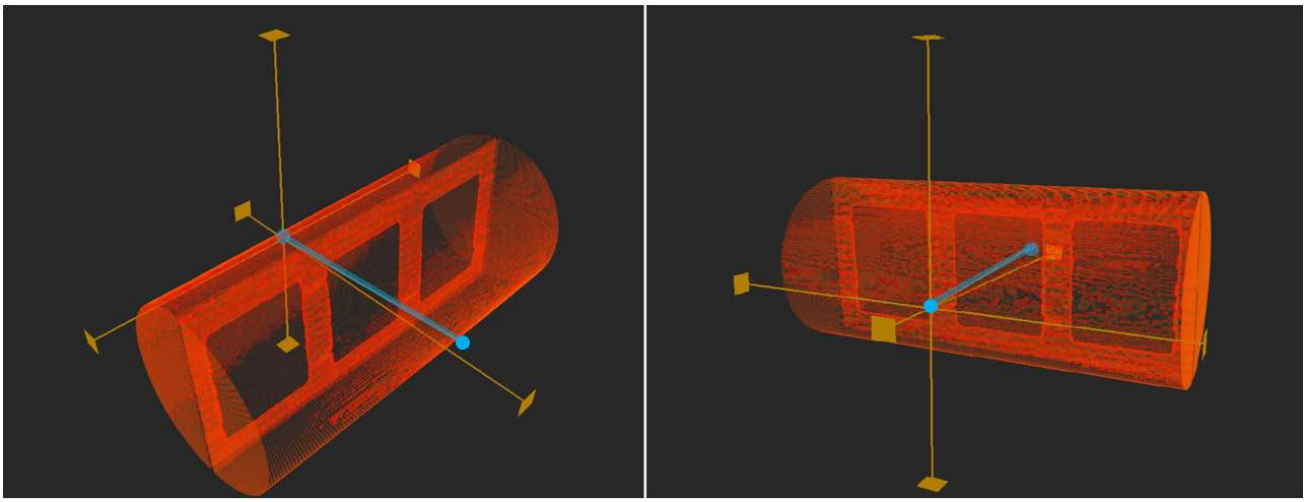

Figure 6.11: Lineprobe location for saturation calculations. It was placed through the center of the middle fracture created by the spacer, perpendicular to the fracture plane. The blue line between the two blue dots indicates the location of the obtained CT-values.

Figure 6.12 shows the development in CT values at the location set by the line probe. The upper line called OIL_SAT represent the 100% oil saturated scan at the start of the experiment. The bottom line called CO2_SAT represent the CT-values obtained from the 100% CO_2 saturated scan. All the lines between these two illustrate a reduction in CT values as CO_2 displaced oil during displacement as a function of time and distance from fracture. The fracture can be observed by drop in the CT values in the middle of the lines. The boundaries of the core can be observed by a rapid drop in CT values at the left and right.

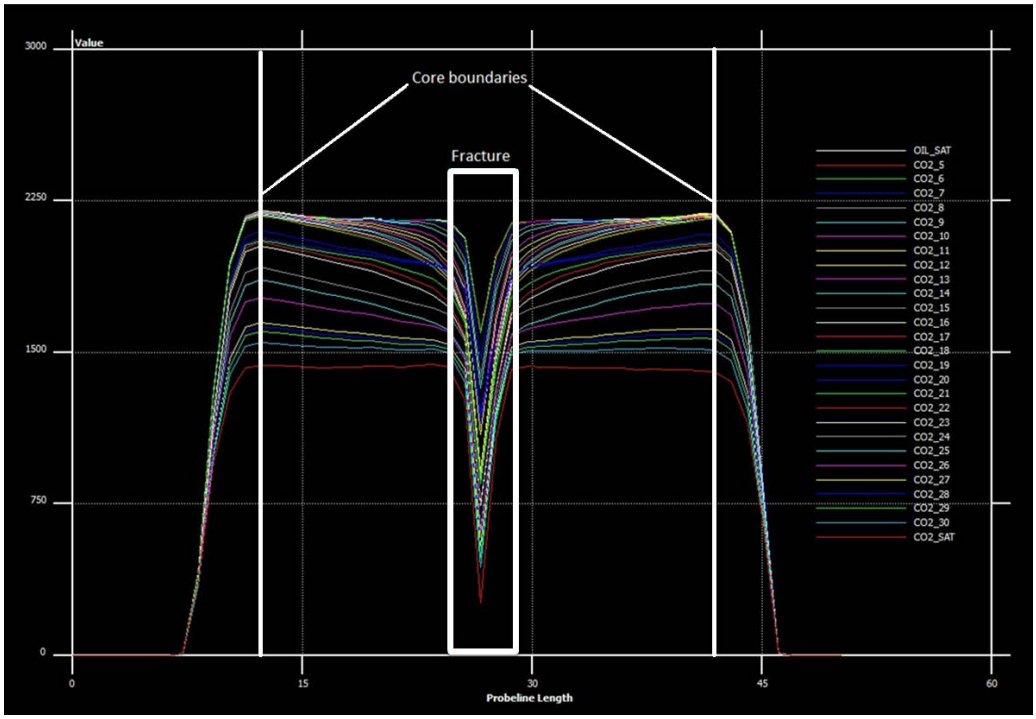

Figure 6.12: CT values obtained from the line probe. The upper line (white color) represent 100% oil saturated core, and the bottom line (red color) represent a 100% CO_2 saturated core. As oil is displaced by CO_2, the lines gradually decline from 100% oil saturation down towards 100% CO_2 saturation. The lines represent the development in fluid distribution at the location of the line probe at different distances from fracture and at different time steps. CT values are lower in the fracture because of the absence of a porous media were only fluids are present.

Figure 6.13 shows the calculated CO_2 concentration as a function of distance from the fracture at different time steps, assuming a linear relationship between CT values and the saturation. The fracture is located at 0 mm and the boundary of the core is located at 16 mm. As oil is displaced from the matrix, CO_2 concentration increases throughout the injection test. In the beginning of the test, a high CO_2 concentration gradient from the fracture can be identified from the lines, but levels off evenly from fracture to the boundary of the core as time commences.

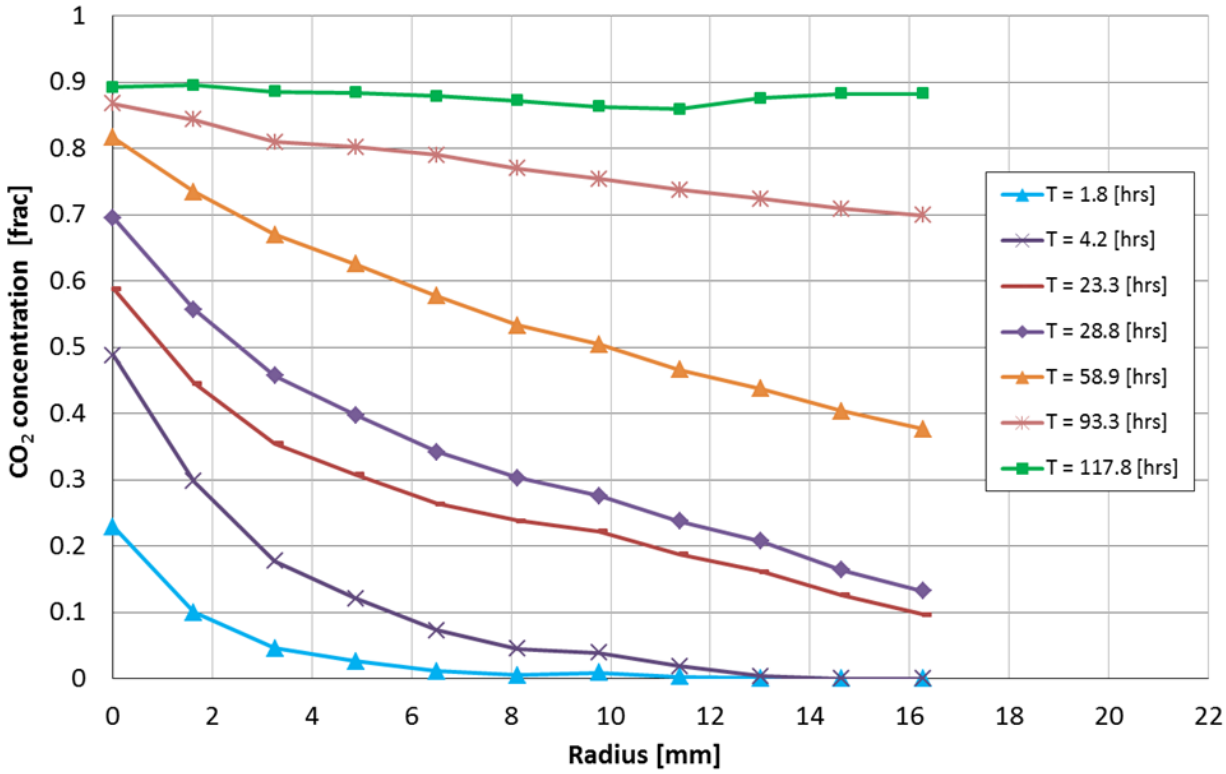

Figure 6.13: Calculated CO_2 concentration as a function of distance from the fracture (radius) at different time steps. Distance goes from 0 mm (fracture) to 16 mm (boundary of the core). As the oil is displaced, CO_2 concentration increased in the matrix throughout the injection test. In the beginning of the test, a high CO_2 concentration near the fracture can be identified from the lines. As time commences the CO_2 concentration levels off evenly from the fracture to the boundary of the core.

6.3.4 Calculation of diffusion coefficient

CO_2 diffusion into the oil leads to mass transfer of oil from the matrix to the fracture. The molecular diffusion coefficient defines the rate of the diffusion process. This process is important in miscible CO_2 flooding as it is one of the main recovery mechanisms in fractured reservoirs. Two methods of finding the diffusion coefficient were applied in this thesis. The first method was found in the literate and involves graphical estimations from Fick's second law based on the spatial CO_2 distribution throughout the core. The second method was to estimate the diffusion coefficient by comparing numerical simulation with the experimental results by using CMG GEM simulator (presented in section 6.4).

A graphical method of estimating the diffusion coefficient is introduced by Islas *et al.* (Islas-Juarez, 2004a). It involves calculation of diffusion coefficients from experimental concentration profiles directly from Fick's second law, given by equation 2.3.

Figure 6.14 and **Figure 6.15** shows the CO_2 concentration profiles for CHR_CO2D_9 as a function of time and distance from fracture, respectively. CO_2 concentration profiles were determined based on the obtained CT values as explained in section 6.3.2. The uncertainties related to the concentration profiles are related to the uncertainty in the CT-values obtained from the CT-scanner and with the assumption that CT-values are in a linear correlation with fluid saturations.

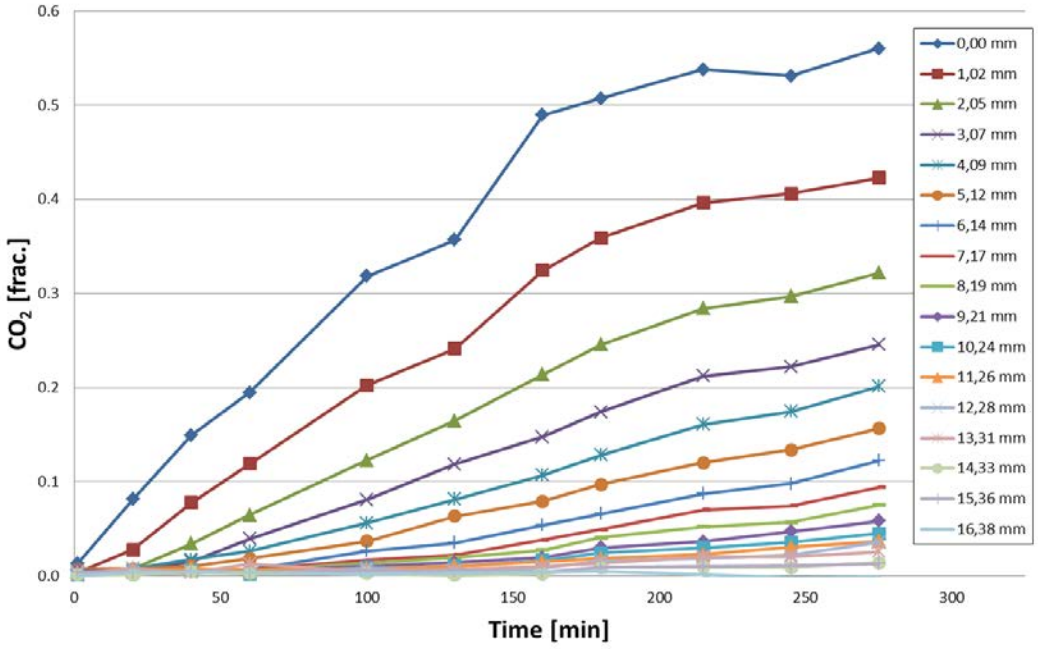

Figure 6.14: Calculated CO_2 concentration in the matrix versus time at various distances from the fracture. Each graph represents CO_2 concentration development with time at a specific distance from the fracture. Increasing CO_2 saturation at all distances in the matrix from the fracture was observed as time commenced and can be identified from the lines.

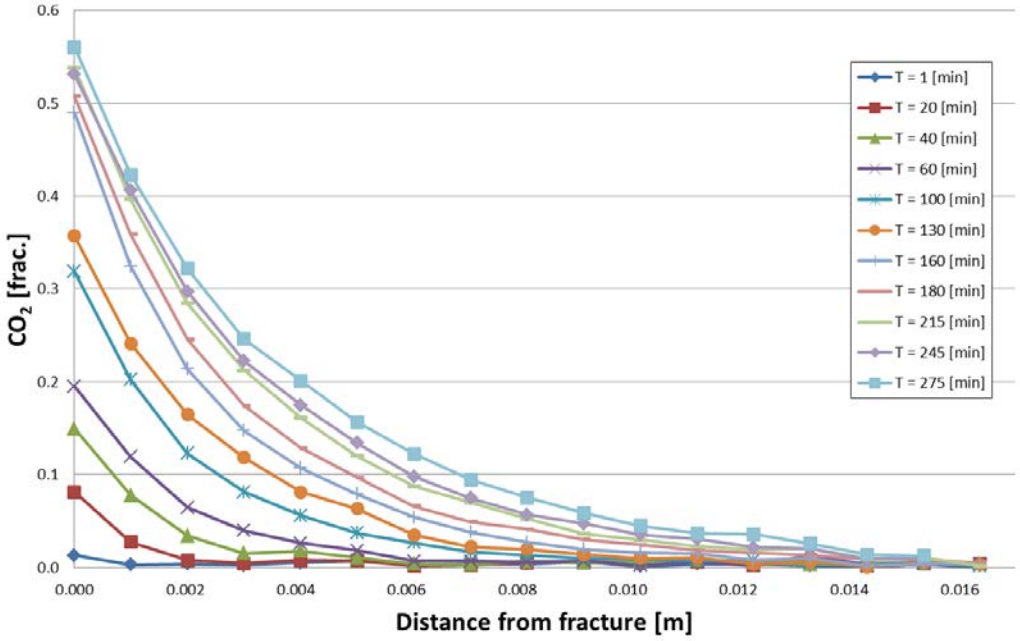

Figure 6.15: Calculated CO_2 concentration in the matrix versus distance from fracture at different time steps. Each graph represents CO_2 concentration from the fracture to the boundary of the core at one time step. Increasing CO_2 saturation in the matrix was observed in the matrix as time commenced and can be identified from the lines.

A change in matrix CO_2 saturation near the fracture was initially observed after 60 minutes. The 11 subsequent scans from time = 60 min (PV inj. = 0.05) to time = 275 min (PV inj. = 0.34) were used to determine the diffusion coefficient when the process was unaffected from boundary effects.

Trendlines were made for each individual data set (see **Figure 6.14** and **Figure 6.15**) to match the experimental results. Each of these trendlines was assigned with an equation. The equations obtained were used to determine the diffusion coefficient. The effective diffusion coefficient was found by equation 2.3, taking the first derivative of CO_2 concentration with respect to distance from fracture ($C_m = f(x)$) and the second derivative of CO_2 concentration with respect to time ($C_m = f(t)$). Since each data set has its own distinctive equation for CO_2 concentration profiles as a function of time and as a function of distance, many diffusion coefficients were calculated. A total of 112 diffusion coefficient were calculated, ranging from $8*10^{-11}$ [m^2/s] to $6*10^{-9}$ [m^2/s].

Figure 6.16 displays all the diffusion coefficients calculated from each data set as a function of distance from fracture. A tendency of increasing diffusion coefficient with increasing distance from fracture can be observed. The average diffusion coefficient based on the values obtained from all data sets from T = 60 [min] to T = 275 [min] was calculated to be D_e = 1.66*10^{-9} ± 7.2*10^{-10} m^2/s. The uncertainty is calculated based on standard deviation.

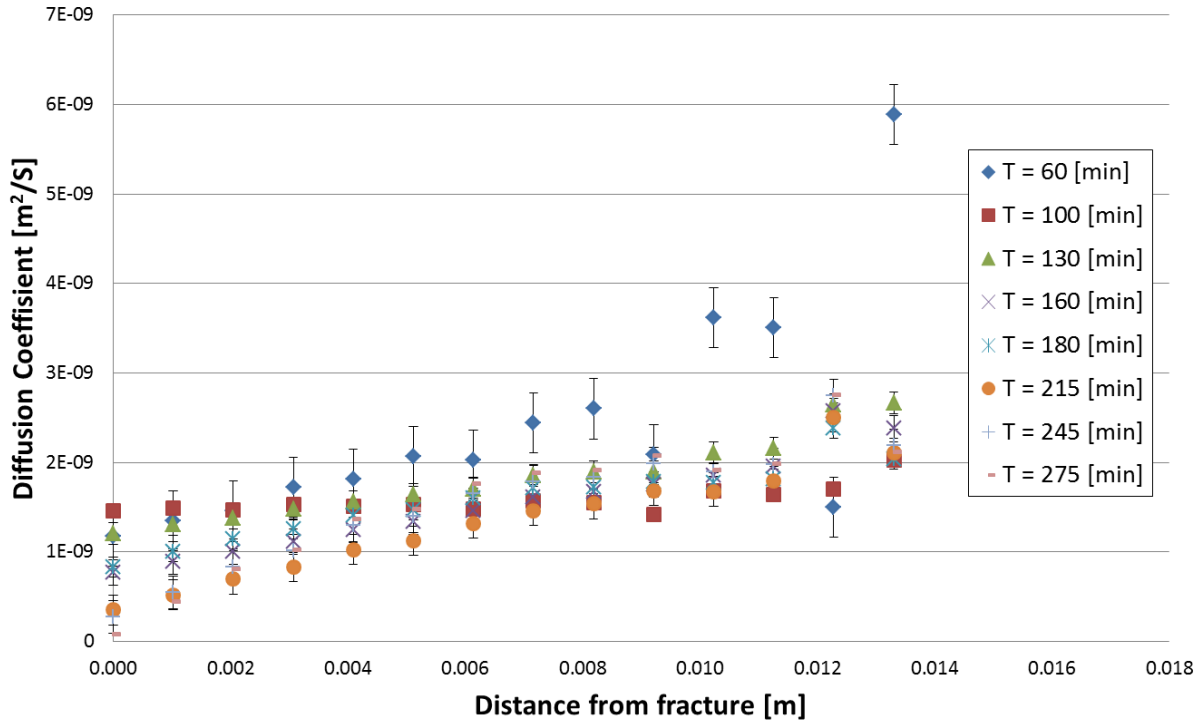

Figure 6.16: Calculated diffusion coefficient based on determined CO_2 concentration profiles from the experimental results. The coefficients are calculated by a direct use of Fick's second law of diffusion with the use of CO_2 concentration profiles as a function of time and as a function of distance. The average effective diffusion coefficient was found to be D_e = 1.66*10^{-9} ± 7.2*10^{-10} m^2/s.

The outliner point observed in **Figure 6.16** after 60 minutes (0.013 m from the fracture) represents the highest diffusion coefficient. The diffusion process is driven by concentration gradients and is faster where higher concentration difference between the two miscible fluids exists. The high concentration of oil and low concentration of CO_2 near the edge of the core causes a faster diffusion rate; hence CO_2 molecules mix faster with oil in this area. This also explains the trend of increasing diffusion coefficient with increasing distance from the fracture. Near the fracture there will be a more even distribution of CO_2- and oil molecules resulting in a slower diffusion rate.

Figure 6.17 presents literature values of diffusion coefficients between CO_2 and n-decane as a function of pressure. The diffusion coefficient found in this experiment was in the same range as the experimental values found by Renner and Grogan, performed with a porous media present (Renner, 1988) and also without a porous media present (Grogan et al., 1988). Both Renner and Grogan observed an increase in diffusion coefficient with increasing pressure. The coefficient found in this experiment is lower than the trend of increasing pressure as found by the others. The diffusion rate in porous media depends on the tortuosity factor, porosity and matrix geometry (Darvish, 2007). These parameters are different in Rørdal chalk than for Berea sandstone (see section 5.1) and will contribute to the slightly lower value at a higher pressure.

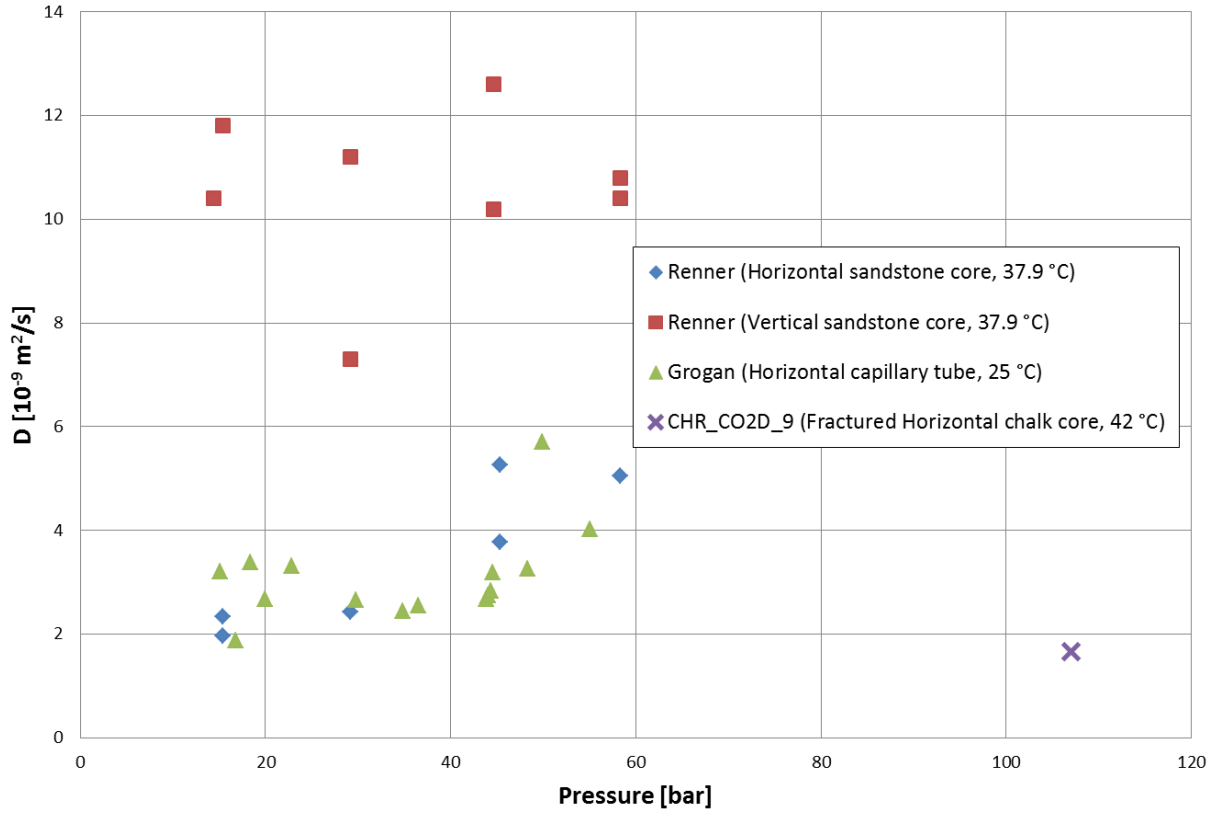

Figure 6.17: Diffusion coefficients between CO_2 and n-decane as a function of pressure. Diffusion coefficients from Renner and Grogan at different experimental conditions are indicated, in addition to the calculated diffusion coefficient from the CO_2 injection presented in this thesis. The calculated diffusion coefficient is in the same range as results from Renner and Grogan. Results from Grogan are based on average experimental pressure. Data obtained from (Renner, 1988, Grogan et al., 1988)

6.3.5 Material balance calculation

Figure 6.18 show the reduction of oil saturation as a function of pore volumes of supercritical CO_2 injected for CHR_CO2D_9. The blue dots are measured oil production from material balance and the green line presents the experimental line pressure during the experiment. The temperature in the CT-scanner room decreased during the nights causing a drop in the line pressure. The fluctuations in line pressure resulted in a periodically stop in oil production during the nights as can be observed in the graph. To be able to compare the production to other tests a series of plots was generated to represent the actual oil production without stagnations highlighted by red squares in the figure.

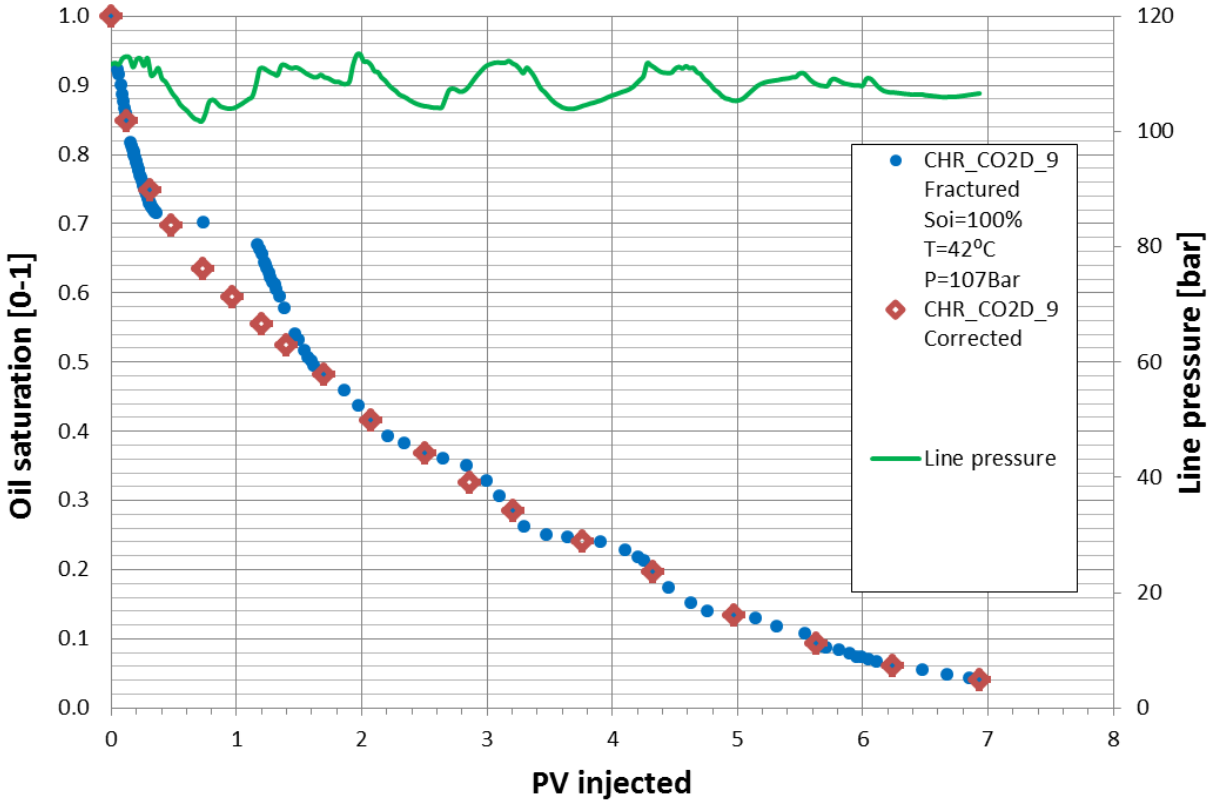

Figure 6.18: Reduction in oil saturation as a function of PV supercritical CO_2 injected in addition to the line pressure. Temperature fluctuations during the nights caused a periodic stop in production. An additional set of data (red squares) was created to correct the curve of the reduction in oil saturation, in a scenario with no fluctuations in pressure, to be able to compare the results with other tests. The line pressure was plotted in the same figure to highlight the stagnations in oil production as the line pressure dropped at nights.

Figure 6.19 shows the calculated recovery from material balance for CHR_CO2D_9 in addition to differential pressure during the experiment. Low differential pressure confirms the absence of viscous forces during the displacement and thereby confirms the only recovery mechanism to be molecular diffusion. The total recovery reached 96% OOIP after approximately 7 pore volumes of CO_2 injected.

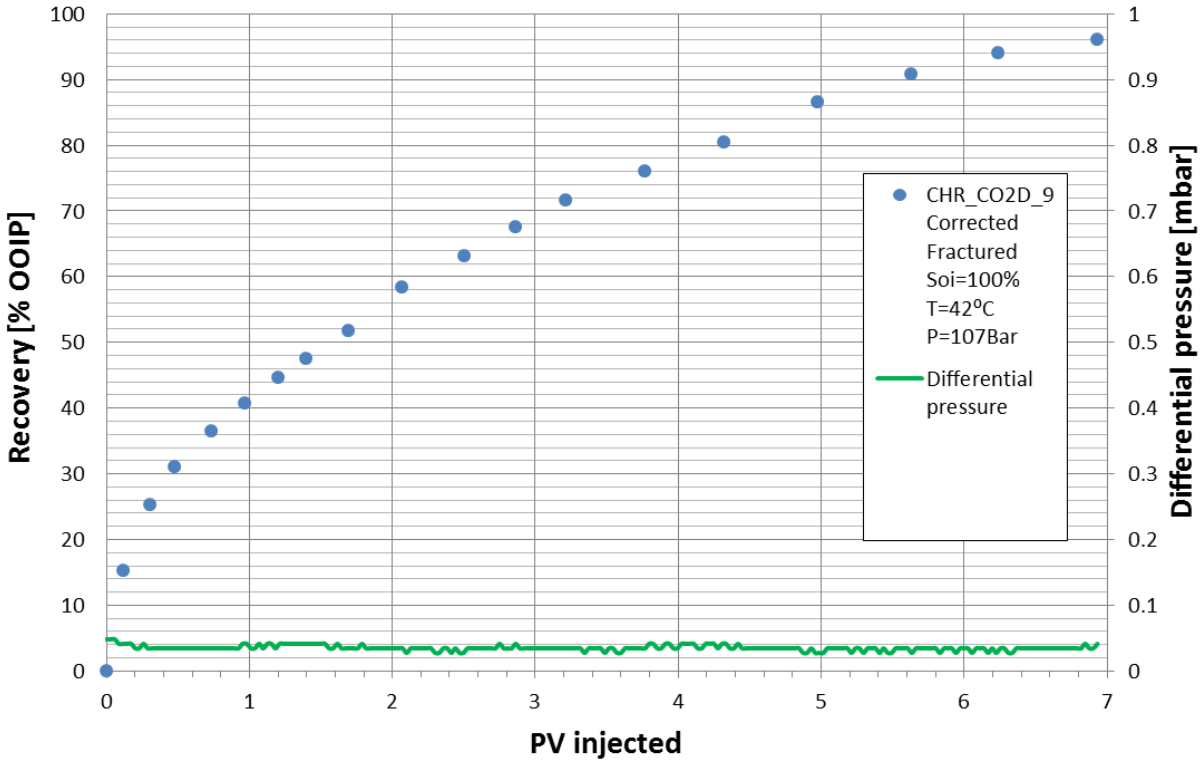

Figure 6.19: Calculated oil recovery from material balance and the differential pressure across the core during the experiment. The lack of differential pressure confirms diffusion as the only recovery mechanism. The total recovery reached 96% of OOIP when the experiment was terminated.

Figure 6.20 shows reduction in oil saturation as a function of pore volumes of CO_2 injected from the two analogue experiments conducted at UoB (P = 90 bar, T = 35 °C) in addition to the CO_2 injection conducted in the US (P = 107 bar, T = 42 °C). All three experiments involved injection of supercritical CO_2 into a fractured 1.5" Rørdal chalk core which was 100% oil saturated and reached final recoveries above 96% OOIP. The graphs overlap and show good reproducibility between identical cores. No significant discrepancy on reduction in oil saturation can be recognized. A slight variation in the oil recovery rate can be identified from the lines, caused by delayed and accelerated production resulting from pressure variations either in the system or the nitrogen pressure controlling production through the BPR.

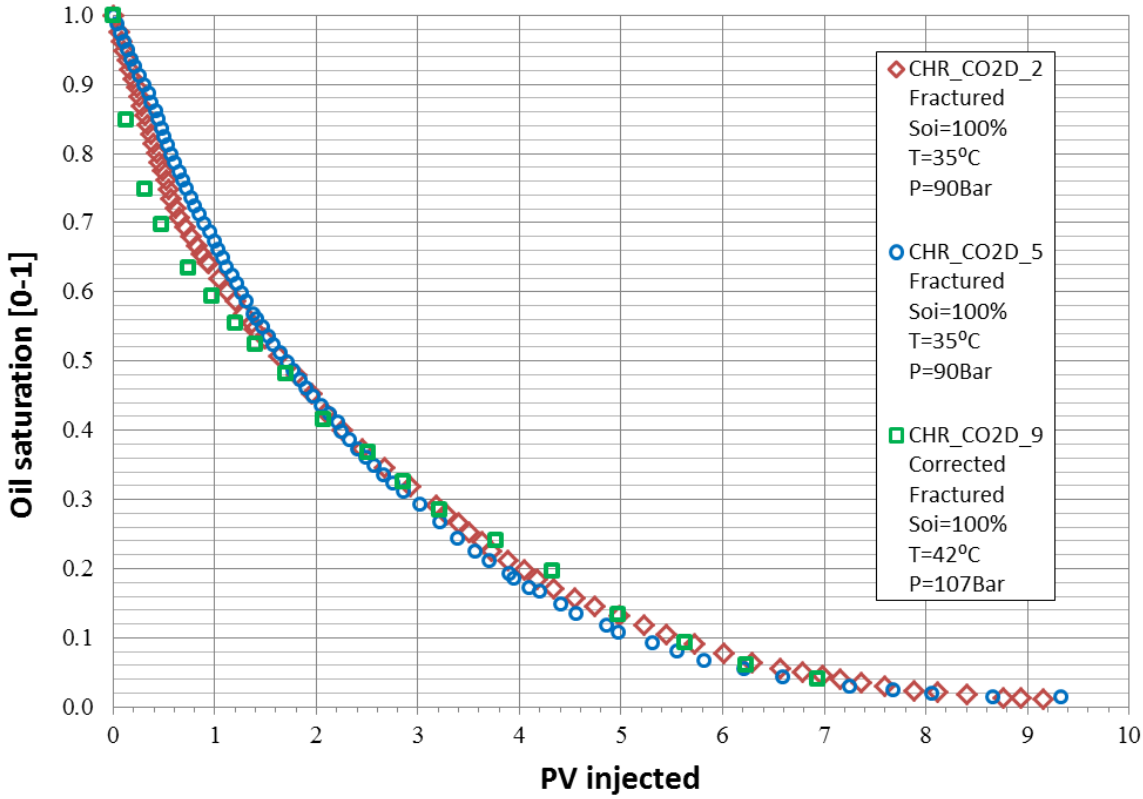

Figure 6.20: Calculated oil saturation as a function of pore volumes injected for the two 100% oil saturated core experiments conducted at UoB and the CO_2 injection experiment conducted in Bartlesville. The graphs indicate a slight variation in oil production rate predicted to be caused by delayed and accelerated production through the BPR. The corrected graph for CHR_CO2D_9 is based on predictions with the absence of temperature fluctuation in which causes some uncertainty when compared to other tests. The graphs overlap after 1.6 PV of CO_2 injected with final recoveries above 95% OOIP and no significant discrepancy on reduction in oil saturation can be recognized.

6.3.6 Gravity effects

Increased CO_2 concentration in the upper part of the core as time commenced was observed in **Figure 6.10**. At experimental conditions, CO_2 and n-decane has a density of 0.622 g/ml and 0.722 g/ml, respectively. **Figure 6.21** shows how the core was digitally sliced in the middle of the core along the fracture plane to investigate gravitational effects.

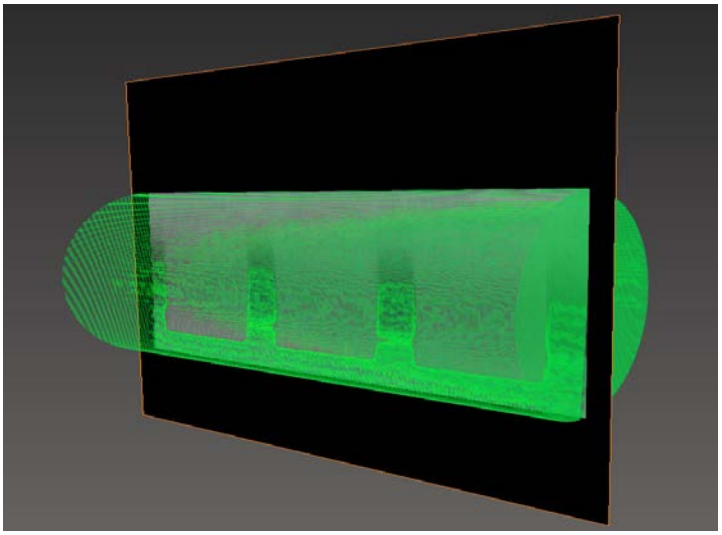

Figure 6.21: Illustration of where the core was digitally cut for visualization of gravity effects.

Figure 6.22 shows the calculated oil saturation development caused by gravity effects at various time steps. Inlet side is on the right (injection) and the outlet side if on the left (production). Warm colors indicate high oil saturations and cold colors indicate low oil saturation. The spacer is highlighted in white color to only observe the spatial saturation distribution in the fracture caused by gravity effects during the test. The CO_2 enters the bottom part of the core. After approximately 5.3 hours the oil in the fracture was completely displaced. Already at this time step there was a higher CO_2 concentration in the upper part of the core caused by gravity effects. A buildup of CO_2 in the upper part of the core was observed as time commenced.

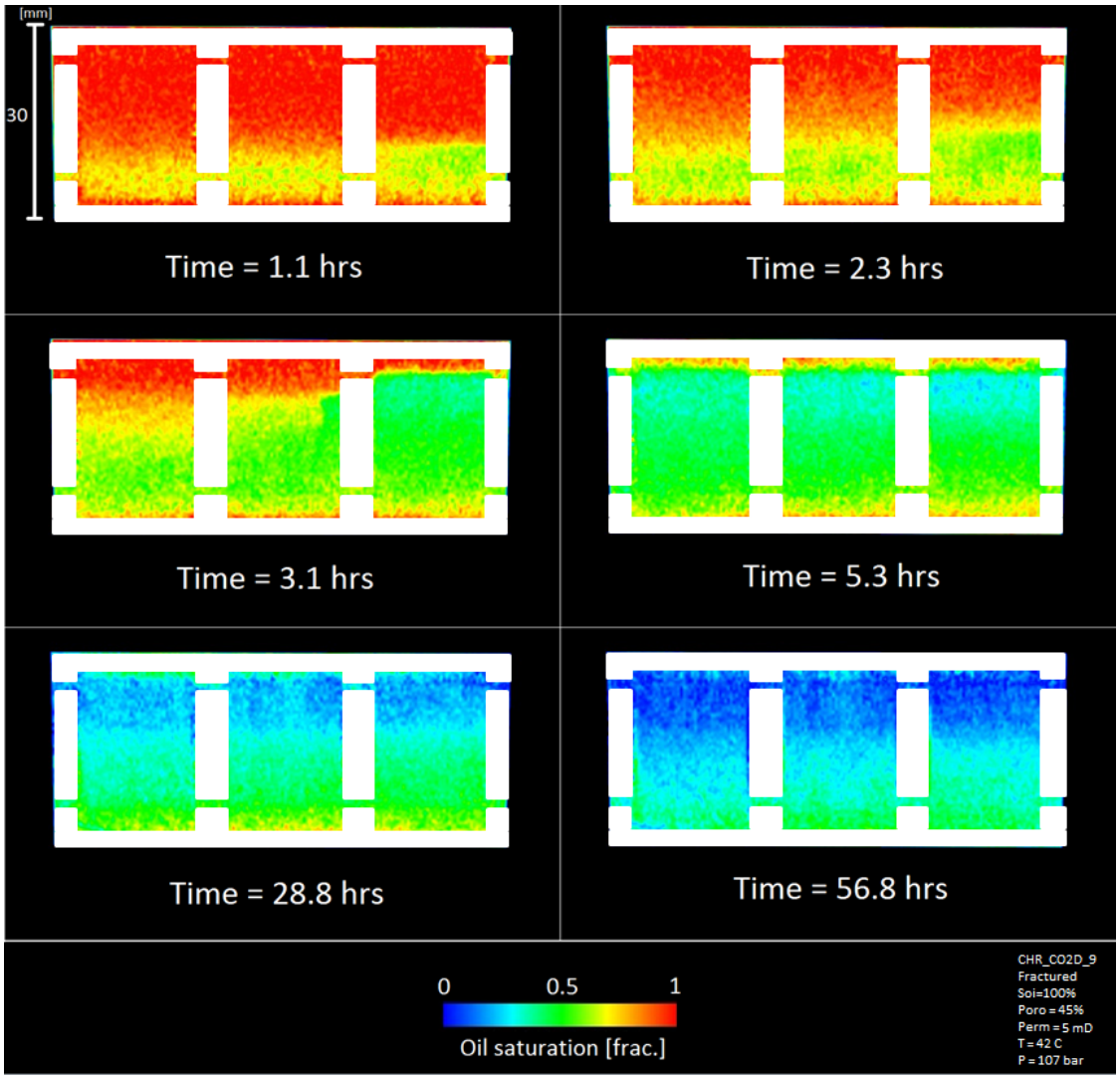

Figure 6.22: Calculated oil development in the middle of the core along the fracture. The CO_2 enters the core in the bottom part of the core from the right side. After the oil in the fracture is displaced, a higher buildup of CO_2 saturation at the top part of the core is observed as time goes by. The inlet (injection) is on the right of the images and outlet (production) is on the left side. The spacer is indicated in white to only highlight the saturation distribution in the fracture caused by gravity effects.

Figure 6.23 illustrates the line probe location for investigating gravity by calculating CO_2 concentration in the upper and lower parts of the core in addition to a graph showing calculated CO_2 concentration versus length of the core after 56.8 hours. Two line probes were placed in the matrix beside the fracture in the top (blue line) and bottom (red line) of the core. A higher CO_2 concentration in the upper part of the core is observed. The CO_2 concentration is slightly higher at the inlet and outlet of the core than in the middle resulting from diffusion from the end pieces.

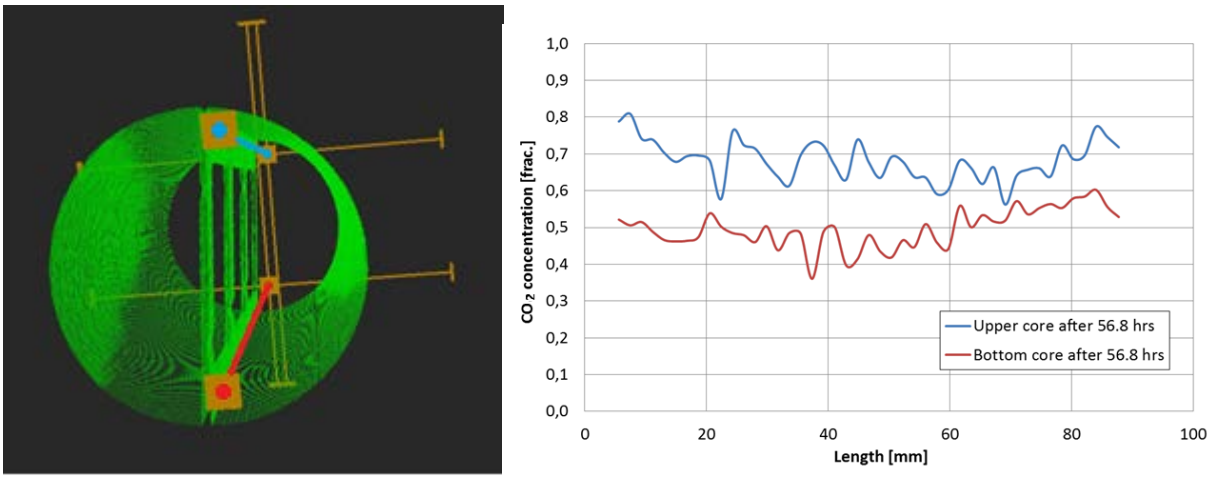

Figure 6.23: Line probe location to investigate gravity effects in addition to calculated CO_2 concentration in the upper and lower part of the core after 56.8 hours of injection. The line probes were placed in the matrix along the fracture plane to observe variations in CO_2 saturation throughout the core because of density differences of the present fluids. The red lines indicate where the CT values were obtained. The CO_2 concentration is higher in the top part of the core resulting from gravity effects. The red lines indicate where the upper and bottom line probe was placed. A higher CO_2 concentration at the inlet and outlet is observed because of end effects, e.g. diffusion from the end pieces.

6.3.7 Periodical stop in production

The periodic temperature fluctuations during the nights caused the line pressure to decrease below the regulated back pressure, leading to a halt in production. Still, CO_2 was injected into the core and mass transfer of oil took place from the matrix to the fracture by diffusion during these time periods. The oil saturation increased in the fracture during the night and was produced from the fracture in the morning when the room temperature increased. The injection rate was too low to observe any increase in line pressure caused by buildup of CO_2 during the halt in production.

Figure 6.24 shows the development in oil saturation in the fracture before and after halt in production as time commenced. T = 28.8 [hours] was before the stop in production from the core. T = 44.0 [hours] shows an increased oil saturation in the fracture after the stop in production. Increased oil saturation in the fracture is observed. Production was recommenced and at T = 50.2 [hours] and at T = 51.1 [hours] the oil is displaced from the fracture.

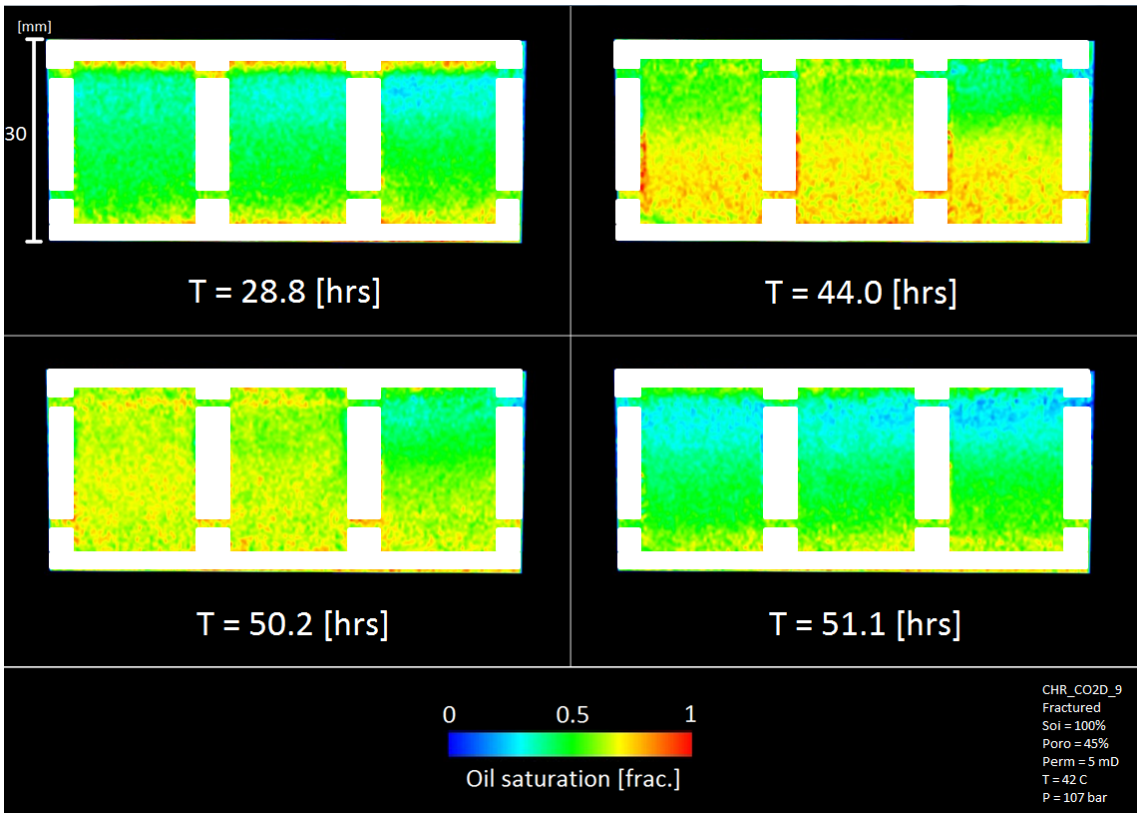

Figure 6.24: Calculated oil saturation before and after halt in oil production. T = 28.8 [hours] is before the stop in production. Oil saturation increased in the fracture during halt in production. T = 44.0 [hours] indicate buildup of oil in the fracture after the halt in production. T = 50.2 [hours] and T = 51.1 [hours] shows that oil is displaced from the fracture after oil production was recommenced. The spacer is indicated in white to only observe the saturation distribution occurring in the fracture.

6.4 CMG GEM simulations

Numerical simulations have been performed with CMG GEM simulator to match experimental data from the supercritical CO_2 injection visualized in CT. The procedure is explained in section 5.8. The method of calculating the effective diffusion coefficient was based on the numerical simulation conducted by Alavian and Whitson (Alavian and Whitson, 2012).

6.4.1 Matching CMG GEM simulations with experimental results

Figure 6.25 shows development in oil saturation as a function of time for the supercritical CO_2 injection (CHR_CO2D_9) corrected for temperature fluctuations (red circles) and the recovery graph obtained from numerical simulation (P = 92 bar, T = 20 °C). Both show a decrease in oil saturation versus time during the first three days of CO_2 injection (out of 6 days total injection time). The simulation model was able to reproduction oil production up to approximately three days of CO_2 injection, after which the recovery in the simulation was less efficient, compared to the experimental results. Several simulations were run with different diffusion coefficients and an absolute diffusion coefficient of D_a = $1*10^{-8}$ m^2/s was found to give the best match.

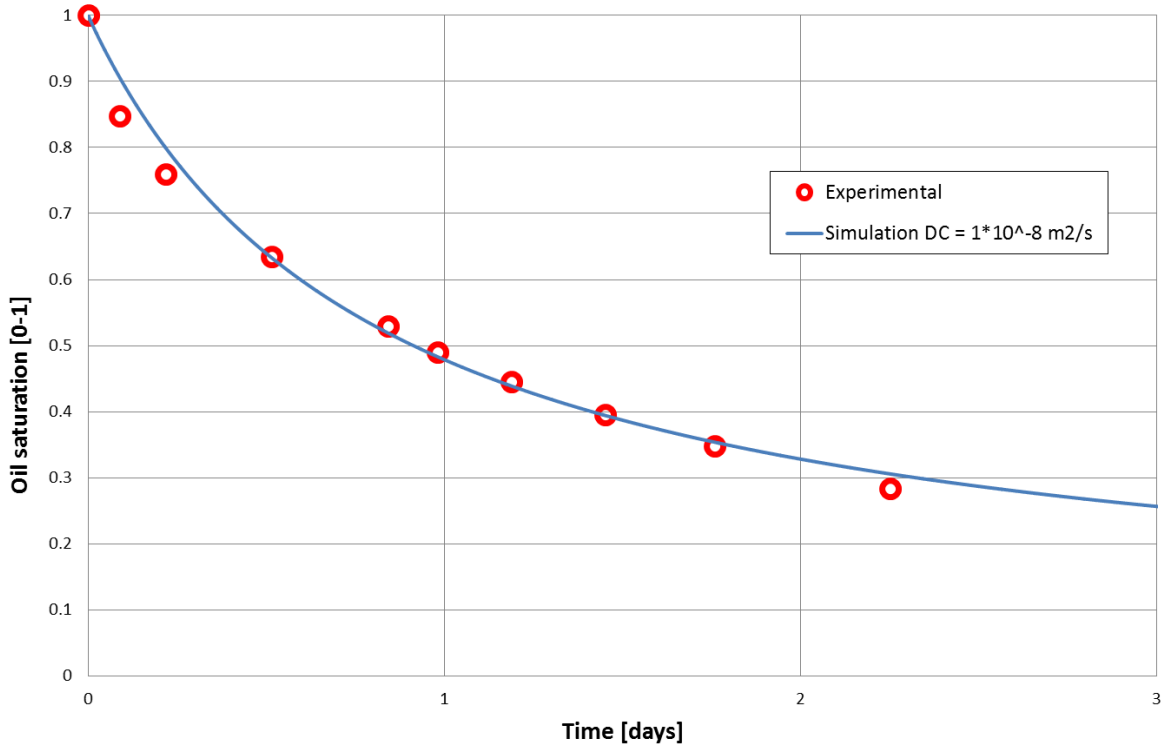

Figure 6.25: Development in oil saturation as a function of time for the supercritical CO_2 injection (CHR_CO2D_9) corrected for temperature fluctuations (red circles) and the recovery graph obtained from numerical simulation (P = 92 bar, T = 20 °C). The graphs overlap until approximately 1.6 days of CO_2 injection. After this point, a discrepancy can be recognized from the graphs, probably caused by the absence of oil swelling in the numerical simulation.

Higher recovery efficiency from the experimental CO_2 injection at supercritical conditions rather than the simulated liquid CO_2 injection is observed after 2.2 days of CO_2 injection in **Figure 6.25**. Possible reasons why this occur:

- The simulation does not account for oil swelling which leads to lower recovery efficiency. Dissolution of CO_2 cause oil to swell up to 50-60% and thereby increases the contact area between the oil and CO_2 in which increase diffusion rate and recovery efficiency for the supercritical CO_2 injection experiment (Firoozabadi, 2010, Iglauer, 2011a, Sohrabi et al., 2007).

- The CO_2 phase in the numerical simulation is in liquid state while it is in supercritical in the supercritical CO_2 injection experiment.

Higher recovery efficiency has been observed from subsequent CO_2 flooding into Rørdal chalk at supercritical conditions compared to liquid conditions through experimental work (Haugen, 2012). This may contribute to lower recovery efficiency in the numerical simulation because the CO_2 was in liquid state rather than supercritical state. Several attempts on achieving supercritical conditions in the simulation were made without success. Beyond the critical point of CO_2 (see **Figure 3.3**) there was no transfer of fluids between the fracture and the matrix in the simulator. The graphs were compared under the assumption that mixing with n-decane by diffusion remains the same for liquid CO_2 and supercritical CO_2 under miscible conditions.

Figure 6.26 shows dynamic 3D images of the simulation model in addition to the CT images obtained from the visualization experiment at different time steps. Each image represents the same location (both simulated and experimental) of the core at different time steps from a birds-eye view where diffusion of CO_2 occurs from all open end faces (fracture and end pieces) at the right, top and bottom side in all images. The time is indicated at the bottom of each image. Warm colors indicate high oil saturations and cold colors indicate low oil saturation. A good match between numerical simulation and experimental CT images was obtained up to 13.6 hours of injection (first four images). A slight discrepancy between the experimental and simulated oil saturation was observed late in the injection test (last three images), caused by noise and uncertainties in the raw CT data. The uncertainty was more pronounced at low oil saturations because of the small difference in CT values; see e.g. the last CT image show bright color with no oil present in the matrix whereas the image from the simulation is dark blue. More information about uncertainties related to CT scanning in section 6.8.

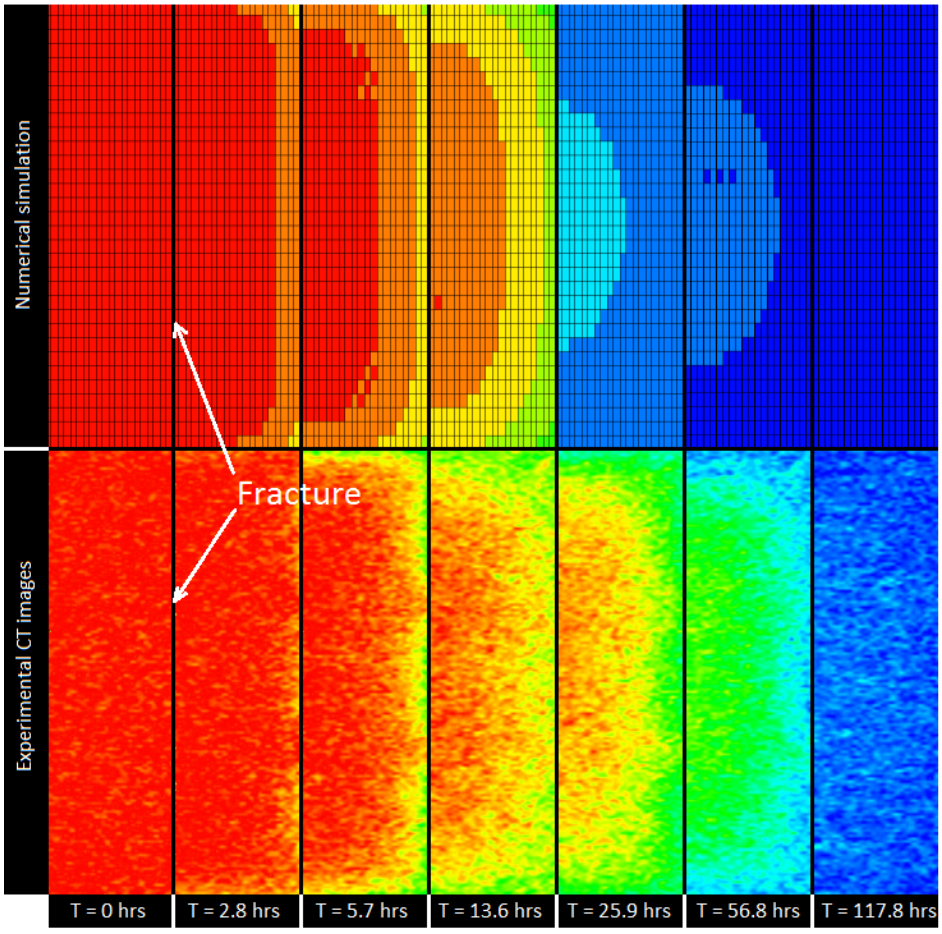

Figure 6.26: Comparing 3D images obtained from numerical simulation performed with CMG GEM in addition to the CT images obtained from the CO_2 injection experiment (CHR_CO2D_9). The upper 6 images represent the numerical simulation and the lower 6 images are the CT images obtained from the experiment; both used to visualize oil recovery by CO_2 diffusion from the fracture. The last three images of the injection (after 13.6 hours) present a discrepancy in colors caused by noise and uncertainties related to the raw CT data.

6.4.2 Calculation of oil production based on the numerical simulation

CMG GEM counts both CO_2 and n-decane as one oil phase since both fluids are miscible under the simulated conditions. To estimate the oil production from the matrix, i.e. mass transfer of n-decane from the matrix to the fracture, the oil components of CO_2 and n-decane given in moles was plotted as a function of time by using CMG Results Graph. The fluid saturation and consequently the oil production from the matrix were calculated from the values obtained from this graph. **Figure 6.27** shows the plot obtained from CMG Results Graph.

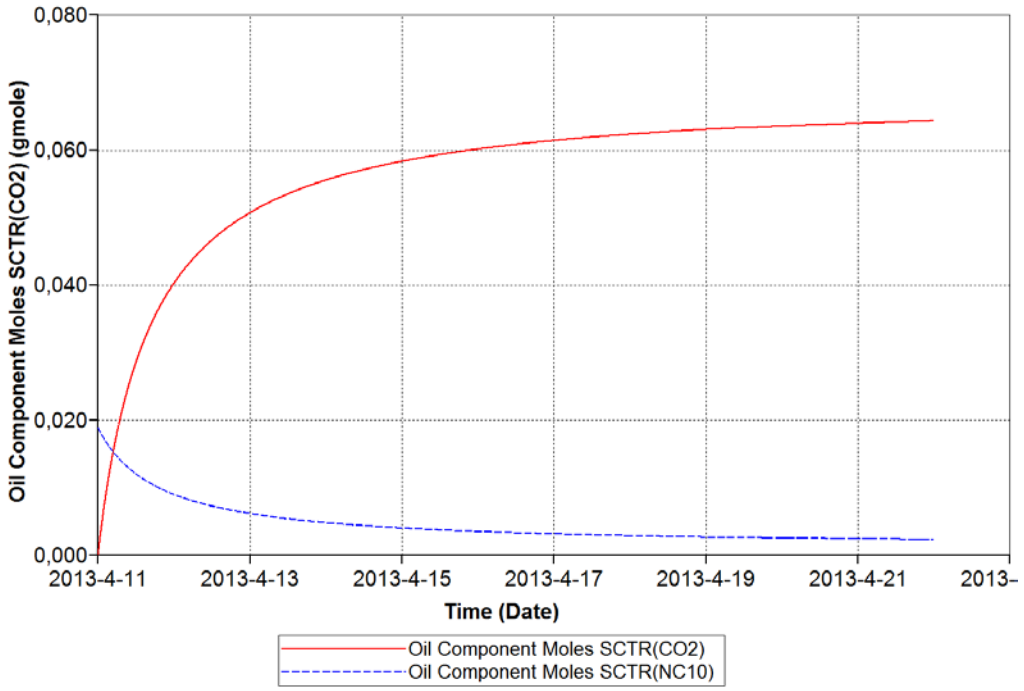

Figure 6.27: Oil components in moles for CO_2 and n-decane in the matrix as a function of time given in date. Changes in fluid saturation and consequently the oil production in the matrix were calculated from the obtained values.

6.4.3 Calculating the effective diffusion coefficient by CMG GEM simulation

An absolute diffusion coefficient of $D_a = 1*10^{-8}$ m^2/s was estimated from fitting numerical simulation to experimental results displayed in **Figure 6.25**. By the use of equation 5.3, with a cementation factor from the Valhall field, the effective diffusion coefficient was calculated to be $D_e = 3.02*10^{-9}$ m^2/s. A good match was obtained compared to the result from the visualization experiment ($D_e = 1.66*10^{-9}$ m^2/s) and also with results from Renner and Grogan displayed in **Figure 6.17** (Grogan et al., 1988, Renner, 1988).

6.4.4 Sensitivity analysis

A sensitivity parameter study was conducted with known parameters that influence oil production by diffusion. The porosity, permeability and the diffusion coefficient was changed separately one at a time, to observe to which extent the individual parameter impact oil production. Production graphs were made for each individual simulation and the average error were calculated based on the discrepancy from the fitted simulated production graph showed in **Figure 6.25**. Each data point in the error graphs represent an average error from a simulation based on the reduction in oil saturation from T = 0 [days] to T = 3 [days] and ranging from 0 to 100 saturation units. An important observation was made; a hysteresis in the production graph was observed when changing the dimensions of the fracture area filled with CO_2. All simulations conducted in this thesis were based on a static fracture-to-matrix-area ratio. This has to be taken into consideration in further simulations based on this model.

Porosity

Figure 6.28 shows the reduction in oil saturation as a function of time for three different porosities in the matrix. A change in porosity had a significant impact on the oil recovery. In the case of high matrix porosity, a larger volume of oil needs to be extracted from the matrix, resulting in lower recovery efficiency than for low matrix porosity, where the volume of oil recovered by diffusion is less and leading to higher recovery efficiency.

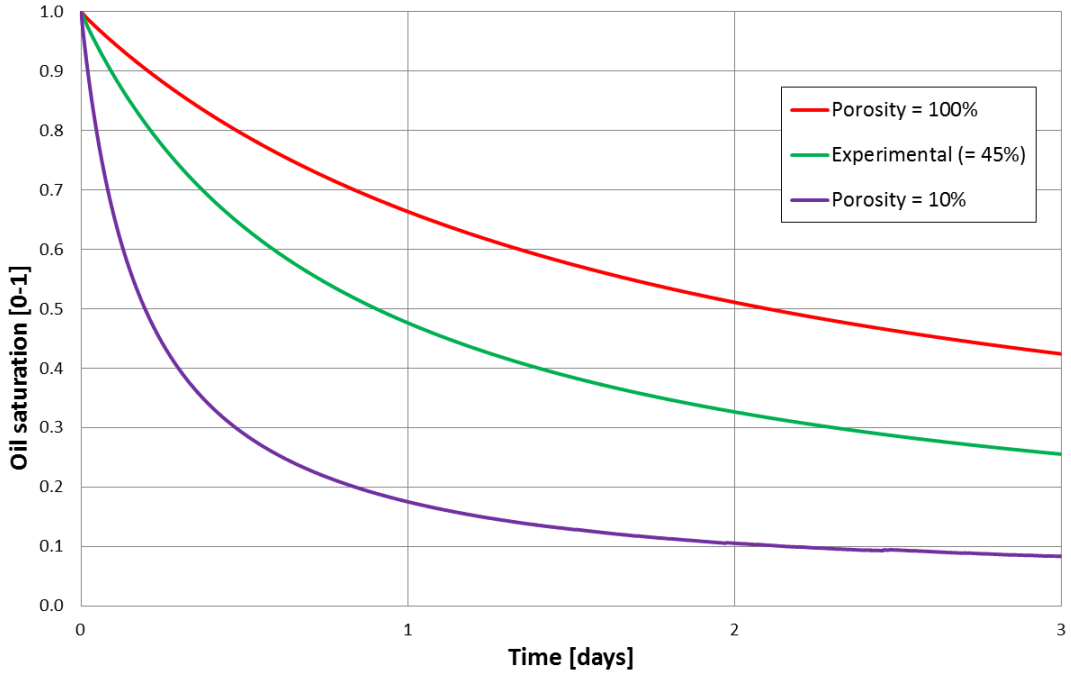

Figure 6.28: Reduction in oil saturation for analogue simulations only varying the porosity. A change in porosity has a significant impact on the oil recovery rate. The green line represents the experimental value of porosity (=45%). In a scenario with high porosity (=100%) the oil production rate is slow, while a low porosity (=10%) leads to a fast oil production rate as the total volume of oil that was extracted from the matrix is a lot less.

Figure 6.29 shows the error in saturation units as a function of average matrix porosity. A higher error was observed at a low porosity than for a high porosity. The higher error at a low porosity (< 19%) was predicted to be caused by an accelerated oil production from the matrix as the amount of oil extracted by diffusion was much smaller. In addition, a larger discrepancy between the experimental matrix porosity and the low porosity graph can be recognized from **Figure 6.28**.

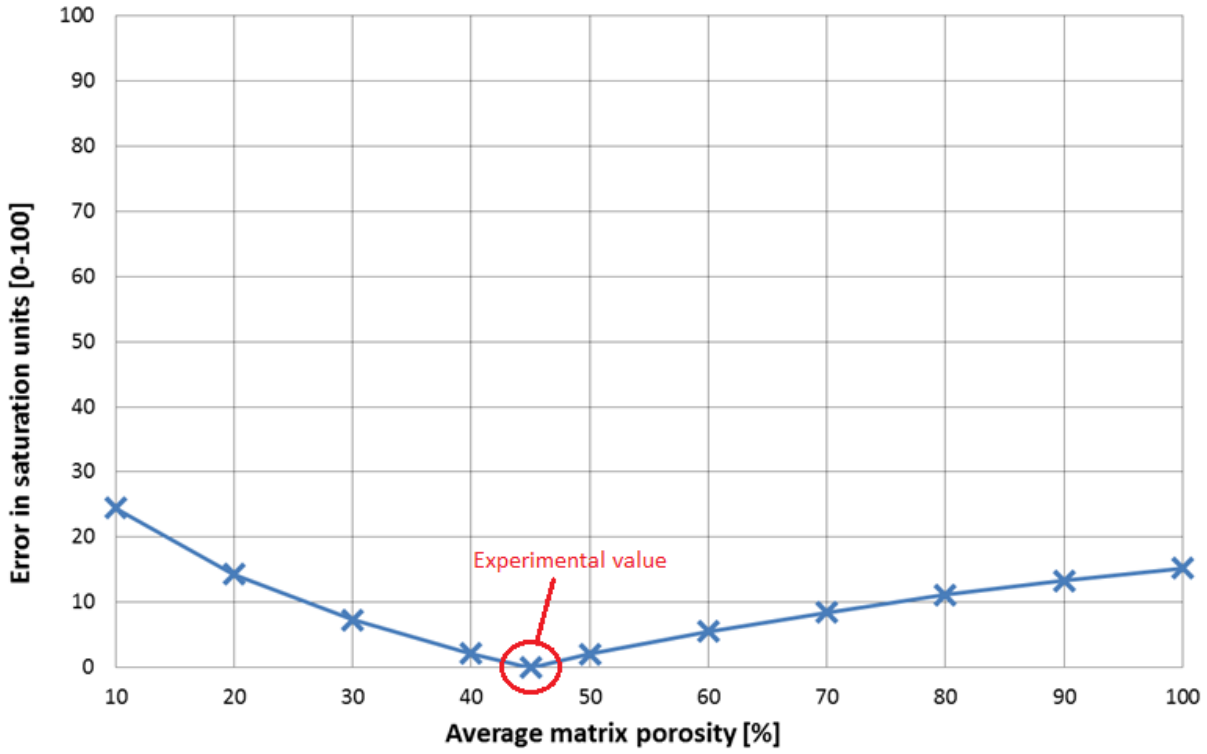

Figure 6.29: Error in saturation units as a function of average matrix porosity. A higher error was observed at a lower porosity than a high porosity. The experimental value of matrix porosity is highlighted in figure (red circle).

Absolute Permeability

Figure 6.30 shows the calculated error in saturation units when changing the absolute matrix permeability from 1nD-1D, over 6 orders of magnitude. Several numerical simulations was conducted with a variation in permeability and showed no significant impact on oil recovery; even with permeability as low as 1 nD (typical permeability of shale) and as high as 1D (typical permeability of fractures) the reduction in oil saturation remained the same.

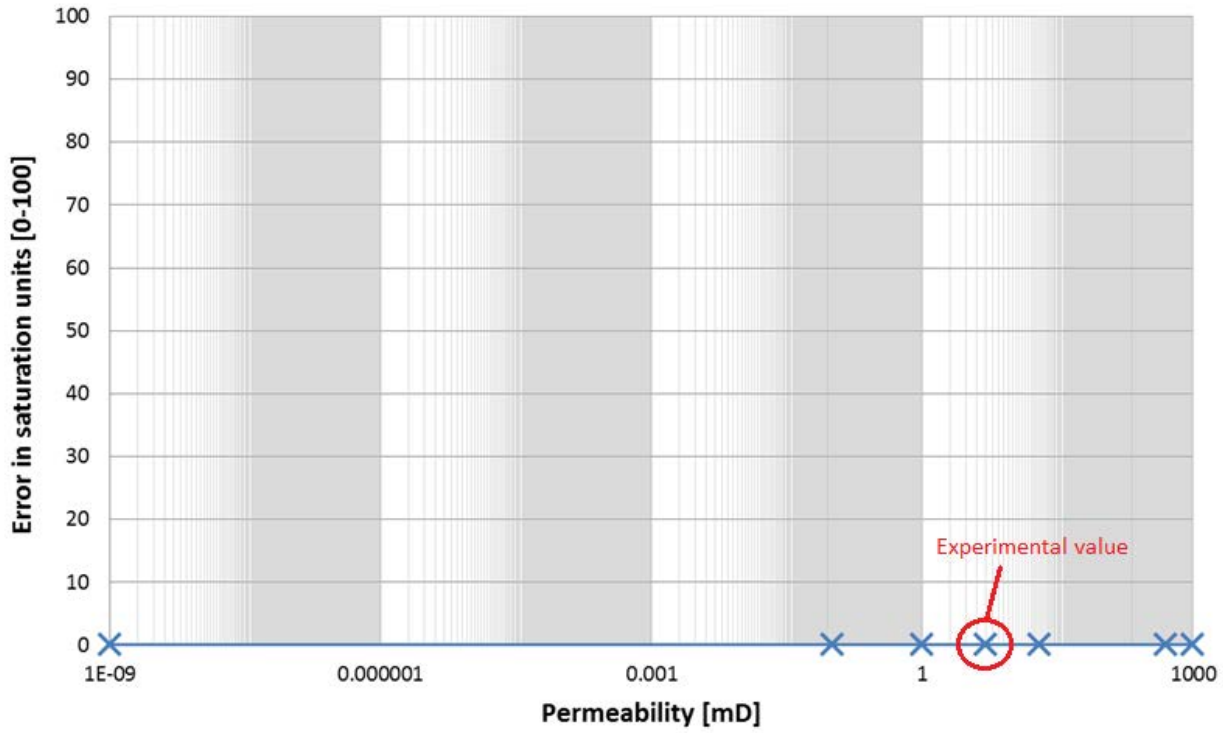

Figure 6.30: Error in saturation units as a function of permeability. Permeability is given as a logarithmic scale and showed no impact on oil recovery in this model with all errors below 0.0012. The experimental value of permeability in the matrix is highlighted in the figure (red circle).

Diffusion coefficient

Figure 6.31 shows the error in saturation units as a function of absolute diffusion coefficient. The diffusion coefficient had a significant impact on oil recovery and the error was higher with a lower diffusion coefficient than a higher diffusion coefficient. A reduction in diffusion coefficient leads to a significant reduction in oil production rate. This will lead to an increased error when reducing the diffusion coefficient because the oil production is compared after 3 days (experimental time). The error of a higher diffusion coefficient reached a plateau on the right in the figure. This plateau is caused by limitation of the diffusion rate as the size of the model and the amount of oil that can be extracted from the matrix remains the same. Larger matrix dimensions would result in a larger average error recognized by a higher plateau value when further increasing the diffusion coefficient.

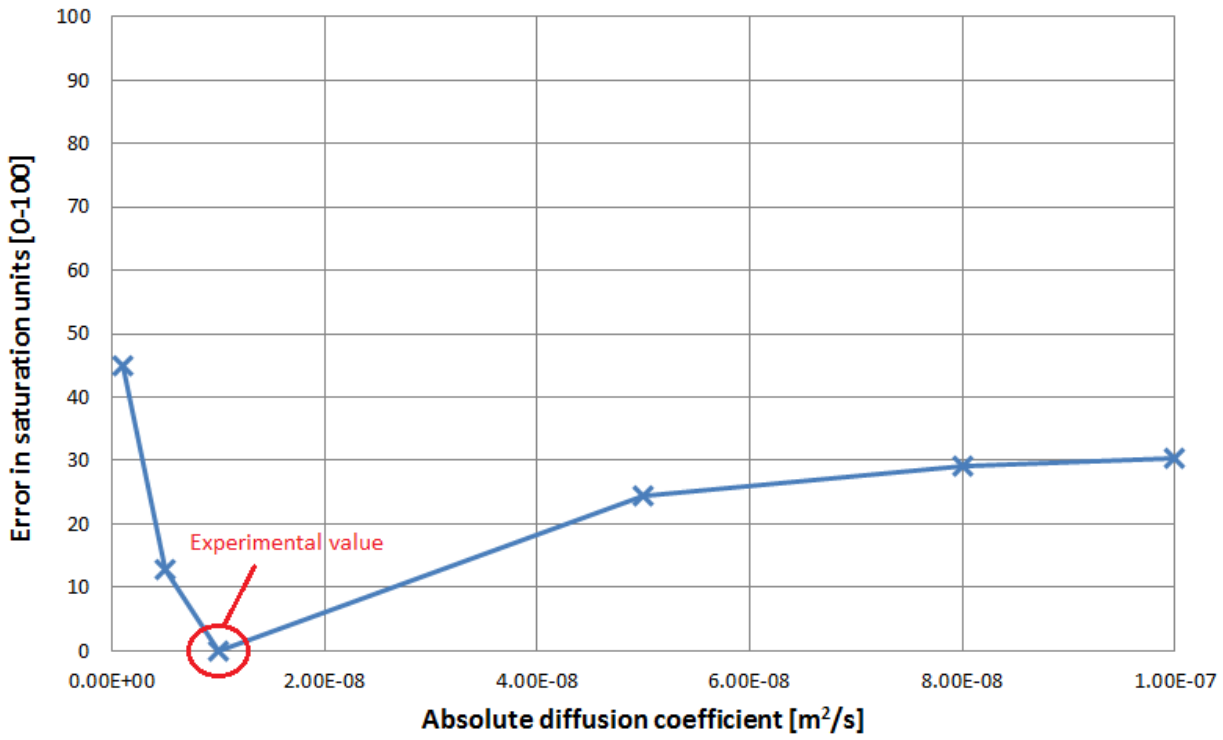

Figure 6.31: Error in saturation units as function of absolute diffusion coefficient for the simulation model. A higher error was observed for lower diffusion coefficients since inconsiderable amounts of oil were recovered from the matrix. The diffusion coefficient that gave the best match with experimental data is highlighted (red circle).

6.4.5 Up scaling the area of diffusion

Figure 6.32 shows the reduction in oil saturation as a function of time for the same model as displayed in **Figure 6.25**, only scaling up the matrix area containing oil while the ratio between length and width remains the same. **Table 6.5** lists the associated lengths and widths used in the model in addition to the total volume of oil in the matrix. The oil production does not reflect a real scenario since the assumption is based on our simulation model with limiting conditions (e.g. n-decane as oil phase, 100% oil saturated matrix, no viscous- or gravitational forces present) and a fracture network continuously flooded with CO_2 would not be economical. It is more for conceptualizing the impact of diffusion at larger scales with the use of this model. To compare the scale of the simulated 2 dimensional block with actual matrix blocks found in a fractured petroleum reservoir; matrix blocks in the Tor formation in the Ekofisk field at NCS were measured to be between 0.3 to 0.9 meters wide (Thomas et al., 1987).

Table 6.5: Dimensions on grid for up scaling

Scale	Length [m]	Width [m]	Oil volume [m^3]
Experimental	0.084	0.017	0.001
2x	0.169	0.033	0.003
5x	0.422	0.083	0.016
10x	0.845	0.166	0.063
20x	1.690	0.332	0.252

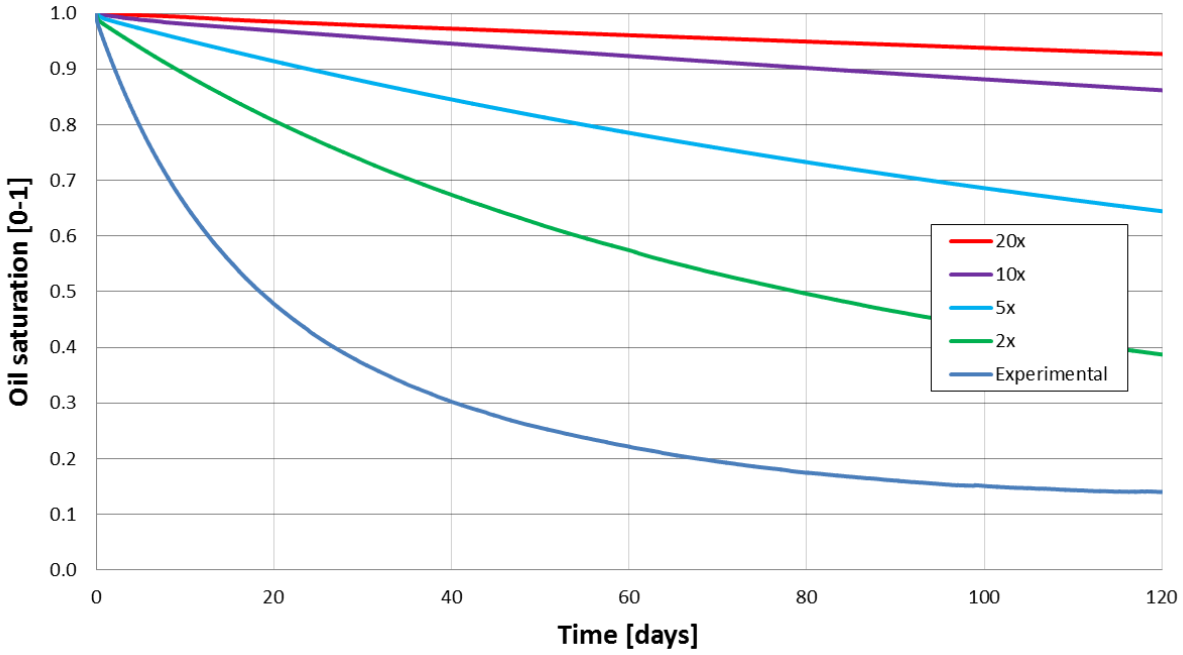

Figure 6.32: Reduction in oil saturation as a function of time for the numerical simulation. The matrix is scaled up with varying lengths and widths to observe the impact of on total oil recovery from larger matrix blocks by diffusion. As expected, larger blocks up to 1.69 meter in length and 0.33 meter width require longer time to recover the same amount of oil compared to smaller matrix blocks and experimental scale.

6.4.6 Miscible conditions versus immiscible conditions

Figure 6.33 shows the reduction in oil saturation in the matrix as a function of time for a miscible displacement and an immiscible displacement. The simulations was run to observe the impact on oil recovery from the matrix to the fracture by diffusion in a scenario where the CO_2 and n-decane is under immiscible conditions (P = 1 bar, T = 20 °C). The reduction in oil saturation does not replicate a field application since the simplified model is based on recovery by molecular diffusion alone and no viscous forces are present; it was run to observe the impact on oil recovery from matrix blocks of achieving miscibility in high conductivity fracture systems in fractured reservoirs. As expected, no reduction in oil saturation in the matrix was observed and confirmed that no oil is displaced from the matrix in an immiscible CO_2 displacement.

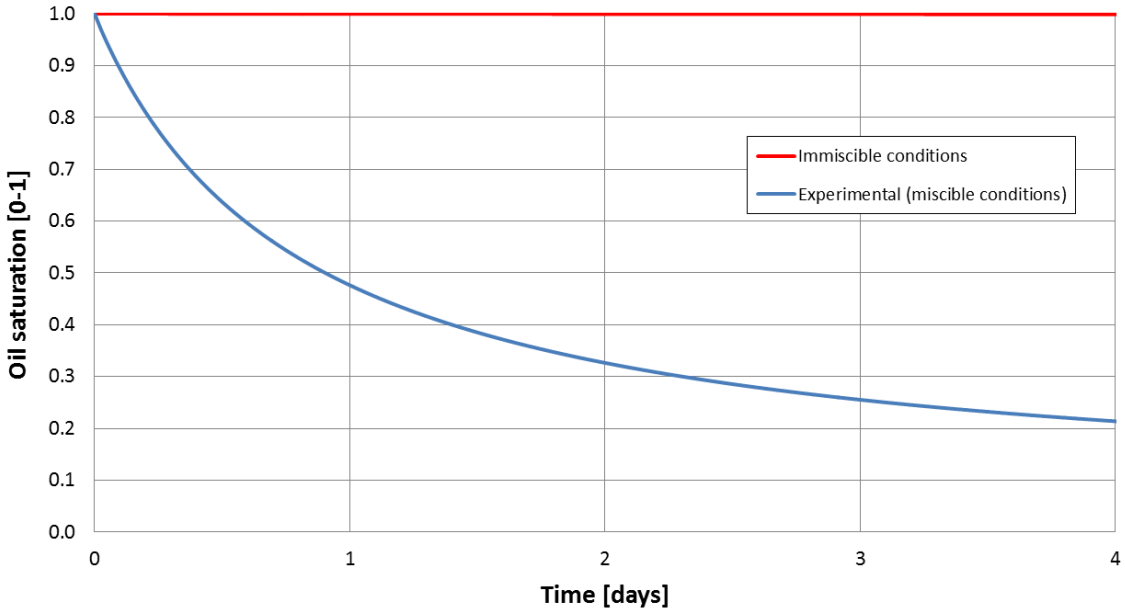

Figure 6.33: Reduction in oil saturation for miscible and immiscible conditions as a function of time. No reduction in oil saturation from the matrix at immiscible conditions was observed. The reduction in oil saturation does not replicate a real scenario since the model is based on recovery by molecular diffusion alone and no viscous forces are present.

6.5 Supercritical CO_2-foam injection visualized in CT

The CO_2 injection test presented in chapter 6.4 was conducted in an ideal fractured system (e.g. no initial water present, 100% CO_2 saturation in the fracture at all times) at experimental scale. Introducing foam includes injecting water (mixed with surfactant) simultaneously with the CO_2. The presence of water has been reported to slow down diffusion processes leading to less efficient oil recovery on experimental scale (Grogan, 1987). The small scale of this injection test caused the displacement to be equally dominated by both diffusion and viscous effects. On field scale the displacement would be governed by viscous forces generated by the foam.

CO_2 and a surfactant solution were co-injected with a gas fraction of 90% into a fractured 1.5" chalk core for 3 days. Experimental conditions are given in **Table 6.4**. Short experiment duration was because of limitation in the time schedule for using the CT-scanner. A total of 21 scans were taken during the CO_2-foam experiment. **Figure 6.34** shows the dry CT scan of the core (CHR_CO2F_10) used in this experiment.

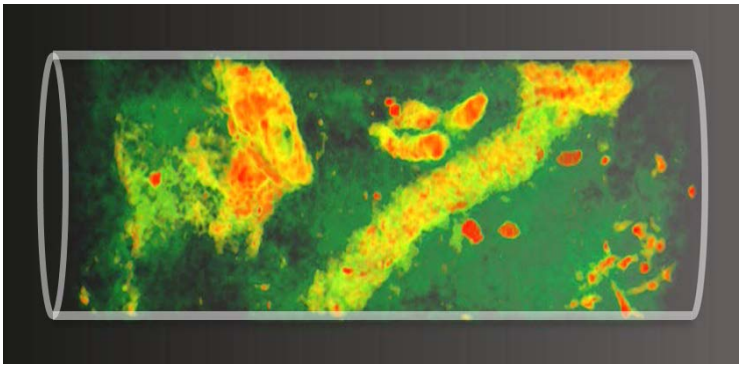

Figure 6.34: Dry scan of CHR_CO2F_10 used in the supercritical CO_2-foam experiment.

The core was initially 100% oil saturated. The development in oil saturation was calculated by equation for visualization purposes, although no preliminary CT scan of the core 100% saturated with surfactant could be obtained (as explained in section 4.1.1). Introducing a third phase (surfactant) to the system will result in an irregular calculation of CO_2 distribution in the matrix. For this reason a molecular diffusion coefficient was not estimated from this experiment.

Figure 6.35 shows the oil development from calculated saturations obtained from CT-values from all 21 scans. Warm colors indicate high oil saturations and cold colors indicate low oil saturation. Each image represents the same location of the core at different time steps from a birds-eye view, where CO_2 and surfactant are co-injected at the bottom of the image and produced at the top. The time is indicated at the bottom of each image. A viscous displacement front was observed on the inlet side as time commenced.

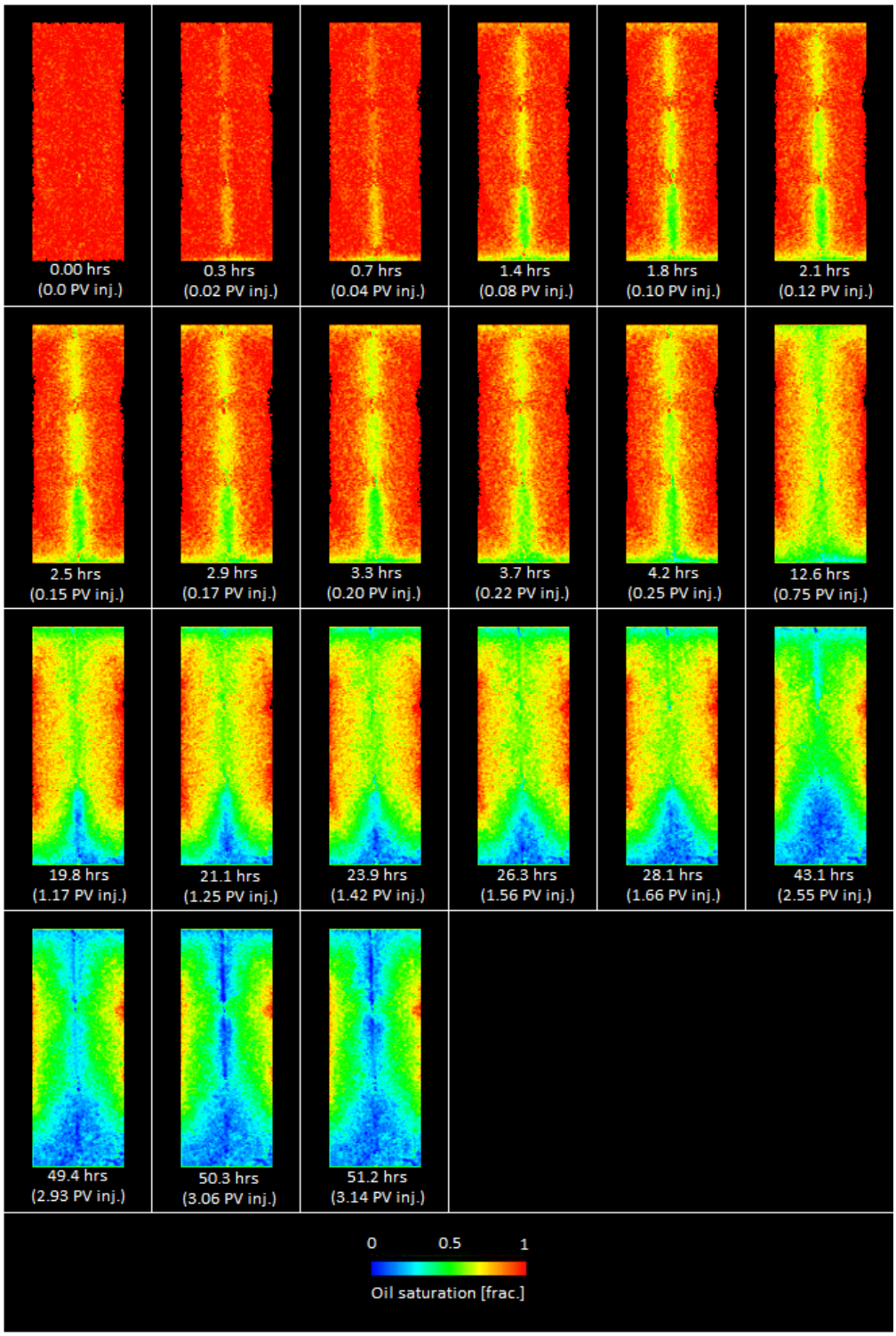

Figure 6.35: Calculated oil development for the CO_2-foam experiment. Warm colors indicate high oil saturations and cold colors indicate low oil saturation. The core is horizontally digitally sliced perpendicular to the fracture to observe recovery mechanisms from a birds-eye view. Supercritical CO_2 and a surfactant solution were co-injected from the bottom side of the core in the images. A viscous displacement front was observed on the inlet side as time commenced.

Figure 6.36 shows the oil development in the middle of the core (X_L = 0.5). Warm colors indicate high oil saturations and cold colors indicate low oil saturation. Compared to the CO_2 injection, the CO_2 saturation followed the same trend and entered the lower parts of the fracture in the beginning of the test and then gradually increased in the top of the core as time commenced.

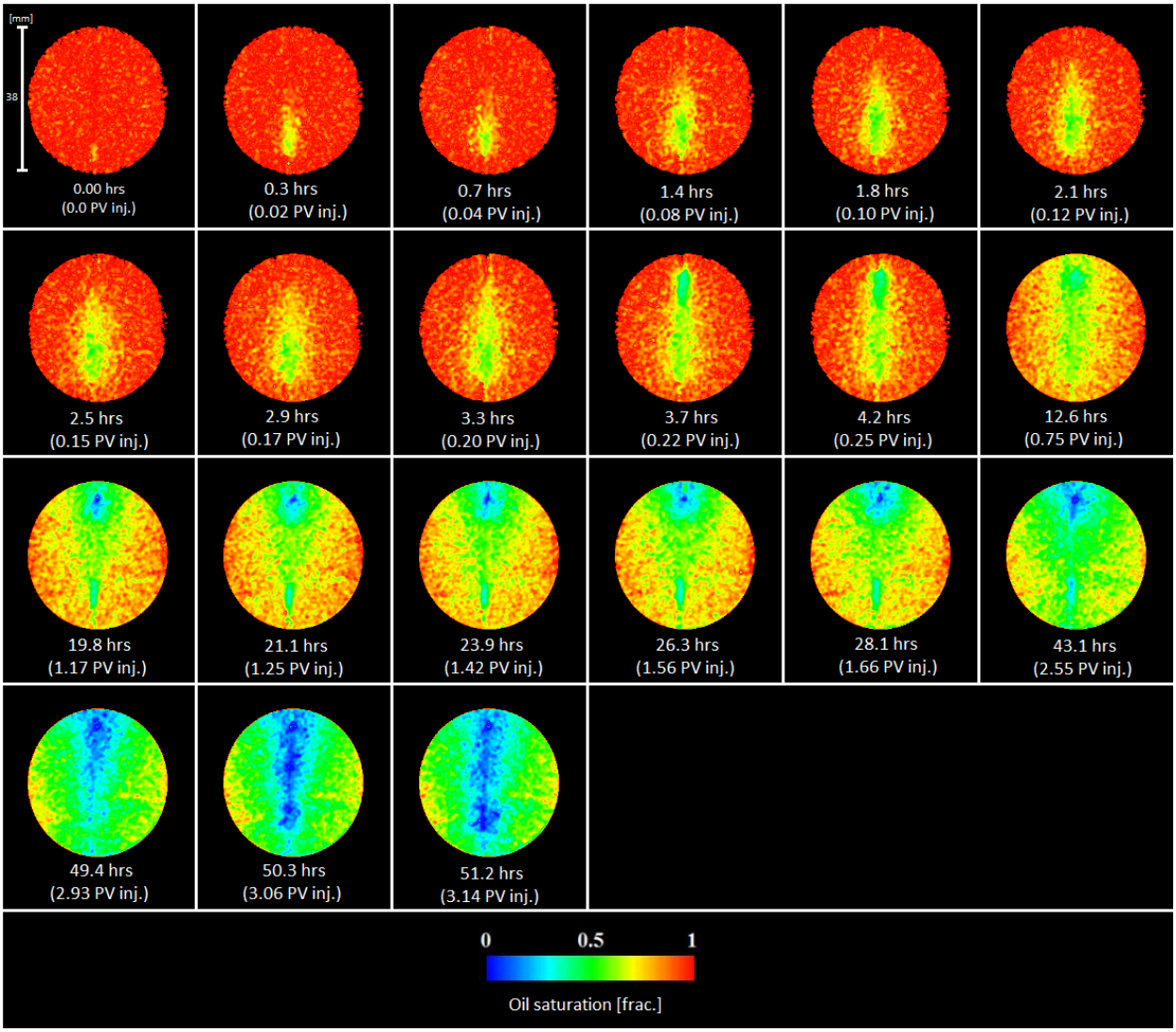

Figure 6.36: Calculated oil development in a vertical slice in the center of the core at different time steps. Warm colors indicate high oil saturations and cold colors indicate low oil saturation. A length scale is indicated on the left on the first image (38 mm). CO_2 mixed with surfactant solution entered the lower parts of the fracture first and then gradually segregated towards the top of the fracture as time commenced.

6.5.1 Material balance calculation

Figure 6.37 shows the oil recovery as a function of pore volume of supercritical CO_2 injected with the associated differential pressure across the core (CHR_CO2F_10). The low differential pressure across the core indicates that the foam was being destroyed. It was determined to be a result of no initial water being present in the pores. Foam getting destroyed or weakened at low water saturations have been observed in other experiments (Zanganeh et al., 2011), as the foam dries out and partially collapses abruptly at a water saturation corresponding to the "limiting capillary pressure" (Khatib et al., 1988, Rossen et al., 1995). The stability of the lamella depends on the capillary pressure in the surrounding medium and without the absence of water the high capillary pressure causes the lamella to break and collapse (Khatib et al., 1988).

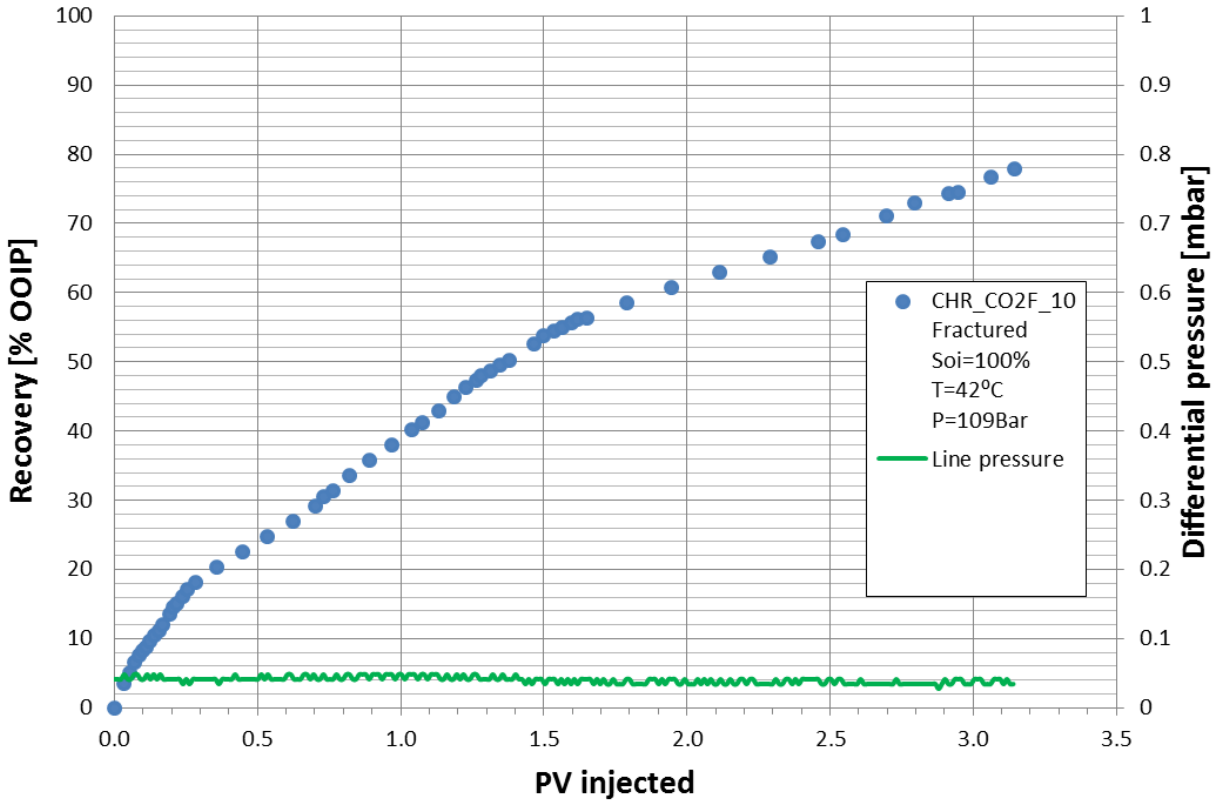

Figure 6.37: Calculated oil recovery from material balance as a function of supercritical CO_2 injected. The low differential pressure across the sample, despite co-injection of CO_2 and surfactant for foam generation, indicated that the foam was being destroyed upon entering the pore structure.

The displacement front seen at the inlet side on the core in **Figure 6.35** is believed to be foam generation through spontaneous water imbibition at the inlet. Concentration of surfactant solution is higher at the inlet. Water in the surfactant solution may spontaneously imbibe into the matrix because Rørdal chalk has a preference for water. To see if foam could be generated, the injection rate was set ten times higher at the end of the experiment but no increase in differential pressure was observed. **Figure 6.38** shows the production of both the CO_2 injection and the CO_2-foam experiment to compare the results. The CO_2 foam injection seems to be more efficient than the CO_2 injection but not as good as expected.

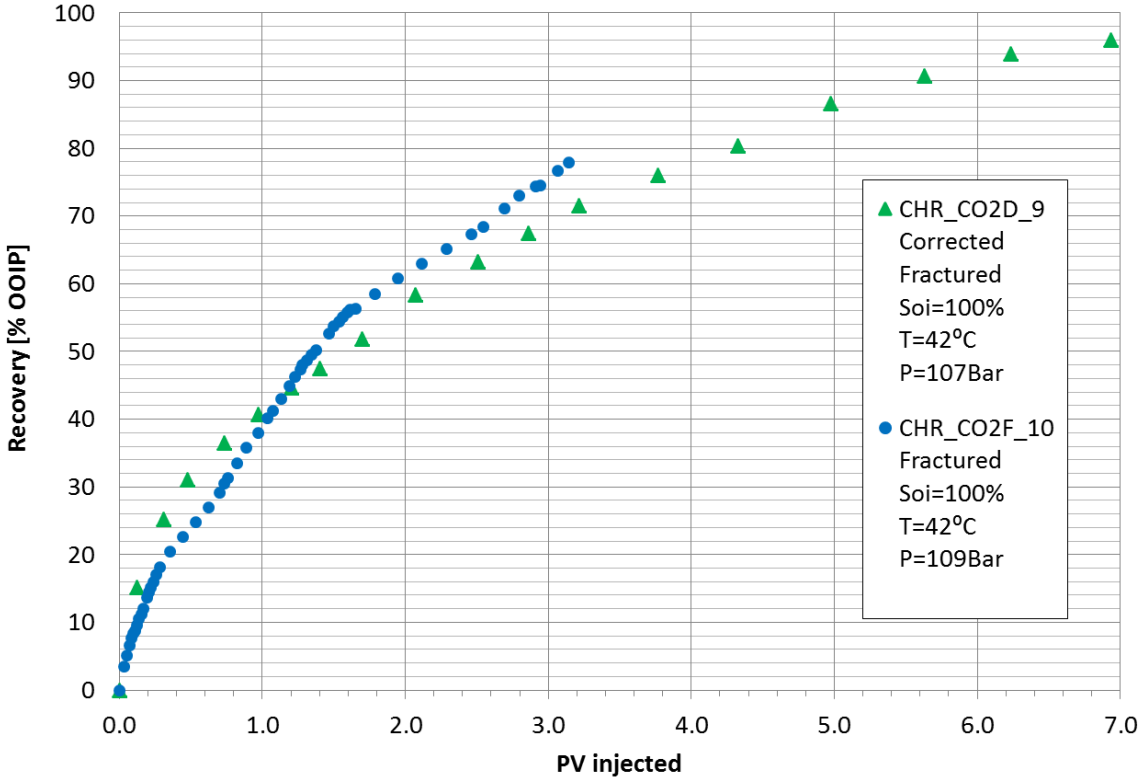

Figure 6.38: Calculated oil recovery from material balance as a function of time for both the CO_2 injection and the CO_2 foam injection. The CO_2 foam injection seem to have a higher oil production rate, but not as efficient as expected.

6.6 Liquid CO_2 injection labeled with ^{11}C visualized in PET/CT

Several experiments involving ^{11}C as a nuclear tracer in the CO_2 phase was conducted at Haukeland University Hospital. One experiment involving liquid CO_2 injection into fractured sandstone is presented in this thesis. Information about the PET/CT scanner process is briefly explained in section 4.2. The experimental procedure is explained in section 5.6. A material balance calculation could not be obtained in this experiment to avoid contamination of radioactive ^{11}C. Liquid CO_2 was injected into a 100% oil saturated core at a rate of 9 ml/h for 2 days. The objective was to investigate if CO_2, doped with the radioactive tracer ^{11}C, could be used to visualize the diffusion process from the fracture to the matrix.

Figure 6.39 displays the dry CT scan of the core, consisting of 273 images. The voxel sizes of the CT image is 0.28 mm * 0.28 mm * 0.6 mm in x-, y- and z direction, respectively. The images from PET scans has lower resolution, as explained in section 4.2, with voxel sizes 2 mm * 2 mm * 0.6 mm.

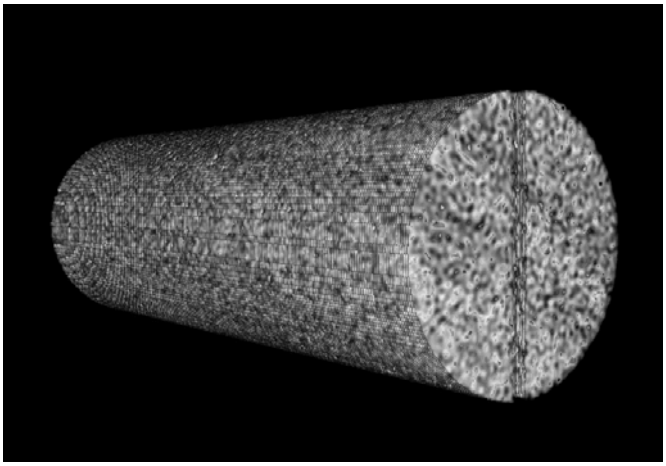

Figure 6.39: Dry CT scan of the 2" Bentheimer sandstone core used in the PET/CT experiment.

Two separate PET cycles was conducted during the experiment. Detected radiation decreases rapidly, caused by the fast disintegration of ^{11}C. The PET scanner takes this into account as it calculates the same delivered signal despite the declining radiation from ^{11}C. The first PET cycle was conducted at the start of the experiment and the second was conducted 12 hours into the injection test. Obtained images were digitally sliced as shown in **Figure 6.6** and **Figure 6.9**, to visualize the movement of CO_2 within the core during the test.

Figure 6.40 displays the signal from the first PET cycle conducted, vertically sliced perpendicular to the fracture plane in the middle of the core (X_L = 0.5). The radiation of ^{11}C was approximately 3 GBq at delivery from the hot cell. The dry CT image is showed slightly transparent in the background to indicate the boundaries of the core. An injection rate of 60 ml/h was kept at the start of the experiment. Because of an unfavorable mobility ratio between CO_2 and oil a finger developed in the top of the fracture and immediately displaced oil in this area. At the experimental conditions (P = 83 bar, T = 25 °C) the CO_2 is slightly denser than n-decane (see **Table 5.2**). Any gravitational support for the CO_2 should enhance the oil recovery by displacing oil in the lower parts of the fracture. In addition, the CO_2 would get a larger contact area with the oil for displacement by diffusion. However, the room temperature was not measured and could possibly been higher than 25 °C. If the temperature was higher the less dense CO_2 might support the observations of oil displacement in the top of the fracture caused by gravity override. Recovery of oil from the bottom of the core depends on CO_2 diffusion from the top part of the matrix and fracture.

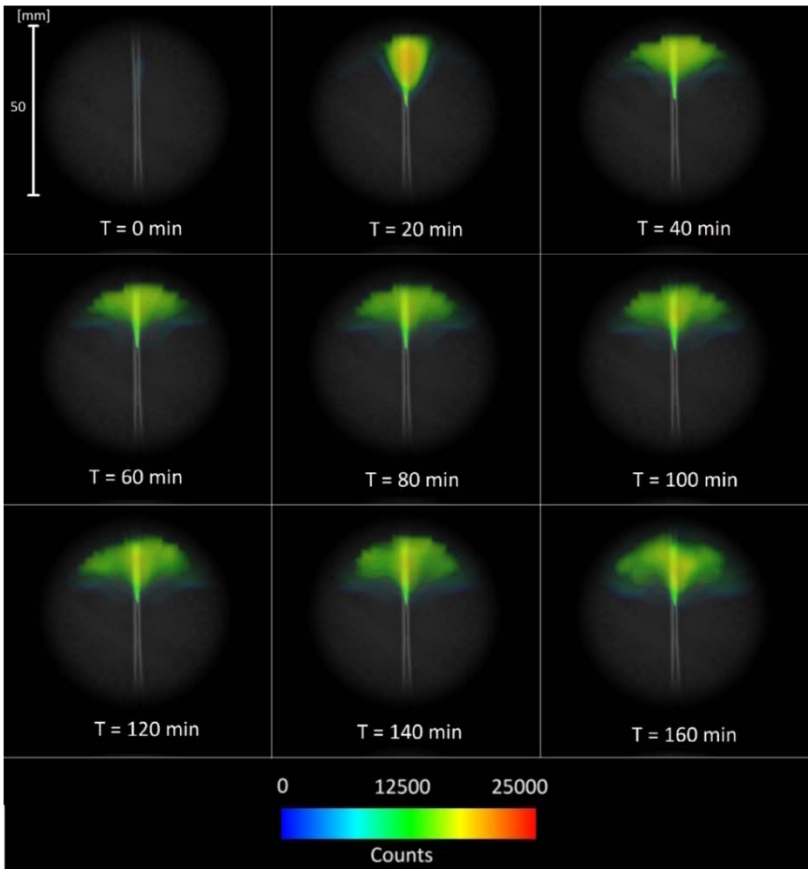

Figure 6.40: The first PET cycle showing injection of CO_2 labeled with ^{11}C in a 100% oil saturated fractured core at various time steps. The core is vertically sliced perpendicular to fracture plane in the middle of the core (X_L = 0.5). The dry scan of the core is made slightly transparent in the background (grey) to indicate the boundaries of the core in all images. The color specter indicated at the bottom is the detected PET signal from ^{11}C. Warm colors indicate high concentration of ^{11}C and cold colors indicate low ^{11}C concentration. The white line present in the first image indicates the length scale and is 50 mm long.

Figure 6.41 shows the second PET cycle. This time the PET scanner was set to measure signals for 5 hours to investigate how long the ^{11}C could give a satisfying signal during experiments. There was some operational problems with the cycltotron, resulting in less radioactive nucleus in the mixture of ^{11}C. It was measured to be approximately 1.3 GBq (compared to 3 GBq from the first PET cycle). However, the detected signals was enough to visualise CO_2. The images is showing a clean signal until about 160 minutes before the images starts to get blurry. Still, the ^{11}C seem to give a satisfying signal up to about 200 minutes.

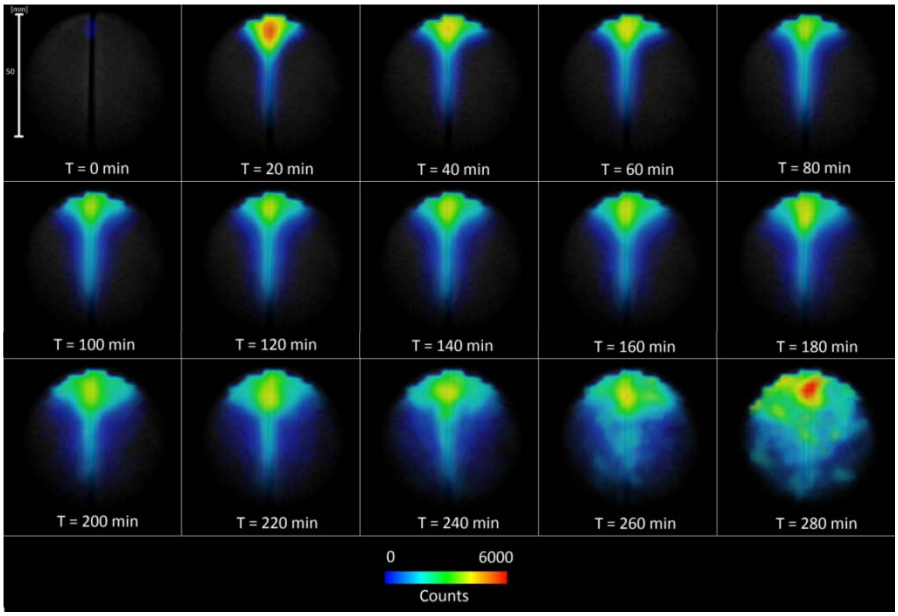

Figure 6.41: The second PET cycle showing injection of CO_2 labeled with ^{11}C in a 100% oil saturated fractured core at various time steps. The core is vertically sliced perpendicular to fracture plane in the middle of the core (X_L = 0.5). The dry scan of the core is made slightly transparent in the background (grey) to indicate the boundaries of the core in all images. The color specter indicated at the bottom is the detected PET signal from ^{11}C. Warm colors indicate high concentration of ^{11}C and cold colors indicate low ^{11}C concentration. The white line present in the first image indicates the length scale and is 50 mm long.

The second PET cycle differs from the first as CO_2 is visible further down the fracture of the core. Between the two cycles, CO_2 was injected into the core at a rate of 9 ml/h for 12 hours. CO_2 is slightly denser than n-decane at 83 bar and 25 °C coupled with mass transfer by vertical diffusion during this time period may explain this effect.

Figure 6.42 shows a horizontally sliced core perpendicular to fracture plane for both PET cycles. The core was sliced in image #5 from the top, to only observe oil recovery by CO_2 diffusion in the top part of the core. Much of the oil was already displaced before the second cycle was commenced. It was evident that oil recovery through diffusion was faster in the first PET cycle. Higher CO_2 saturation and less oil saturation in the top part of the core lead to a slower diffusion process in the second PET cycle and confirmed that the diffusion process is driven by concentration gradients.

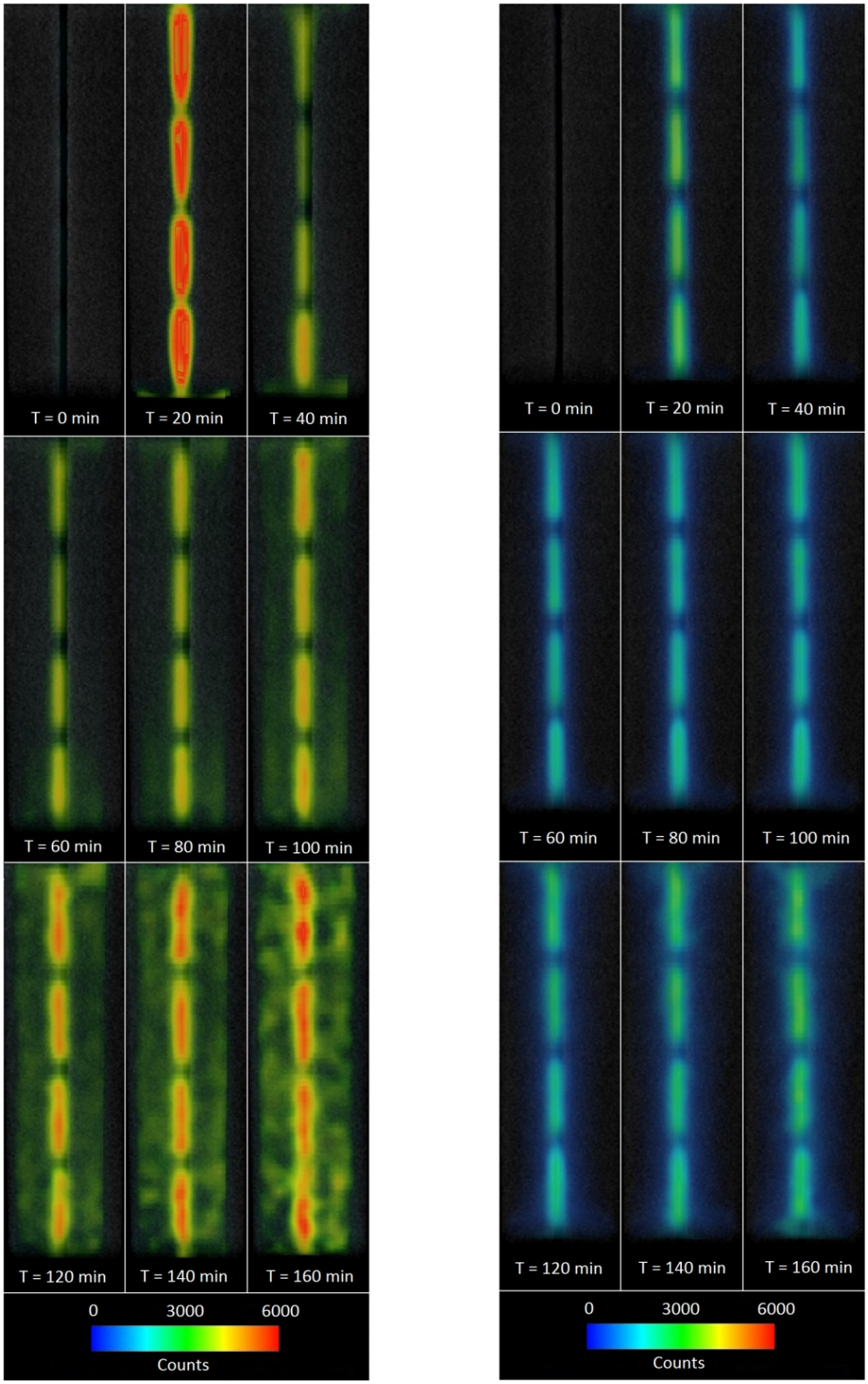

Figure 6.42: Injection of CO_2 labeled with ^{11}C for both PET cycles. The core is horizontally sliced perpendicular of the fracture plane in the top part of the core to investigate recovery by diffusion. The first PET cycle is on the left and the second PET cycle is on the right. It is evident that mass transfer of oil by the diffusion is higher in the first PET cycle because of higher concentration of oil present in the matrix. This validates that the diffusion process is driven by concentration gradients.

Figure 6.43 shows a picture of the core after the experiment was ended. Oil was only displaced in the top part of the core. This illustrates the main problem with the use of gas as the displacing fluid. Density and viscosity differences compared to oil generally leads to poor recovery caused by fingering and/or gravity override of injected fluid because of an unfavorable mobility ratio. On the other hand, the oil in top part is efficiently displaced by diffusion. This indicates that recovery by diffusion is efficient on short diffusion lengths where the gas is in contact with the oil.

Figure 6.43: Image of the core after ended experiment. The oil is displaced from the top of the core. Remaining oil in the bottom parts of the core was observed and supported the prediction of gravity override of CO_2 in the fracture during the injection test.

6.7 Supercritical CO_2 flooding in reservoir shale cores in CT

One experiment including CO_2 injection into two reservoir shale cores was conducted at Texas A&M University at College Station. Experimental setup is given in section 5.7. The experiment was designed to investigate if some crude oil could be recovered from reservoir shale cores by molecular diffusion. **Figure 6.44** shows oil production as a function of cumulative time for the shale experiment.

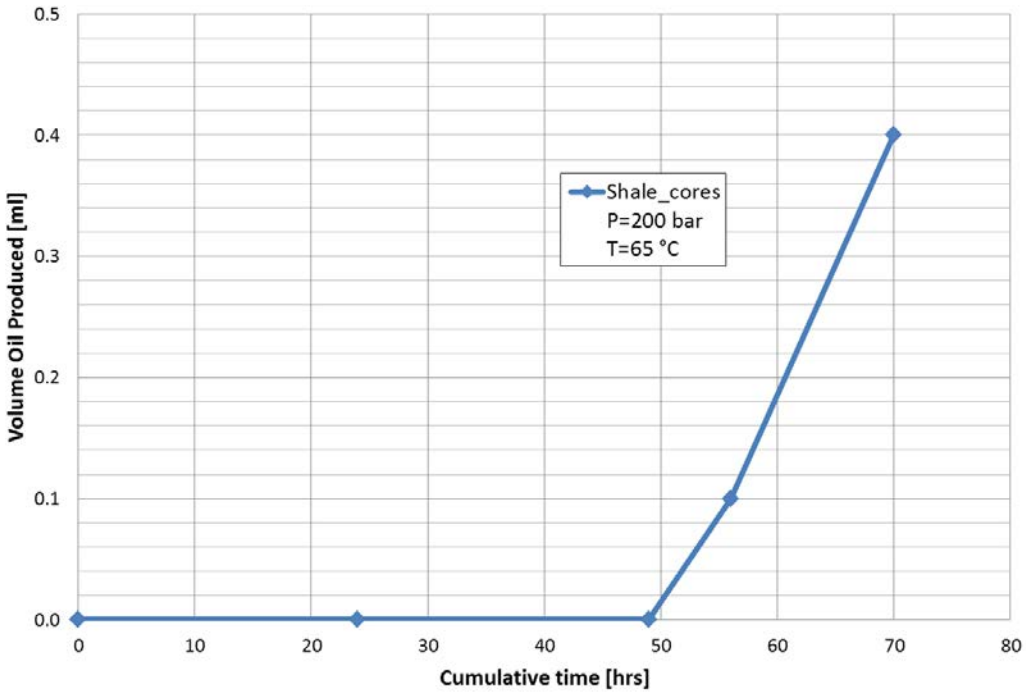

Figure 6.44: Oil production as a function of cumulative time for the two shale cores.

Unfortunately the difference in CT values between diffusive CO_2 and the crude oil within the core was too low to extract any definite information about changes in fluid saturations. To counter this, if possible, the experimental shale cores could be saturated with oil mixed with a dopant to enhance the difference in CT values. Fluid saturation calculation can then be performed to visualize the displacement. The recovery from the cores could not be calculated since the initial water and oil in place was unknown. However, educated guesses on oil recovery were performed considering two different scenarios. In a scenario with *high storage capacity*; 6 % porosity and 10% initial water saturation the recovery reach 20% OOIP. A scenario with *low storage capacity*; 3% porosity and 30% initial water saturation the recovery reach 51% OOIP.

6.8 Uncertainties related to experiments

Uncertainties related to CT imaging

Measurements and visualization with the use of a CT scanner are subject to a variety of errors and image artifacts including beam hardening, star-shaped artifacts, positioning errors and machine errors (Akin et al., 2003). These are briefly discussed. The majority of CT scanners were developed for medical purposes and were not intended for quantitative imaging and analysis. Most of the soft X-rays are absorbed in the air and at the interface of the sample leaving remaining high energy photons that are measured by the scanner. Thus, the X-ray spectrum attenuates towards the lower energy portions of the spectrum which introduces an error in the linear attenuation measurement called beam hardening; adding dark bands around the periphery of the scanned object. Artifacts originate from the image reconstruction and are caused by scattering of photons that interferes with the matter in the object. The extend of artifacts increases with scanned volume or slice width.

Positioning errors can occur during the process of image subtraction to obtain saturations and porosity. To avoid these errors the position of the scanned core within subtracted images must be constant. Thereby it is important to avoid any movement of the core holder between scans. For example, in the PET/CT experiment, the core holder was moved between the 100% saturated scans since the core had to be saturated with oil in a separate lab than the PET/CT scanner room. The original place of the core holder in the PET/CT scanner was marked with a pen which resulted in some uncertainty. For more information about errors related to CT scanning see (Akin et al., 2003).

Uncertainties related to all experiments

Uncertainties related to experimental work conducted in this thesis can be divided into two categories; Experimental uncertainties and equipment uncertainties. Each step in the preparation and conduction of experiments has an associated uncertainty that contribute to the total uncertainty of the experiment.

Experimental uncertainties include thermal variances, system leaks and errors in measurements and readings during the experiment. Small fluctuations in temperature affect the system pressure significantly as can be recognized from the CO_2 injection experiment. To minimize temperature variances at UoB the heating cabinet door was kept closed during the whole experiment except when turning valves. System leaks often occur during experiments. Two experiments were aborted because of leaks. Fixing leaks is time consuming and are often associated with large enough uncertainty to abort the experiment.

All the equipment used in the experiments, such as calipers, pumps and weights has an associated uncertainty. The calipers have an uncertainty of ±0.01 mm. Uncertainty in injection rate of pumps is ±5 % and pressure gauge readings is ±2%. Equations for calculating uncertainty for porosity, permeability and bulk volume of cores and pore volume based on these error values are presented in appendix A.

Figure 6.45 displays the reduction in oil saturation as a function of PV injected for one of the supercritical CO_2 injections (CHR_CO2D_2) including error bars. Uncertainties regarding the recovery include error in calculated total pore volume of the core after fracturing and error in production readings from the cylinder and via web camera resulting from the sight angle. Uncertainties regarding pore volume of CO_2 injected include error in injection rate from the pumps and measurements of dead volume. The two last mentioned errors contribute to the largest uncertainty in the experiments conducted in this thesis.

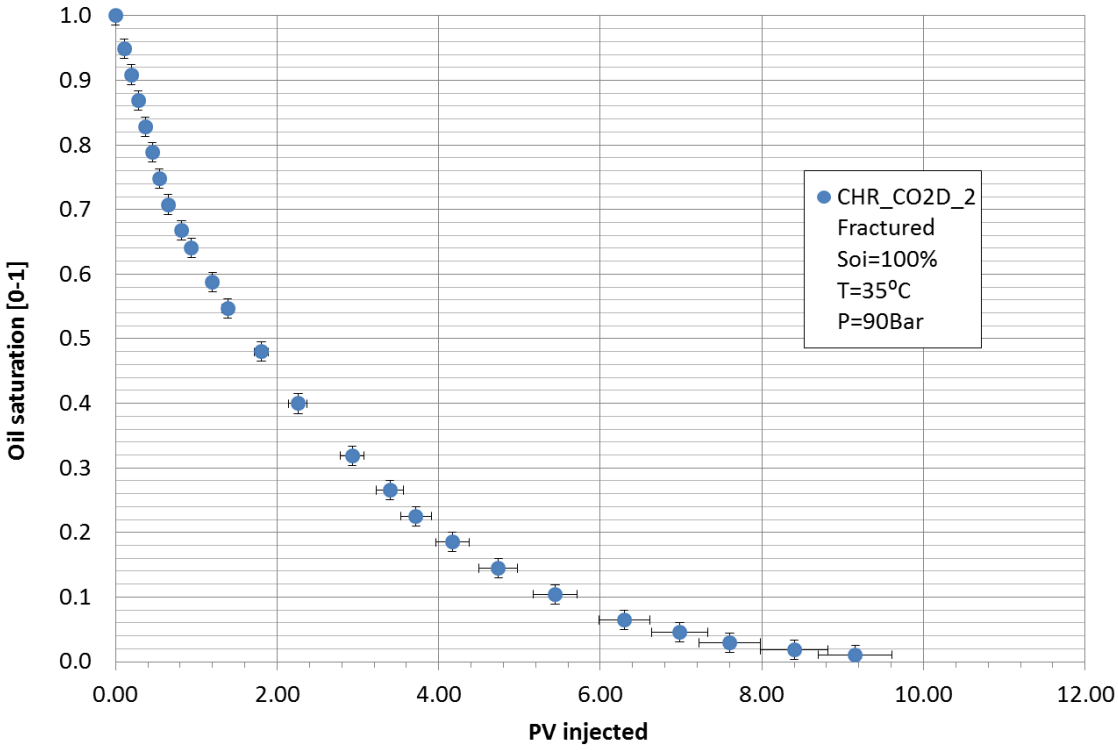

Figure 6.45: Reduction in oil saturation as a function of PV CO_2 injected for CHR_CO2D_2 including error bars.

7 Conclusions

- Oil recoveries ranging between 95-98% OOIP was achieved during miscible CO_2 injection tests in fractured chalk cores with a highly conductive fracture with molecular diffusion as the only recovery mechanism. Final recovery was not affected by the presence of irreducible water saturation, but was less efficient as a larger amount of injected CO_2 was needed to obtain the same recovery.

- The high recoveries required large quantities of injected CO_2 because diffusion rate is a slow process influenced by length and time. In a field application, injecting several pore volumes of CO_2 is not feasible. However recoveries reached 55-60% of OOIP with less than 2 PV of CO_2 injected, and 75-85% of OOIP after 4 PV of CO_2 injected.

- It was observed that without the presence of a fracture, less PV of CO_2 were needed to reach high oil recovery resulting from both viscous and diffusive recovery mechanisms.

- Reduction in oil saturation in supercritical CO_2 injections performed at 90 bar and 35 °C was compared with the experiment performed at 107 bar and 42 °C. The graphs showed similarity with no significant discrepancy. More injection tests should be conducted to draw a definite conclusion on this matter.

- Data obtained from the CT-scanner was used to calculate CO_2 saturations during the experiment based on the spatial CO_2 distribution in the matrix. The images acquired, together with the absence of a differential pressure across the core plug, confirmed that the main oil recovery from the matrix was by molecular diffusion.

- The effective molecular diffusion coefficient was calculated for a miscible CO_2 injection test in a fractured, 100% oil saturated Rørdal chalk core (water-wet) at 107 bar and 42 °C. It was estimated to $D_e = 1.66*10^{-9} \pm 7.2*10^{-10}$ m^2/s from calculated concentration profiles based on a graphical method with the use of Fick's second law of diffusion. This value can be used as an input parameter in further simulations of miscible CO_2 injections at similar conditions.

- Gravity segregation was observed during several experiments because of density differences between CO_2 and n-decane. A build-up of CO_2 concentration was increasing in the top of the fracture and in the matrix as time commenced. This effect was particularly evident in the experiment conducted in the CT/PET scanner at Haukeland where injected CO_2 was labeled with a radioactive tracer.

- Introduction of pre-generated CO_2-foam did not have a significant impact on oil recovery as the foam was destroyed at the inlet of the core resulting from experimental conditions explained in section 6.5.1 (no irreducible water saturation present).

- Numerical simulations have been performed with CMG GEM simulator and matched with the CO_2 visualization experiment with oil recovery by diffusion. The simulations satisfactorily reproduced experimental data under the assumption that the experimental supercritical CO_2 and the simulated liquid CO_2 act in the same matter with n-decane.

- An effective molecular diffusion coefficient of $D_e = 3.02*10^{-9}$ m^2/s was estimated based on fitting oil production graphs from the numerical simulation with experimental data under the previous mentioned assumption.

- A sensitivity parameter study was conducted with known parameters that influence oil recovery by diffusion. The numerical model was not sensitive with permeability variation ranging from 1 nD to 1D. The CO_2 diffusion process was, however, strongly influenced by changes in porosity and the diffusion coefficient.

- The numerical model confirmed that no oil was recovered from the matrix without miscible conditions between the oil present in the matrix and the CO_2 present in the fracture.

- Diffusion of CO_2 into the matrix from the fracture was successfully visualized by doping the injected CO_2 with radioactive ^{11}C, but there are limitations regarding the short lifespan of the tracer. If CO_2 concentrations shall be estimated, the oil phase should be doped with 1-iododecane to enhance the difference in CT-values.

- Oil production from supercritical CO_2 injection into reservoir shale cores from an oil field was observed. Recoveries were calculated based on assuming different scenarios and recoveries ranged from 20% to 51% of OOIP. If possible, the oil phase should be doped in future experiments to enhance the difference in CT-values to observe changes in the spatial CO_2 distribution in the matrix.

8 Future work

- The high quality CT data acquired from the CO_2 injection experiment can be used in further investigations. The diffusion process takes place from the inlet, outlet and the fracture. The data could be used to estimate diffusion coefficient from the inlet and outlet of the core and compare the results.

- The data sets available can be used to obtain a CO_2 concentration plot in the upper and lower parts of the core as a function of time during the CO_2 injection to observe the advancement rate of the gravity segregation taking place in the matrix and in the fracture.

- A similar experiment to the supercritical CO_2 injection could be applied with a vertical alignment, to compare the results and see if the diffusion coefficient is higher than for horizontal alignment which would be in agreement with Renner (Renner, 1988).

- The supercritical CO_2 injection test visualized in CT was run for a total of 6 days. The diffusion coefficient found in this thesis was based on the first 5 hours of CO_2 injection test. This means that several parameters could be investigated in a relatively short amount of time. Parameters that could be altered and investigated in future experiments:
    - Presence of irreducible water saturation
    - Alteration of wettability
    - Different experimental pressure and temperature
    - Different injection rates
    - Tertiary CO_2 flooding
    - CO_2-foam injection with irreducible water present

- The numerical model designed to observe oil recovery in the matrix from a fracture can be used for further investigations:
    - Include resistivity which includes tortuosity, porosity and cementation factor directly in the simulation by adding the RESISTIVITY keyword to compare the diffusion coefficient with results from this thesis.
    - Include oil swelling.
    - Observe the impact on oil recovery rates at varying width and length of the matrix block.
    - Observe the impact on oil recovery with irreducible water saturation present in the matrix.
    - Alteration of wettability

- Change parameters in the numerical simulation to achieve supercritical conditions of the CO_2 phase to compare with experimental results and also with simulated liquid conditions from this thesis.

- Further develop the numerical simulation model to observe the impact on oil recovery by diffusion in more complex scenarios and possibly on field scale.

9 Nomenclature

EOR	Enhanced Oil Recovery
NCS	Norwegian Continental Shelf
CCS	Carbon capture and sequestration
CCUS	Carbon capture, utilization and sequestration
MMP	Minimum miscibility pressure
PET	Positron Emission Tomography
CT	Computed Tomography
CT_{scan}	CT values obtained for different fluids during CO_2 injection
CT_{CO2}	100% CO_2 scan
CT_{Oil}	100% oil scan
PV	Pore volume of fractured core
R_f	Recovery factor
μ_a,	Linear attenuation for material *a*
I_0	Intensity of the incident beam
I	Intensity after passing through the material
X	Material thickness
Q	Fluid flow rate
μ	Fluid viscosity
A	Cross sectional area of the core sample
L	Sample length
Δp	Differential pressure across the core sample
K	Absolute permeability
$k_{r,i}$	Relative permeability of a fluid *i* (oil, gas or water)
$K_{e,i}$	Effective permeability of a fluid *i* (oil, gas or water)
S_i	Fluid saturation of a fluid
S_{iw}	Irreducible water saturation
V_p	Pore volume
V_t	Total core volume
D_e	The effective diffusion coefficient
D_a	The absolute diffusion coefficient
ϕ	Porosity
m	Cementation factor
σ	Interfacial tension
M	Mobility ratio

10 References

ABRISHAMI, Y., LINDA, U. & HATAMIAN, H. 1996. Phase Behaviour of Fluids in Multiple Contact Processes with CO2, N2 and their Mixture. *Abu Dhabi International Petroleum Exhibition and Conference.* Abu Dhabi, United Arab Society of Petroleum Engineers

AHMED, A. 2013. *En eksperimentell studie av CO_2 injeksjon for økt oljeutvinning i oppsprukket kalk.* Msc., Universitetet i Bergen.

AHMED, A. B. B. N., R. 2012. A Selection Criterion for CO2-Enhanced Oil Recovery and Dispersion Modeling of High-Pressure CO2 Release. *SPE Western Regional Meeting.* Bakersfield, California, USA: Society of Petroleum Engineers.

AHMED, T. H. M. T. 1994. Prediction of CO2 Minimum Miscibility Pressures. *SPE Latin America/Caribbean Petroleum Engineering Conference.* Buenos Aires, Argentina.

AKBAR, M., VISSAPRAGADA, B., ALGHAMDI, A.H., AND ALLEM, D. 2000. A Snapshot of Carbonate Reservoir Evaluation. *Oilfield Review,* 12**,** 20-21.

AKIN, S., A.R., K., MEES, F., SWENNEN, R., VAN GEET, M. & JACOBS, P. 2003. Computed Tomography in Petroleum Engineering Research. *Applications of X-ray Computed Tomography in the Geosciences,* Geological Society**,** 23-38.

AKIN, S., KOVSCEK, A.R. 1999. Imbibition Studies of Low-Permeability Porous Media. *SPE Western Regional Meeting.* Anchorage, Alaska: Society of Petroleum Engineers.

ALAM, M. H., M.L., CHRISTENSEN, H. F. & FABRICIUS, I. L. 2011. Impact of Supercritical CO_2 Injection on Petrophysical and Rock Mechanics Properties of Chalk: An Experimental Study on Chalk from South Arne Field, North Sea. *SPE Annual Technical Conference and Exhibition.* Denver, Colorado, USA.

ALAVIAN, S. A. & WHITSON, C. H. 2012. Modeling CO2 Injection Including Diffusion in a Fractured-Chalk Experiment with Initial Water Saturation. *Carbon Management Technology Conference.* Orlando, Florida, USA: Carbon Management Technology Conference.

ALLAN, J. Q. S., S. C&C RESERVOIRS, INC. 2003. Controls on Recovery Factor in Fractured Reservoirs: Lessons Learned from 100 Fractured Fields. *SPE Annual Technical Conference and Exhibition.* Denver, Colorado: Society of Petroleum Engineers.

ALVARADO, V. A. M., E. 2010. Enhanced Oil Recovery: An Update Review. *Energies,* 3**,** 1529-1575.

AMAO, A., SIDDIQUI, S., MENOUAR, H. & HERD, B. L. 2012. A New Look at the Minimum Miscibility Pressure (MMP) Determination from Slimtube Measurements. *SPE Improved Oil Recovery Symposium.* Tulsa, Oklahoma: Society of Petroleum Engineers

AUSTAD, T. 2008. Seawater in Chalk An EOR and Compaction Fluid. *The 42nd U.S. Rock Mechanics Symposium (USRMS).* San Francisco, CA.

AWAN, A. R., TEIGLAND, R. & KLEPPE, J. 2006. EOR Survey in the North Sea. *Symposium on Improved Oil Recovery.* Tulsa, Oklahoma, USA.

AYIRALA, S. C., RAO, D.N. , LOUISIANA STATE U. 2006. Comparative Evaluation of a New MMP Determination Technique. *SPE/DOE Symposium on Improved Oil Recovery.* Tulsa, Oklahoma, USA: Society of Petroleum Engineers

BAILEY, D. L., D.W. TOWNSEND ,PETER E VALK , MICHAEL N MAISEY 2006. *Positron Emission Tomography: Basic Sciences,* Hardcover.

BARRUFET, M. A., SAID EL-SAYED K., TANTAWY S. M., GUSTAVO A. IGLESIAS-SILVA 1996. Liquid Viscosities of Carbon Dioxide + Hydrocarbons from 310 K to 403 K''. *Journal of Chemical and Engineering Data,* 41.

BEER, A. 1852. Bestimmung der Absorption des rothen Lichts in farbigen Flüssigkeiten. *Annal. Phys. Chem. 86***,** 78-88.

BIRD, R. B. S., W.E E.N. LIGHTFOOT 1976. *Transport Phenomena,* New York.

BLUNT, M. J., FAYERS, F.J., ORR, F.M. 1993. Carbon dioxide in enhanced oil recovery. *Energy Conversion and Management,* 34**,** 1197-1204.

BROCK, W. R. & BRYAN, L. A. E. C. U. S. A. 1989. Summary Results of CO2 EOR Field Tests, 1972-1987. *Low Permeability Reservoirs Symposium.* Denver, Colorado: Society of Petroleum Engineers

BUI, L. H. 2013. *Near-Miscible CO2 Application to Improve Oil Recovery.* MSc, University of Kansas.

CAMPBELL, B. T. N. M. P. R. R. C. F. M. O. J., NEW MEXICO INST. OF MINING AND TECHNOLOGY 1985. Flow Visualization for CO2/Crude-Oil Displacements. *SPE Journal,* Volume 25, Number 5**,** 665-678.

CHANG, Y.-B., COATS, B. K. & NOLEN, J. S. 1998. A Compositional Model for CO2 Floods Including CO2 Solubility in Water. *SPE Reservoir Evaluation & Engineering,* 1**,** 155-160.

CHILLENGER, G. V. A. Y., T.F. 1983. Some Notes on Wettability and Relative Permeability of Carbonate Rocks II. *Energy and Sources,* 7**,** 67-75.

CHRISTIANSEN, R. L., MARATHON OIL CO.; HAINES, HIEMI KIM, MARATHON OIL CO. 1987. Rapid Measurement of Minimum Miscibility Pressure With the Rising-Bubble Apparatus *SPE Reservoir Engineering,* Volume 2, Number 4**,** 523-527.

CHRISTOPHERSEN, A. 2012. *Økt oljeutvinning ved injeksjon av CO2-skum i en oppsprukket karbonatbergart ved forskjellige fuktforhold.* MSc Master Thesis, University of Bergen.

COLES, M. E., MUEGGE E.L. , AUZERAIS F.M. , FRULLA, P. , KANTZAS, A. 1995. The Use of Attentuation Standards for CT Scanning. *SCA Conference Paper Number 9513.*

CUSSLER, E. 1997. *Diffusion: Mass Transfer in Fluid Systems*.

DA SILVA, F. V. B., P. 1989. Molecular Diffusion in Naturally Fractured Reservoirs: A Decisive Recovery Mechanism. *SPE Annual Technical Conference and Exhibition.* Society of Petroleum Engineers.

DARVISH, G. R. 2007. *Physical Effects Controlling Mass Transfer in Matrix Fracture System During CO2 Injection into Chalk Fractured Reservoirs.* PhD, NTNU.

DARVISH, G. R. S., SINTEF/NTNU; E. LINDEBERG, SPE, SINTEF; T. HOLT, SPE, RESLAB A/S; AND S.A. UTNE, SINTEF 2006. Reservoir Conditions Laboratory Experiments of CO2 Injection Into Fractured Cores. *SPE/DOE Symposium on Improved Oil Recovery, 22-26 April 2006.* Tulsa, Oklahoma, USA: Society of Petroleum Engineers

DAUTRIAT, J. S., N. GLAND, SPE, S. YOUSSEF, SPE, E. ROSENBERG, SPE, AND S. BEKRI, SPE, INSTITUT FRANÇAIS DU PÉTROLE 2007. Stress-Dependent Permeabilities of Sandstones and Carbonates: Compression Experiments and Pore Network Modelings. *SPE Annual Technical Conference and Exhibition.* Anaheim, California, U.S.A.: Society of Petroleum Engineers.

DE BOER, R. B., WELLINGTON. S.L , AND TSCHIEDEI. K.L. 1984. Measurements on CO2-Diffusion through Unusually Resistive Layers on Oil-Water Interfaces. *Colloids and Surfaces,* 9**,** 79-83.

DENOYELLE, L. A. B., C. 1983. Influence of diffusion on Enhanced Oil Recovery by CO, Injection. *Proc. IntI. Symposium CO_2, EOR.* Budapest.

DINDORUK, B. & FIROOZABADI, A. 1997. Crossflow in Fractured/Layered Media Incorporating Gravity, Viscous, and Phase Behavior Effects. *SPE Journal,* 2**,** 120-135.

EKDALE, A. A. B., R.G. 1993. Trace Fossils and Ichnofabric in the Kjolby Gaard Marl, Uppermost Cretaceous, Denmark. *Bull. Geol. Soc. Denmark,* 31**,** 107.

ELSHARKAWY, A. M., SUEZ CANAL U.; POETTMANN, F.H., CHRISTIANSEN, R.L., COLORADO SCHOOL OF MINES 1992. Measuring Minimum Miscibility Pressure: Slim-Tube or Rising-Bubble Method? *SPE/DOE Enhanced Oil Recovery Symposium.* Tulsa, Oklahoma.

ENICK, R. M. D. O. C. A. P. E., UNIV. OF PITTSBURGH; D. OLSEN, IBM GLOBAL BUSINESS SERVICES; J. AMMER, US DOE NATIONAL ENERGY TECHNOLOGY LABORATORY; W. SCHULLER, URS CORPORARION 2012. Mobility and Conformance Control for CO2 EOR via Thickeners, Foams,

and Gels -- A Literature Review of 40 Years of Research and Pilot Tests. *SPE Improved Oil Recovery Symposium.* Tulsa, Oklahoma, USA: Society of Petroleum Engineers

FALCONE, G. & HARRISON, R. 2013. Deciding Whether to Fund Either CCS or CCUS Offshore Projects: Are We Comparing Apples and Pears in the North Sea? *SPE Annual Technical Conference and Exhibition.* New Orleans, Louisiana, USA: 2013, Society of Petroleum Engineers.

FARAJZADEH, R., ANDRIANOV, A. & ZITHA, P. L. J. 2009. Foam Assisted Enhanced Oil Recovery at Miscible and Immiscible Conditions. *Kuwait International Petroleum Conference and Exhibition.* Kuwait City, Kuwait: Society of Petroleum Engineers.

FAROUQ, S. M. & THOMAS, S. 1989. The Promise And Problems Of Enhanced Oil Recovery Methods. *Technical Meeting / Petroleum Conference Of The South Saskatchewan Section.* Regina: Society of Petroleum Engineers.

FENG LI, R. W. Y., SPE, IPSI; SHUNHUA LIU, SPE, OCCIDENTAL OIL AND GAS; AND GEORGE J. HIRASAKI, SPE, AND CLARENCE A. MILLER, SPE, RICE UNIVERSITY 2010. Foam Mobility Control for Surfactant Enhanced Oil Recovery. *SPE Journal,* Volume 15, Number 4.

FERNØ, M. A. 2012. Enhanced Oil Recovery in Fractured Reservoirs, Introduction to Enhanced Oil Recovery (EOR) Processes and Bioremediation of Oil-Contaminated Sites.

FERNØ, M. A., HAUGEN, Å. & GRAUE, A. 2010. Visualizing Oil Displacement In Fractured Carbonate Rocks - Impacts On Oil Recovery At Different Hydrostatic Stress And Wettability Conditions. *In:* DEPT. OF PHYSICS AND TECHNOLOGY, U. O. B. (ed.) *44th U.S. Rock Mechanics Symposium and 5th U.S.-Canada Rock Mechanics Symposium.* Salt Lake City, Utah: American Rock Mechanics Association.

FIROOZABADI, A. 1994. Miscible Displacement in Fractured Porous Media: Part I--Experiments. *SPE/DOE Improved Oil Recovery Symposium.* Tulsa, Oklahoma: 1994 Copyright 1994, Society of Petroleum Engineers, Inc.

FIROOZABADI, A. 2000. Recovery mechanisms in fractured reservoirs and field performance. *Journal of Canadian Petroleum Technology,* 39**,** 13-17.

FIROOZABADI, A., CHENG, P. 2010. Prospects for subsurface CO2 sequestration. *AIChE Journal,* 56**,** 1398-1405.

FOLGER, L. K. G., S.N. TEXACO EXPLORATION AND PRODUCTION, INC. 1996. A Case Study of the Development of the Sundown Slaughter Unit CO2 Flood Hockley County, Texas. *Permian Basin Oil and Gas Recovery Conference.* Midland, Texas: Society of Petroleum Engineers

FRIED, J. J. A. C., M.A. 1971. Dispersion in porous media. *Adv. Hydrosci.,* 7**,** 169.

GARMEH, G., JOHNS, R. T. & LAKE, L. W. 2009. Pore-Scale Simulation of Dispersion in Porous Media. *SPE Journal,* 14**,** 559-567.

GCCSI. 2013. *Sleipner CO2 Injection* [Online]. Global CCS Institute. Available: http://www.globalccsinstitute.com/projects/12401 [Accessed 06.08 2013].

GHORAYEB, K. F., A. RESERVOIR ENGINEERING RESEARCH INSTITUTE 2001. Features of Convection and Diffusion in Porous Media for Binary Systems. *Journal of Canadian Petroleum Technology,* 40.

GLASO, O. 1990. Miscible Displacement Recovery Tests With Nitrogen. *SPE Reservoir Engineering,* 5**,** 61-68.

GOLABI, E., AZAD, F.S. AND BRANCH, O. 2012. Experimental Study of Wettability Alteration of Limestone Rock from Oil-Wet to Water-Wet using Various Surfactants. *SPE Heavy Oil Conference.* Calgary, Alberta, Canada: SPE157801.

GOZALPOUR, F., REN, S. R. & TOHIDI, B. 2005. CO2 EOR and Storage in Oil Reservoirs. Oil & Gas Science and Technology. *Oil & Gas Science and Technology,* 39**,** 591-602.

GRAUE, A. 2006. *PTEK214 "Experimental Reservoir Physics", Dept. of Physics and Technology, University of Bergen.*

GRAUE, A. & NESSE, K., U. OF BERGEN; B.A. BALDWIN, GREEN COUNTRY PETROPHYSICS; E.A. SPINLER, D.P. TOBOLA, PHILLIPS PETR. CO. 2002. Impact of Fracture Permeability on Oil Recovery in Moderately Water-Wet Fractured Chalk Reservoirs. *SPE/DOE Improved Oil Recovery Symposium.* Tulsa, Oklahoma: Society of Petroleum Engineers

GRAUE, A., VIKSUND, B. G. & BALDWIN, B. A. 1999. Reproducible Wettability Alteration of Low-Permeable Outcrop Chalk *SPE Reservoir Evaluation & Engineering,* Volume 2, Number 2**,** 134-140.

GREEN, D. W., WILLHITE, G.P. (1998). : 1998. Enhanced oil recovery, Richardson.

GROGAN, A. T., PINCZEWSKI, V. W., RUSKAUFF, G. J. & ORR JR., F. M. 1988. Diffusion of CO2 at Reservoir Conditions: Models and Measurements. *SPE Reservoir Engineering,* 3**,** 93-102.

GROGAN, A. T., U. OF NEW SOUTH WALES; PINCZEWSKI, W.V., U. OF NEW SOUTH WALES 1987. The Role of Molecular Diffusion Processes in Tertiary CO2 Flooding *Journal of Petroleum Technology,* Volume 39, Number 5**,** 591-602.

HAIFENG JIANG, E., LILY NURYANINGSIH, HERTANTO ADIDHARMA, UNIVERSITY OF WYOMING 2012. The Influence of O2 Contamination on MMP and Core Flood Performance in Miscible and Immiscible CO2 WAG *SPE Improved Oil Recovery Symposium.* Tulsa, Oklahoma, USA.

HAUGEN, K. B. S., AND A. FIROOZABADI, SPE, YALE U. 2006. Measuring Molecular and Thermal Diffusion Coeffi cients in Multicomponent Mixtures by the Beam Deflection Technique. *SPE Annual Technical Conference and Exhibition.* San Antonio, Texas, USA Society of Petroleum Engineers.

HAUGEN, M. 2012. *CO_2 Injection in Fractured Chalk For Enhanced Oil Recovery.* MSc Master thesis, University of Bergen.

HAUGEN, Å., FERNØ, M. A., GRAUE, A. & BERTIN, H. J. 2012. Experimental Study of Foam Flow in Fractured Oil-Wet Limestone for Enhanced Oil Recovery. *SPE Reservoir Evaluation & Engineering,* Volume 15, Number 2**,** 218-228.

HEDEGAARD, K. G., A. , UNIVERSITY OF BERGEN, BERGEN, NORWAY 2011. Does Wettability Affect the Strength of Chalk? *45th U.S. Rock Mechanics / Geomechanics Symposium, June 26 - 29, 2011*.

HENRY, J. D., ATLANTIC RICHFIELD CO. 1977. The Effect of Oil Price Policy on Tertiary Oil Recovery. *SPE Economics and Evaluation Symposium.* Dallas, Texas: Society of Petroleum Engineers.

HJULER, M. L. 2007. *Diagenesis of Upper Cretaceous onshore and offshore chalk from the North Sea area.* Technical University of Denmark.

HOLM, L. W. J., V.A. 1974. Mechanisms of Oil Displacement By Carbon Dioxide *Journal of Petroleum Technology,* Volume 26, Number 12**,** 1427-1438.

HOLTZ, M. H. P. 2009. Geologic CO2 Storage in Oil Fields: Considerations for Successful Sites. *SPE International Conference on CO2 Capture, Storage, and Utilization.* San Diego, California: Society of Petroleum Engineers.

HOWES, B. J., AMOCO CANADA PETROLEUM COMPANY LTD. 1988. Enhanced Oil Recovery In Canada: Success In Progress. *Journal of Canadian Petroleum Technology,* 27.

IGLAUER, S. 2011a. Carbon capture and storage with a focus on capillary trapping as a mechanism to store carbon dioxide in geological porous media. *Advances in Multiphase Flow and Heat Transfer,* Volume 3, Chapter 4**,** 177-197.

IGLAUER, S. 2011b. Dissolution Trapping of Carbon Dioxide in Reservoir Formation Brine – A Carbon Storage Mechanism. *Mass Transfer - Advanced Aspects, Dr. Hironori Nakajima (Ed.), ISBN: 978-953-307-636-2, InTech*.

ISLAS-JUAREZ, R., INSTITUTO MEXICANO DEL PETROLEO; F. SAMANEGO V., UNAM; E. LUNA, C. PEREZ-ROSALES, J. CRUZ, INSTITUTO MEXICANO DEL PETROLEO 2004a. Experimental Study of Effective Diffusion in Porous Media. *SPE International Petroleum Conference in Mexico.* Puebla Pue., Mexico: Society of Petroleum Engineers

ISLAS-JUAREZ, R. I. M. D. P. F. S. V., UNAM; E. LUNA, C. PEREZ-ROSALES, J. CRUZ, INSTITUTO MEXICANO DEL PETROLEO 2004b. Experimental Study of Effective Diffusion in Porous Media. *SPE International Petroleum Conference in Mexico.* Puebla Pue., Mexico: Society of Petroleum Engineers

J.S. ARONOFSKY, H. J. R. J. 1956. Mobility Ratio – Its Influence on Injection or Production Histories in Five-Spot Water Flood *Journal of Petroleum Technology,* Volume 8, Number 9**,** 205-210.

JAHEDIESFANJANI, H. C., F. 2006. Improving Performance of the Naturally Fractured Carbonate Reservoirs by Means of the Various Stimulation and Completion Techniques. *First International Oil Conference and Exhibition in Mexico.* Cancun: Society of Petroleum Engineers

JOHANNESEN, B. E. 2008. *Wettability Determined by NMR and its Impacts on Oil Recovery in Chalk.* PhD, University of Bergen.

KARIMAIE, H., DARVISH, G. R., LINDEBERG, E. & TORSÆTER, O. 2007. Experimental Investigation of Secondary and Tertiary Gas Injection In Fractured Carbonate rock. *EUROPEC/EAGE Conference and Exhibition.* London, U.K.: Society of Petroleum Engineers.

KATZ, M. L. 1980. Outlook For Enchanced Recovery Operations In The 80's. *Annual Meeting Papers, Divison of Production.* Dallas, Texas.

KETCHAM, R. A. C., W. D 2001. Acquisition, optimization and interpretation of X-ray computed tomographic imagery: applications to the geosciences. 381-400.

KHATIB, Z. I., HIRASAKI, G. J. & FALLS, A. H. 1988. Effects of Capillary Pressure on Coalescence and Phase Mobilities in Foams Flowing Through Porous Media. *SPE Reservoir Engineering,* 3**,** 919-926.

KOCH, D. L. A. B., J.F. 1985. Dispersion in fixed beds. *Fluid Mech. ,* 154**,** 399.

KOVSCEK, A. R. R., C. J. 1993. *Fundamentals of Foam Transport in Porous Media, in Foams in the Petroleum Industry,* Washington D.C.

L.W. HOLM, U. C. 1986. Miscibility and Miscible Displacement. *Journal of Petroleum Technology,* Volume 38, Number 8**,** 817-818.

LAFORCE, T., IMPERIAL COLLEGE LONDON, AND FRANKLIN M. ORR, JR., STANFORD UNIVERSITY 2008. Development of Gas/Oil Miscibility in Water and Gas Injection. *SPE Annual Technical Conference and Exhibition.* Denver, Colorado, USA: Society of Petroleum Engineers.

LAKE, L. W. 1989. Enhanced Oil Recovery. *Prentice Hall Incorporated*.

LAMBERT, M. R., MARINO, S. D., ANTHONY, T. L., CALVIN, M. W., GUTIERREZ, S. & SMITH, D. P. 1996. Implementing CO2 Floods: No More Delays! *Permian Basin Oil and Gas Recovery Conference.* Midland, Texas: Society of Petroleum Engineers.

LENNTECH. 2009. *Carbon dioxide* [Online]. Available: http://www.lenntech.com/carbon-dioxide.htm [Accessed 12.08 2013].

LESCURE, B. M. & CLARIDGE, E. L. 1986. CO2 Foam Flooding Performance vs. Rock Wettability. *SPE Annual Technical Conference and Exhibition.* New Orleans, Louisiana: 1986 Copyright 1986, Society of Petroleum Engineers.

LIEN, J. R. 2004. Grunnleggende reservoarfysikk. *PTEK211, Universitetet i Bergen*.

LIN, E. C., HUANG, EDWARD T.S., UNOCAL CORP. 1990. The Effect of Rock Wettability on Water Blocking During Miscible Displacement *SPE Reservoir Engineering,* Volume 5, Number 2**,** 205-212.

LINDEBERG, E. & HOLT, T. 1994. EOR by Miscible CO2 Injection in the North Sea. *SPE/DOE Improved Oil Recovery Symposium.* Tulsa, Oklahoma: 1994 Copyright 1994, Society of Petroleum Engineers, Inc.

LOPEZ, V. N. 2012. *Enhanced Oil Recovery (EOR): Basic Concepts and U.S. Industry Experience* [Online]. Porto Alegre Brazil. Available: http://www.pucrs.br/cepac/download/1ccac/10_Recuperacao_Avancada_Petroleo_CCS_-_Vanessa_Nunez.pdf [Accessed 11.09.13.

LUO, H. K., A. 2008. Investigation of Diffusion Coefficients of Heavy Oil and Hydrocarbon Solvent Systems in Porous Media. *SPE/DOE Symposium on Improved Oil Recovery.* Tulsa, Oklahoma, USA.

MALIK, Q. M., ISLAM, M. R. & NULL 2000. Potential of Greenhouse Gas Storage and Utilization Through Enhanced Oil Recovery in Canada. World Petroleum Congress.

MANRIQUE, E. J. & MUCI, V. E. G., M.E. 2007. EOR Field Experiences in Carbonate Reservoirs in the United States. *SPE Reservoir Evaluation & Engineering,* 10**,** 667-686.

MATHIASSEN, T. 2013. *En eksperimentell studie av CO2 lagring i sedimentære bergarter ved bruk av ulike avbildningsteknikker.* MSc Master Thesis, University of Bergen.

MELZER, L. S. 2012. Carbon Dioxide Enhanced Oil Recovery (CO_2 EOR): Factors Involved in Adding Carbon Capture, Utilization and Storage (CCUS) to Enhanced Oil Recovery. *CO_2 Consultant and Annual CO_2 Flooding Conference Director.* Midland, Texas.

METWALLY, Y., UNIVERSITY OF HOUSTON; EVGENY M.CHESNOKOV, UNIVERSITY OF HOUSTON 2010. Measuring Gas Shale Permeability Tensor In the Lab Scale. *2010 SEG Annual Meeting.* Denver, Colorado: Society of Exploration Geophysicists.

MILLER, J. S. A. J., R. A. 1981. A laboratory study to determine physical characteristics of heavy oil after CO2 saturation. *SPE/DOE 9789.*

MORSI, K., LESLIE, J. & MACDONALD, D. 2004. CO2 Recovery and Utilization for EOR. *Abu Dhabi International Conference and Exhibition.* Abu Dhabi, United Arab Emirates: Society of Petroleum Engineers.

MRIDUL KUMAR, S., VIET HOANG, SPE, CENGIZ SATIK, SPE, CHEVRON ENERGY TECHNOLOGY CO.; AND DANNY ROJAS, SPE, STANFORD UNIVERSITY 2008. High-Mobility-Ratio Waterflood Performance Prediction: Challenges and New Insights. *SPE Reservoir Evaluation & Engineering,* Volume 11, Number 1**,** 186-196.

MULLER, T., BEB ERDGAS AND ERDOL GMBH; LAKE, LARRY W., U. OF TEXAS 1991. Theoretical Study of Water Blocking in Miscible Flooding. *SPE Reservoir Engineering,* Volume 6, Number 4**,** 445-451.

NETL, N. E. T. L. 2010. Carbon Dioxide Enhanced Oil Recovery - Untapped Domestic Energy Supply and Long Term Carbon Storage Solution.

NIST. 2013. *NIST Chemistry WebBook* [Online]. Standard Reference Data Act. . Available: http://webbook.nist.gov/ [Accessed 10.08 2013].

OFE, O. O. F. E. 2013. *Enhanced Oil Recovery* [Online]. Available: http://energy.gov/fe/science-innovation/oil-gas/enhanced-oil-recovery [Accessed 04.08 2013].

OLAOLUWA O. ADEPOJU, A. L. W. L., SPE, THE UNIVERSITY OF TEXAS AT AUSTIN, AND RUSSELL T. JOHNS, SPE, THE PENNSYLVANIA STATE UNIVERSITY 2013. Investigation of Anisotropic Mixing in Miscible Displacements. *SPE Reservoir Evaluation & Engineering,* Volume 16, Number 1**,** 85-96.

OLSEN, C. 2007. *Elastic and electric properties of North Sea Chalk.* PhD, Technical University of Denmark.

OYEKUNLE, A. A. S., TOTAL E&P NIGERIA 2013. Implications of U.S. and Europe Shale Gas on the Nigerian Gas Market. *Nigeria Annual International Conference and Exhibition.* Lagos, Nigeria: Society of Petroleum Engineers.

PATEL, P. D., SHELL DEVELOPMENT CO.; CHRISTMAN, P.G., SHELL DEVELOPMENT CO.; GARDNER, J.W., SHELL DEVELOPMENT CO. 1987. Investigation of Unexpectedly Low Field-Observed Fluid Mobilities During Some CO2 Tertiary Floods *SPE Reservoir Engineering,* Volume 2, Number 4**,** 507-513.

PERKINS, T. K., JOHNSTON, O.C., THE ATLANTIC REFINING CO. 1963. A Review of Diffusion and Dispersion in Porous Media. *SPE Journal,* Volume 3, Number 1**,** 70-84.

PICHA, M. S., SPE, RELIANCE INDUSTRIES LTD. 2007. ENHANCED OIL RECOVERY BY HOT CO2 FLOODING. *SPE Middle East Oil and Gas Show and Conference.* Kingdom of Bahrain.

PITTAWAY, K. R. R., E.E. CONOCO INC. 1990. The Ford Geraldine Unit CO2 Flood: Operating History. *SPE Production Engineering,* 5**,** 333-337.

POLLACK, N. R., ENICK, R. M., MANGONE, D. J. & MORSI, B. I. 1988. Effect of an Aqueous Phase on CO2/Tetradecane and CO2/Maljamar-Crude-Oil Systems. *SPE Reservoir Engineering,* 3**,** 533-541.

POMEROY, R. D. L., W.N. , SCUDDER, N.F. STAPP, F.P. 1933. Rate of solution of methane in quiescent liquid hydrocarbons. *Ind. Eng. Chem.,* 25**,** 1014-1019.

RAGE, T. 1996. *Studies of Tracer Dispersion and Fluid Flow in porous media.* PhD, University of Oslo.

RAMIREZ, W. F., U. OF COLORADO; SHULER, PATRICK J., CHEVRON OIL FIELD RESEARCH CO.; FRIEDMAN, FRANCOIS, CHEVRON OIL FIELD RESEARCH CO. 1980. Convection, Dispersion, and Adsorption of Surfactants in Porous Media *SPE Journal,* 20.

RAN, X., ZHAO, Y. & LIAO, X. 2012. An Assessment of a CO2 Flood for EOR and Sequestration Benefits in the Ordos Basin, Northwest China. *Carbon Management Technology Conference.* Orlando, Florida, USA.

RAO, D. N., LEE, J. I. 2000. Miscibility Evaluation for Terra Nova Offshore Field. *Canadian International Petroleum Conference.* Calgary, Alberta.

RENNER, T. A., AMOCO PRODUCTION 1988. Measurement and Correlation of Diffusion Coefficients for CO2 and Rich-Gas Applications. *SPE Reservoir Engineering,* 3**,** 517-523.

ROEHL, P. O. C., P.W. 1985. *Carbonate petroleum reservoirs*, Springer-Verlag.

ROSSEN, W. R. 1996. Foam in Enhanced Oil Recovery, in Foams - Theory Measurment and Applications.

ROSSEN, W. R., ZHOU, Z. H. & MAMUN, C. K. 1995. Modeling Foam Mobility in Porous Media. *SPE Advanced Technology Series,* 3**,** 146-153.

SAHIMI, M. 2011. *Flow and Transport in Porous Media and Fractured Rock*, WILEY.VCH Verlag GmbH & Co.

SELLEY, R. C. 1998. *Elements of Petroleum Geology.*

SHEIKHA, H., POOLADI-DARVISH, M. & MEHROTRA, A. K. 2006. An Inverse Solution Methodology for Estimating Diffusivity Coefficient of Gases in Bitumen from Pressure-Decay Data. *SPE Annual Technical Conference and Exhibition.* San Antonio, Texas, USA.

SHEN, F. S. L., EP TECH 2004. A Combined Geological, Geophysical and Rock Mechanics Approach to Naturally Fractured Reservoir Characterization and Its Applications. *SPE Annual Technical Conference and Exhibition.* Houston, Texas: Society of Petroleum Engineers.

SKARESTAD, M. S., A. 2011. Reservoarteknikk II, Ptek 213 - Fluid Properties and Recovery Methods.

SKJÆVELAND, S. M., KLEPPE, J. 1992. Recent Advances in Improved Oil Recovery Methods For North Sea Sandstone Reservoirs. *SPOR*.

SOHRABI, M., RIAZI, M., JAMIOLAHMADY, M., IRELAND, S. & BROWN, C. 2007. Carbonated water injection for oil recovery and CO2 storage. *Institute of Petroleum Engineering, Heriot-Watt University, Edinburgh, Scotland*.

SOLBAKKEN, J. S., SKAUGE, A. & AARRA, M. G. 2013. Supercritical CO Foam - The Importance of CO Density on Foams Performance. *In:* ENGINEERS, S. O. P. (ed.) *2013 SPE Enhanced Oil Recovery Conference.* Kuala Lumpur, Malaysia.

STATOIL. 2008. *Sleipner CCS* [Online]. Available: http://www.statoil.com/AnnualReport2008/no/Sustainability/Climate/Pages/5-3-2-3_SleipnerCCS.aspx [Accessed 06.08 2013].

STATOIL. 2013. *Improved oil recovery from carbonate reservoirs* [Online]. Available: http://www.statoil.com/en/technologyinnovation/optimizingreservoirrecovery/recoverymethods/tightfracturedgasandcarbonatereservoirs/pages/improvedoilrecoveryfromcarbonatereservoirs.aspx [Accessed 02.08 2013].

STOSUR, G. J. 1990. Enhanced Oil Recovery in North America: Status and Prospects. Energy Sources, Part A: Recovery, Utilization, and Environmental Effects. *12,* 4**,** 429-437.

STOSUR, G. J. & LUHNING, R. W. 1994. Worldwide EOR Activity in the Low Price Environment. *14th World Petroleum Congress.* Stavanger, Norway: World Petroleum Congress.

STOWELL, J. F. W., S.E.LAUBACH AND J.E.OLSON. 2001. Effect of modern state of stress on flow-controlling fractures: a misleading paradigm in need of revision. *DC Rocks 2001, The 38th U.S. Symposium on Rock Mechanics (USRMS).* Washington D.C.

TAN, C. T. & FIROOZABADI, A. 1995. Theoretical Analysis Of Miscible Displacement In Fractured Porous Media By A One-Dimensional Model: Part I -- Theory. *Journal of Canadian Petroleum Technology,* 34.

THOMAS, F. B., H, HOLOWACH N., ZHOU, X., BENNION, D. B. & BENNION, D. W. 1994. Miscible or Near-Miscible Gas Injection, Which Is Better. *SPE/DOE Improved Oil Recovery Symposium, 17-20 April Tulsa, Oklahoma.*

THOMAS, L. K., DIXON, T. N., EVANS, C. E. & VIENOT, M. E. 1987. Ekofisk Waterflood Pilot. *Journal of Petroleum Technology,* 39**,** 221-232.

THORSTEINSEN, T. F. 1995. Kompendium i Strålingsfysikk – FYS233. Fysisk institutt – UiB, **,** 21-31.

TIAB, D., DONALDSON, E.C. 2012. *Petrophysics Theory and Practice of Measuring Reservoir Rock and Fluid Transport Properties,* Amsterdam, Gulf Professional Publishing.

TINNI, A., EBRAHIM FATHI, RAJIV AGARWAL, CARL SONDERGELD, YUCEL AKKUTLU, AND CHANDRA RAI 2012. Shale Permeability Measurements on Plugs and Crushed Samples. *SPE Canadian Unconventional Resources Conference.* Calgary, Alberta, Canada: Society of Petroleum Engineers.

TOVAR, F. 2013. *RE: Personal Correspondence.* Type to GRADUATE, P.

VUILLAUME, J.-F. E., AKERVOLL, I. & BERGMO, P. E. S. 2011. CO2 injection Efficiency, Synthesis of Conceptual Chalk Model: Incremental Oil Recovery and CO2 Storage Potential. *Brasil Offshore.* Macaé, Brazil: Society of Petroleum Engineers.

WALSH, M. P., TEXAS A AND M U.; NEGAHBAN, S., GUPTA, S.P., AMOCO PRODUCTION CO. 1989. An Analysis of Water Shielding in Water-Wet Porous Media. *SPE Annual Technical Conference and Exhibition.* San Antonio, Texas.

WATANABE, N., T. ISHIBASHI, N. HIRANO, Y. OHSAKI, Y. TSUCHIYA, T. TAMAGAWA, H. OKABE, AND N. TSUCHIYA 2011. Precise 3D Numerical Modeling of Fracture Flow Coupled With X-Ray Computed Tomography for Reservoir Core Samples. *SPE Journal. (3)***,** 683-691.

WYLIE, P. L., KISHORE, K. & MOHANTY, U. 1999. Effect of Wettability on Oil Recovery by Near-Miscible Gas Injection *SPE Reservoir Evaluation & Engineering,* Volume 2, Number 6**,** 558-564.

XIAO, G., JINGJING, M., JIUDI, L., YANG, H. & HAIYING, W. 2012. Effect of Reservoir Temperature and Pressure on Relative Permeability. *SPETT 2012 Energy Conference and Exhibition.* Port-of-Spain, Trinidad: Society of Petroleum Engineers.

YAN, W. M., C.A. & HIRASAKI, G. J. 2006. Foam sweep in fractures for enhanced oil recovery. *Colloids and Surfaces,* A: Physicochem. Eng. Aspects**,** 282-283.

YELLIG, W. F., AMOCO PRODUCTION CO.; METCALFE, R.S., AMOCO PRODUCTION CO. 1980. Determination and Prediction of CO2 Minimum Miscibility Pressures. *Journal of Petroleum Technology,* Volume 32, Number 1**,** 160-168.

ZANGANEH, M. N., KAM, S. I., LAFORCE, T. & ROSSEN, W. R. 2011. The Method of Characteristics Applied to Oil Displacement by Foam. *SPE Journal,* 16**,** pp 8-23.

ZOLOTUKHIN, A. B., JANN-RUNE URSIN. 2000. *Introduction to Petroleum Reservoir Engineering.*

Appendix A – Uncertainty calculations

The uncertainty of value R given by variables *x, y, z, …, i*, and $S_{\bar{x}}$, $S_{\bar{y}}$, $S_{\bar{z}}$, … , $S_{\bar{i}}$, is the uncertainty related to each variable can then be calculated by equation:

$$S_{\bar{R}} = \sqrt{\left(\frac{\partial R}{\partial x} S_{\bar{x}}\right)^2 + \left(\frac{\partial R}{\partial y} S_{\bar{y}}\right)^2 + \left(\frac{\partial R}{\partial z} S_{\bar{z}}\right)^2 + \ldots + \left(\frac{\partial R}{\partial i} S_{\bar{i}}\right)^2} \qquad \text{(A1)}$$

where $x, y, z, \ldots, i$, are uncorrelated variables and $\bar{x}$, $\bar{y}$, $\bar{z}$, … , $\bar{i}$, are the arithmetical middle value of the measured variable given by:

$$\bar{x} = \frac{x_1 + x_2 + \ldots + x_N}{N} = \frac{1}{N}\sum_{i=1}^{N} x_i \qquad \text{(A2)}$$

If the value R is given as a product of variables, a^2, b^2 and c^2 , equation can be given by:

$$\frac{\partial_{\bar{R}}}{R} = \sqrt{a\left(\frac{\partial_{\bar{x}}}{\bar{x}}\right)^2 + b\left(\frac{\partial_{\bar{y}}}{\bar{y}}\right)^2 + c\left(\frac{\partial_{\bar{z}}}{\bar{z}}\right)^2} \qquad \text{(A3)}$$

Uncertainty in porosity

The contribution to uncertainty regarding porosity is by the use of a caliper. The bulk volume of the cores is calculated from the volume equation for a circular tube, $V_{Bulk} = \pi r^2 L$, where r is the radius of the core and L is the length. The uncertainty in bulk volume is then given by:

$$\partial_{\overline{V_{Bulk}}} = \sqrt{\left(\frac{\partial V_b}{\partial r}\partial_{\bar{r}}\right)^2 + \left(\frac{\partial V_b}{\partial L}\partial_L\right)^2} = \sqrt{(2\pi L\partial_{\bar{r}})^2 + (\pi r^2 \partial_L)^2} \qquad \text{(A4)}$$

The formula for pore volume is $V_p = \frac{m}{\rho}$, with uncertainties in fluid mass m and the density ρ :

$$\partial_{\overline{V_p}} = \sqrt{\left(\frac{\partial V_p}{\partial m}\partial_{\bar{m}}\right)^2 + \left(\frac{\partial V_p}{\partial \rho}\partial_{\bar{\rho}}\right)^2} \qquad \text{(A5)}$$

By combining equation A-4 and A-5, the uncertainty for porosity is given by:

$$\partial_{\bar{\phi}} = \sqrt{\left(\frac{1}{V_{Bulk}}\partial_{\overline{V_p}}\right)^2 + \left(\frac{V_p}{V_{Bulk}}\partial_{\overline{V_{Bulk}}}\right)^2} \qquad \text{(A6)}$$

Uncertainty in permeability

The contribution to uncertainty regarding permeability is the various variables in Darcy's law, such as injection rate, viscosity values at experimental conditions, length and width. Length and width is measured with a caliper and thus will be the same as for porosity measurements. The uncertainty in permeability is then given by:

$$\frac{\partial_{\bar{K}}}{K} = \sqrt{\left(\frac{\partial_{\bar{Q}}}{\bar{Q}}\right)^2 + \left(\frac{\partial_{\bar{\mu}}}{\bar{\mu}}\right)^2 + \left(\frac{\partial_{\bar{L}}}{\bar{L}}\right)^2 + \left(\frac{\partial_{\bar{A}}}{\bar{A}}\right)^2 + \left(\frac{\partial_{\overline{\Delta p}}}{\overline{\Delta p}}\right)^2} \qquad \text{(A7)}$$

Appendix B – Simulation data file

```
RESULTS SIMULATOR GEM 201210
INUNIT SI
WSRF WELL 1
WSRF GRID TIME
OUTSRF GRID SO SG SW PRES *X 'NC10' *X 'CO2'
OUTSRF RES NONE
WPRN GRID 0
OUTPRN GRID NONE
OUTPRN RES NONE

**$  Distance units: m
RESULTS XOFFSET         0.0000
RESULTS YOFFSET         0.0000
RESULTS ROTATION        0.0000  **$  (DEGREES)
RESULTS AXES-DIRECTIONS 1.0 -1.0 1.0
**$ *************************************************************************
**$ Definition of fundamental cartesian grid
**$ *************************************************************************
GRID VARI 34 21 1
KDIR DOWN
DI IVAR
 0.1 32*0.002641 0.1
DJ JVAR
 20*0.0008295 0.05
DK ALL
 714*0.00627

**$ Property: NULL Blocks  Max: 1  Min: 1
**$  0 = null block, 1 = active block
NULL CON          1

**$ Property: Porosity  Max: 0.0.45  Min: 0.45
POR ALL
0.999 32*0.45  0.999
0.999 32*0.45  0.999
0.999 32*0.45  0.999
0.999 32*0.45  0.999
0.999 32*0.45  0.999
0.999 32*0.45  0.999
0.999 32*0.45  0.999
0.999 32*0.45  0.999
0.999 32*0.45  0.999
0.999 32*0.45  0.999
0.999 32*0.45  0.999
0.999 32*0.45  0.999
0.999 32*0.45  0.999
0.999 32*0.45  0.999
0.999 32*0.45  0.999
0.999 32*0.45  0.999
0.999 32*0.45  0.999
0.999 32*0.45  0.999
0.999 32*0.45  0.999
0.999 32*0.45  0.999
34*0.999

**$ Property: Permeability I (md)   Max: 5.0  Min: 5.0
PERMI ALL
500000   32*5    500000
500000   32*5    500000
500000   32*5    500000
500000   32*5    500000
500000   32*5    500000
500000   32*5    500000
500000   32*5    500000
500000   32*5    500000
500000   32*5    500000
500000   32*5    500000
500000   32*5    500000
500000   32*5    500000
500000   32*5    500000
500000   32*5    500000
500000   32*5    500000
500000   32*5    500000
500000   32*5    500000
500000   32*5    500000
500000   32*5    500000
34*500000

**$ Property: Permeability J (md)   Max: 5.0  Min: 5.0
PERMJ ALL
500000   32*5    500000
```

```
500000  32*5    500000
500000  32*5    500000
500000  32*5    500000
500000  32*5    500000
500000  32*5    500000
500000  32*5    500000
500000  32*5    500000
500000  32*5    500000
500000  32*5    500000
500000  32*5    500000
500000  32*5    500000
500000  32*5    500000
500000  32*5    500000
500000  32*5    500000
500000  32*5    500000
500000  32*5    500000
500000  32*5    500000
500000  32*5    500000
500000  32*5    500000
500000  32*5    500000
34*500000
**$ Property:eability K (md)   Max: 5.0  Min: 5.0
PERMK ALL
500000  32*5    500000
500000  32*5    500000
500000  32*5    500000
500000  32*5    500000
500000  32*5    500000
500000  32*5    500000
500000  32*5    500000
500000  32*5    500000
500000  32*5    500000
500000  32*5    500000
500000  32*5    500000
500000  32*5    500000
500000  32*5    500000
500000  32*5    500000
500000  32*5    500000
500000  32*5    500000
500000  32*5    500000
500000  32*5    500000
500000  32*5    500000
500000  32*5    500000
34*500000

**$ Property: Pinchout Array  Max: 1  Min: 1
**$  0 = pinched block, 1 = active block
PINCHOUTARRAY CON           1
SECTORARRAY 'FRACTURE1'  ALL
 1 33*0 1 33*0 1 33*0 1 33*0 1 33*0 1 33*0 1 33*0 1 33*0 1 33*0 1 33*0 1 33*0 1
 33*0 1 33*0 1 33*0 1 33*0 1 33*0 1 33*0 1 33*0 1 33*0 1 33*0 1 33*0 1 33*0
SECTORARRAY 'FRACTURE2'  ALL
 33*0 1 33*0 1 33*0 1 33*0 1 33*0 1 33*0 1 33*0 1 33*0 1 33*0 1 33*0 1 33*0
 1 33*0 1 33*0 1 33*0 1 33*0 1 33*0 1 33*0 1 33*0 1 33*0 1 33*0 1*1
SECTORARRAY 'FRACTURE3'  ALL
 681*0 32*1 1*0
SECTORARRAY 'MATRIX'  ALL
 0 32*1 2*0 32*1 2*0 32*1 2*0 32*1 2*0 32*1 2*0 32*1 2*0 32*1 2*0 32*1 2*0 32*1 2*0
 32*1 2*0 32*1 2*0 32*1 2*0 32*1 2*0 32*1 2*0 32*1 2*0 32*1 2*0 32*1 2*0 32*1 2*0
 32*1 2*0 32*1 2*0 32*1 2*0 32*1 35*0

**DEPTH 1 34 1 1000

DEPTH-TOP ALL
714*1000
**$ Model and number of components

MODEL PR
**=-=-=Component Selection/Properties
**REM
NC 2 2
COMPNAME 'CO2' 'NC10'
HCFLAG
0 1
VISCOR HZYT
MIXVC 1
VISCOEFF 0.1023 0.023364 0.058533 -0.040758 0.0093324
PVC3 1.2
MW
44.01 142.286
AC
0.225 0.49
PCRIT
72.8 20.8
VCRIT
0.094 0.603
TCRIT
304.2 617.6
```

```
PCHOR
78 433.5
SG
0.818 0.734
TB
-78.45 174.15
OMEGA
0.457236 0.457236
OMEGB
0.0777961 0.0777961
VSHIFT
0 0
HEATING_VALUES
0 6473.36
VISVC
0.094 0.603
BIN
0.11

TRES 20
VISW 1.09

**DIFCOR-OIL *WILKE
*DIFFC-OIL      0.0001 0

ROCKFLUID
RPT 1
**$      Sw      krw     krow      Pcow
SWT
        0       0      1.0        0
      1.0      1.0       0        0
**$      Sl      krg     krog
SLT
        0       1       0
        1       0       1
RPT 2
**$      Sw      krw     krow         Pcow
SWT
      0.13       0       1   21.75568367
      0.15   0.0014   0.9846   17.40454694
      0.18   0.0036   0.9539   12.32822075
      0.23   0.0074   0.8881   7.977084013
       0.3   0.0127   0.7655   4.786250408
      0.33    0.015   0.7021   3.843504115
     0.391   0.0196    0.553   2.921730302
     0.469   0.0581   0.3229   2.707813916
     0.564   0.1312   0.1444   2.444918235
     0.632   0.2036   0.0408   2.270423148
     0.674   0.2574   0.0058   2.152362305
     0.702   0.2974   0.0003   2.069748722
      0.71   0.3095   0.0002   2.047354871
     0.718   0.3218   0.0001   2.026454911
     0.722   0.3281        0  -2.175568367
**$      Sl      krg     krog
SLT
        0       1       0
        1       0       1

RTYPE ALL
1*1  32*2  1*1
1*1  32*2  1*1
1*1  32*2  1*1
1*1  32*2  1*1
1*1  32*2  1*1
1*1  32*2  1*1
1*1  32*2  1*1
1*1  32*2  1*1
1*1  32*2  1*1
1*1  32*2  1*1
1*1  32*2  1*1
1*1  32*2  1*1
1*1  32*2  1*1
1*1  32*2  1*1
1*1  32*2  1*1
1*1  32*2  1*1
1*1  32*2  1*1
1*1  32*2  1*1
1*1  32*2  1*1
1*1  32*2  1*1
34*1

INITIAL

USER_INPUT
**VERTICAL BLOCK_CENTER WATER_OIL
**REFPRES
**9200
```

```
**REFDEPTH
**1000
**DWOC
**5000

**REFPRES
**9200

**REFDEPTH
**1000

**DWOC
**5000

*PRES    *KVAR  9200.0
*SW      *IJK                        1 1:21 1    0
                                                                                34 1:21 1    0
                                                                                2:33 21 1    0
                                                                                2:33 1:20 1  0
ZGLOBALC 'NC10' ALL
 0 32*1 2*0 32*1 2*0 32*1 2*0 32*1 2*0 32*1 2*0 32*1 2*0 32*1 2*0 32*1 2*0 32*1
 2*0 32*1 2*0 32*1 2*0 32*1 2*0 32*1 2*0 32*1 2*0 32*1 2*0 32*1 2*0 32*1 2*0
 32*1 2*0 32*1 2*0 32*1 2*0 32*1 2*0 32*1 35*0
ZGLOBALC 'CO2' ALL
 1 32*0 2*1 32*0 2*1 32*0 2*1 32*0 2*1 32*0 2*1 32*0 2*1 32*0 2*1 32*0 2*1 32*0
 2*1 32*0 2*1 32*0 2*1 32*0 2*1 32*0 2*1 32*0 2*1 32*0 2*1 32*0 2*1 32*0 2*1
 32*0 2*1 32*0 2*1 32*0 2*1 32*0 2*1 32*0 35*1

NUMERICAL
DTMAX 0.5
DTMIN 0.00000001
NORM PRESS 100
NORM SATUR 0.15
NORM GMOLAR 0.05
NORM AQUEOUS 0.15
NORM TEMP 10
MAXCHANGE GMOLAR 0.1
CONVERGE HC 0.02
NEWTONCYC 1000
ITERMAX 200
ITERMIN 8
RUN

DATE 2013 4 11
DTWELL 0.00001

**REFINE 1 3 1
**RANGE 9:26 15:20 1
**REFINE 3 3 1
**RANGE 2:8 15:20 1
**RANGE 27:33 15:20 1
**REFINE 3 1 1
**RANGE 2:8 1:14 1
**RANGE 27:33 1:14 1

DATE 2013 4 11.04167
DATE 2013 4 11.08333
DATE 2013 4 11.12500
DATE 2013 4 11.16667
DATE 2013 4 12.00000
DATE 2013 4 13.00000
DATE 2013 4 14.00000
DATE 2013 4 15.00000
DATE 2013 4 16.00000
RESULTS CMOST FOOTER 309898470

RESULTS SPEC 'Permeability I'
RESULTS SPEC SPECNOTCALCVAL -99999
RESULTS SPEC REGION 'All Layers (Whole Grid)'
RESULTS SPEC REGIONTYPE 'REGION_WHOLEGRID'
RESULTS SPEC LAYERNUMB 0
RESULTS SPEC PORTYPE 1
RESULTS SPEC CON 51.045
RESULTS SPEC SPECKEEPMOD 'YES'
RESULTS SPEC STOP

RESULTS SPEC 'Permeability J'
RESULTS SPEC SPECNOTCALCVAL -99999
RESULTS SPEC REGION 'All Layers (Whole Grid)'
RESULTS SPEC REGIONTYPE 'REGION_WHOLEGRID'
RESULTS SPEC LAYERNUMB 0
RESULTS SPEC PORTYPE 1
RESULTS SPEC CON 51.045
RESULTS SPEC SPECKEEPMOD 'YES'
RESULTS SPEC STOP

RESULTS SPEC 'Permeability K'
```

```
RESULTS SPEC SPECNOTCALCVAL -99999
RESULTS SPEC REGION 'All Layers (Whole Grid)'
RESULTS SPEC REGIONTYPE 'REGION_WHOLEGRID'
RESULTS SPEC LAYERNUMB 0
RESULTS SPEC PORTYPE 1
RESULTS SPEC CON 51.045
RESULTS SPEC SPECKEEPMOD 'YES'
RESULTS SPEC STOP

RESULTS SPEC 'Porosity'
RESULTS SPEC SPECNOTCALCVAL -99999
RESULTS SPEC REGION 'All Layers (Whole Grid)'
RESULTS SPEC REGIONTYPE 'REGION_WHOLEGRID'
RESULTS SPEC LAYERNUMB 0
RESULTS SPEC PORTYPE 1
RESULTS SPEC CON 0.254
RESULTS SPEC SPECKEEPMOD 'YES'
RESULTS SPEC STOP

RESULTS SPEC 'Pressure'
RESULTS SPEC SPECNOTCALCVAL -99999
RESULTS SPEC REGION 'All Layers (Whole Grid)'
RESULTS SPEC REGIONTYPE 'REGION_WHOLEGRID'
RESULTS SPEC LAYERNUMB 0
RESULTS SPEC PORTYPE 1
RESULTS SPEC CON 9230
RESULTS SPEC SPECKEEPMOD 'YES'
RESULTS SPEC STOP


RESULTS SPEC 'Rock Density'
RESULTS SPEC SPECNOTCALCVAL -99999
RESULTS SPEC REGION 'All Layers (Whole Grid)'
RESULTS SPEC REGIONTYPE 'REGION_WHOLEGRID'
RESULTS SPEC LAYERNUMB 0
RESULTS SPEC PORTYPE 1
RESULTS SPEC CON 2012
RESULTS SPEC SPECKEEPMOD 'YES'
RESULTS SPEC STOP


RESULTS SPEC 'Water Saturation'
RESULTS SPEC SPECNOTCALCVAL -99999
RESULTS SPEC REGION 'All Layers (Whole Grid)'
RESULTS SPEC REGIONTYPE 'REGION_WHOLEGRID'
RESULTS SPEC LAYERNUMB 0
RESULTS SPEC PORTYPE 1
RESULTS SPEC CON 0
RESULTS SPEC SPECKEEPMOD 'YES'
RESULTS SPEC STOP


RESULTS SPEC 'Initial Water Saturation'
RESULTS SPEC SPECNOTCALCVAL -99999
RESULTS SPEC REGION 'All Layers (Whole Grid)'
RESULTS SPEC REGIONTYPE 'REGION_WHOLEGRID'
RESULTS SPEC LAYERNUMB 0
RESULTS SPEC PORTYPE 1
RESULTS SPEC CON 0
RESULTS SPEC SPECKEEPMOD 'YES'
RESULTS SPEC STOP


RESULTS SPEC 'Block Temperature'
RESULTS SPEC SPECNOTCALCVAL -99999
RESULTS SPEC REGION 'All Layers (Whole Grid)'
RESULTS SPEC REGIONTYPE 'REGION_WHOLEGRID'
RESULTS SPEC LAYERNUMB 0
RESULTS SPEC PORTYPE 1
RESULTS SPEC CON 20
RESULTS SPEC SPECKEEPMOD 'YES'
RESULTS SPEC STOP


RESULTS SPEC 'Global Composition$C' 'CO2'
RESULTS SPEC SPECNOTCALCVAL -99999
RESULTS SPEC REGION 'All Layers (Whole Grid)'
RESULTS SPEC REGIONTYPE 'REGION_WHOLEGRID'
RESULTS SPEC LAYERNUMB 0
RESULTS SPEC PORTYPE 1
RESULTS SPEC CON 1
RESULTS SPEC SPECKEEPMOD 'YES'
RESULTS SPEC STOP


RESULTS SPEC 'Global Composition$C' 'NC10'
RESULTS SPEC SPECNOTCALCVAL -99999
```

```
RESULTS SPEC REGION 'All Layers (Whole Grid)'
RESULTS SPEC REGIONTYPE 'REGION_WHOLEGRID'
RESULTS SPEC LAYERNUMB 0
RESULTS SPEC PORTYPE 1
RESULTS SPEC CON 2
RESULTS SPEC SPECKEEPMOD 'YES'
RESULTS SPEC STOP

RESULTS SPEC 'Grid Thickness'
RESULTS SPEC SPECNOTCALCVAL -99999
RESULTS SPEC REGION 'All Layers (Whole Grid)'
RESULTS SPEC REGIONTYPE 'REGION_WHOLEGRID'
RESULTS SPEC LAYERNUMB 0
RESULTS SPEC PORTYPE 1
RESULTS SPEC CON 0.0103107
RESULTS SPEC SPECKEEPMOD 'YES'
RESULTS SPEC STOP
```